SEMMELWEIS EGYETEM

DOKTORI ISKOLA

Ph.D. értekezések

3310.

AMIR DAMOUNI

Celluláris és molekuláris élettan

című program

Programvezető: Dr. Hunyady Lásszló, egyetemi tanár

Témavezető: Dr. Várnai Péter, egyetemi tanár

Differential SHIP2 Activation by EGF and Insulin Uncovers Pathway-Specific Control of PI(3,4)P_2 Signaling

PhD thesis

Amir Damouni

Molecular Medicine Division

Semmelweis University

Supervisor: Péter Várnai, MD, DSc

Official reviewers: Farkas Sarnyai, PhD
Csilla Laczka, PhD

Head of the Complex Examination Committee:
Miklós Geiszt, MD, DSc

Members of the Complex Examination Committee:
Tamás Hegedűs, DSc
László Homolya, PhD

Budapest
2025

Table of contents

List of Abbreviations

Akt	Protein kinase B
Arf	ADP-ribosylation factor
BRET	Bioluminescence resonance energy transfer
Btk	Bruton's tyrosine kinase
CMV	Cytomegalovirus
DMEM	Dulbecco's modified eagle medium
DMSO	Dimethyl sulfoxide
DNA	Deoxyribonucleic acid
EGF	Epidermal growth factor
EGFR	Epidermal growth factor receptor
ER	Endoplasmic reticulum
ERK	Extracellular signal regulated kinase
FBS	Fetal bovine serum
GAP	GTPase-activating protein
GEF	Guanine nucleotide exchange factor
GPCR	G protein-coupled receptors
GRP1	General receptor for phosphoinositides-1
HEK293	Human embryonic kidney 293 cells
HEK293-AT1R	HEK293 cells expressing the angiotensin II type 1A receptor
HRP	Horseradish peroxidase
IR	Insulin receptor
mTORC2	Mechanistic target of rapamycin complex 2
NES	Nuclear export signal
OCRL	Oculocerebrorenal syndrome of Lowe protein
PD	Phosphatase domain deleted
PDK1	Phosphoinositide-dependent protein kinase-1
PH	Pleckstrin homology
PI	Phosphatidylinositol
$PI(3,4)P_2$	Phosphatidylinositol 3,4-bisphosphate
$PI(4,5)P_2$	Phosphatidylinositol 4,5-bisphosphate
PI3K	Phosphoinositide 3-kinase

PI3KC2A	Phosphoinositide 3-kinase Class II alpha
PI3KC2B	Phosphoinositide 3-kinase Class II beta
PI3P	Phosphatidylinositol 3-phosphate
PI4P	Phosphatidylinositol 4-phosphate
PIP_3	Phosphatidylinositol 3,4,5-trisphosphate
PIP	Phosphoinositides
PIPP	Proline-rich inositol polyphosphate 5-phosphatase
PLCγ	Phospholipase C gamma
PM	Plasma membrane
PTEN	Phosphatase and tensin homolog
PVDF	Polyvinylidene difluoride
RNA	Ribonucleic acid
RTK	Receptor tyrosine kinase
SDS	Sodium dodecyl sulfate
SH2	Src homology 2
SHIP	SH2-domain-containing inositol polyphosphate 5-phosphatase
siRNA	Small interfering RNA
SKIP	Skeletal muscle and kidney-enriched inositol polyphosphate 5-phosphatase
TAPP1	Tandem PH domain-containing protein 1
TK	Thymidine kinase
WT	Wild type
Wm	Wortmannin

1. Introduction

1.1. Inositol lipids

Phosphoinositides (PIPs) are a specialized subgroup of phospholipids derived from phosphatidylinositol (PI) that exist in dynamic and tightly regulated pools within cellular membranes (1). These amphipathic molecules consist of a glycerol backbone, two fatty acid chains, which can vary from 14 to 22 carbon atoms in length and range from saturated to mono- or polyunsaturated, and a myo-inositol head group that can be phosphorylated at multiple positions (2). A series of lipid kinases and phosphatases interconvert these lipids to generate seven distinct PIP species, each defined by unique phosphorylation patterns on the 3-, 4-, and 5-hydroxyl groups of the inositol ring **(Figure 1)** (3, 4). These patterns dictate the subcellular localization and functional roles of each species. PIPs are asymmetrically distributed across intracellular membranes: for example, phosphatidylinositol 4-phosphate (PI4P) is mainly concentrated at the Golgi apparatus (5), while phosphatidylinositol 3,4,5-trisphosphate (PIP_3) is predominantly localized to the inner leaflet of the plasma membrane. This compartmentalization is critical for establishing membrane identity (3) and coordinating trafficking routes between organelles. PIPs are low-abundance but functionally critical phospholipids. Among them, PI4P and phosphatidylinositol 4,5-bisphosphate [$PI(4,5)P_2$] are the most prevalent in mammalian cells, together accounting for approximately 0.5-1.5% of total cellular phospholipids. In contrast, PIP_3 is present at much lower levels, only about 0.1-1% of the amount of PI4P and $PI(4,5)P_2$ under basal conditions (6). Phosphatidylinositol 3,4-bisphosphate [$PI(3,4)P_2$] is even less abundant, comprising less than 0.1% of the total phosphoinositide pool (3).

Beyond their structural roles, PIPs function as versatile regulators of cellular signaling (7). They act as signaling molecules, membrane identity markers, and scaffolding platforms for protein recruitment (1). Their functions are mediated primarily through interactions with effector proteins containing specific lipid-binding domains, such as the pleckstrin homology (PH) domain (8, 9). PIPs are key regulators of diverse cellular processes, including signal transduction (e.g., the phosphoinositide 3-kinases/ protein kinase B [PI3K/Akt] pathway), cytoskeletal dynamics, cell migration, polarity and morphogenesis, endocytosis and exocytosis, autophagy, and calcium signaling (10,

11). Importantly, PIP levels are dynamically regulated and respond rapidly to extracellular stimuli such as growth factors, insulin, and cytokines, enabling swift cellular adaptation. PIPs are primarily synthesized in the endoplasmic reticulum (ER) and distributed to other membrane compartments, including the plasma membrane, through vesicular transport and lipid transfer proteins (12). Dysregulation of phosphoinositide metabolism has been linked to various human diseases, including cancer, metabolic disorders, neurodegenerative diseases and immunodeficiencies, underscoring their essential role in maintaining cellular homeostasis (13, 14).

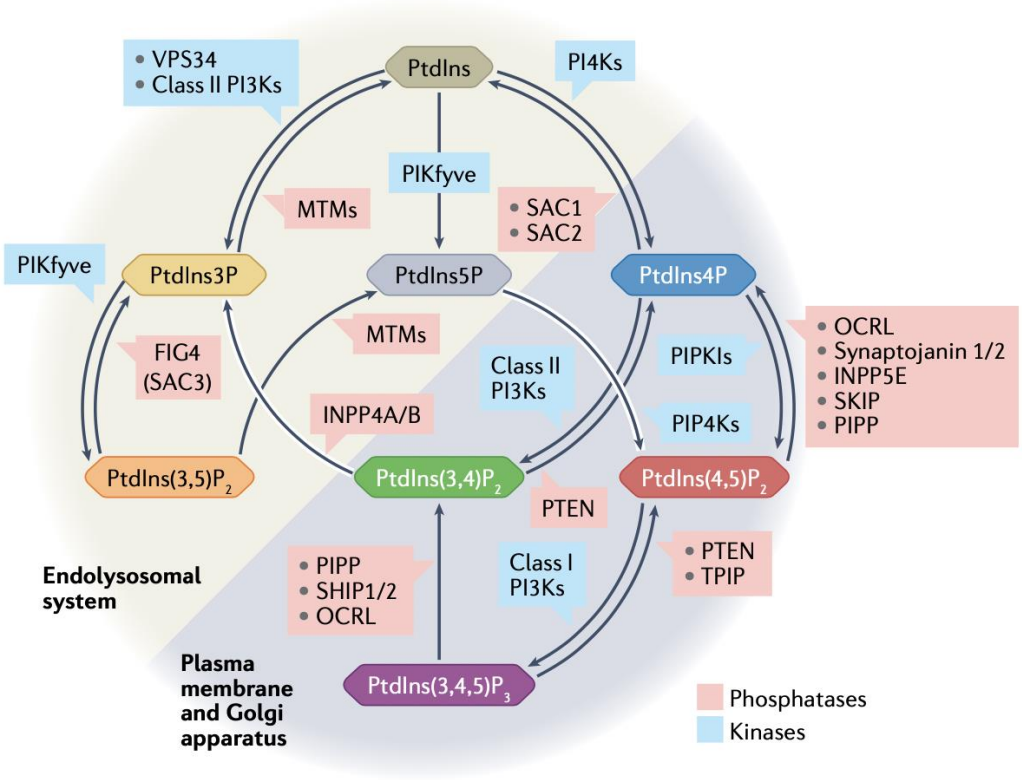

Figure 1. The PIP species, their subcellular distribution and the enzymes involved in their interconversion. There are 7 PIP species, each defined by unique phosphorylation patterns on the 3-, 4-, and 5-hydroxyl groups of the inositol ring. PIPs exist in dynamic pools and are rapidly converted into one another by PI kinases and phosphatases (1).

1.1.1. Phosphatidylinositol 3,4,5-trisphosphate (PIP3)

PIP_3 is a low-abundance but highly potent phosphoinositide predominantly localized to the inner leaflet of the plasma membrane. Despite its modest representation within the lipidome, PIP_3 plays a central role in intracellular signaling, particularly in pathways initiated by receptor tyrosine kinases (RTKs), as well as G protein-coupled

receptors (GPCRs) and cytokine receptors. Upon stimulation of RTKs, class I PI3Ks are activated and catalyze the phosphorylation of $PI(4,5)P_2$ at the 3-position of the inositol ring, leading to the production of PIP_3 at the plasma membrane (15).

Once formed, PIP_3 serves as a critical second messenger by recruiting downstream effector proteins that contain PH domains (16). These include key signaling molecules such as Akt, phosphoinositide-dependent protein kinase-1 (PDK1), Bruton's tyrosine kinase (Btk), and general receptor for phosphoinositides-1 (GRP1) (17, 18). The membrane recruitment of these effectors is essential for their activation, with Akt being one of the most prominent. Full activation of Akt requires its colocalization with both PDK1 and mTOR complex 2 (mTORC2) at PIP_3-enriched membrane regions (19). Akt, a serine/threonine kinase, regulates diverse cellular processes including survival, growth, proliferation, and metabolism (20, 21).

Beyond its role in growth factor signaling, PIP_3 influences a wide array of cellular events such as cytoskeletal reorganization, membrane trafficking and exocytosis (22). It also plays vital roles during embryogenesis, particularly in neural and vascular development, and is indispensable for proper immune cell function (23).

The levels of PIP_3 are tightly controlled by opposing enzymatic activities. It can be dephosphorylated at the 3-position by the tumor suppressor phosphatase and tensin homolog (PTEN), regenerating $PI(4,5)P_2$, or alternatively, it can be converted into $PI(3,4)P_2$ through the action of 5-phosphatases such as SH2-domain-containing inositol polyphosphate 5-phosphatase (SHIP) enzymes **(Figure 2)** (24, 25). Disruption of this balance, for example through hyperactivation of PI3Ks or loss-of-function mutations in PTEN, leads to sustained PIP_3 accumulation and constitutive Akt signaling. This dysregulation has been implicated in the pathogenesis of numerous diseases, including various cancers, insulin resistance and type 2 diabetes, autoimmune conditions, and neurodevelopmental disorders (26, 27). Notably, PTEN mutations represent one of the most frequent genetic alterations in human malignancies (28). In light of its pathological relevance, the PI3K/Akt signaling axis is the focus of extensive therapeutic development, with several PI3K and Akt inhibitors currently undergoing evaluation in clinical trials for oncology and inflammatory diseases (29).

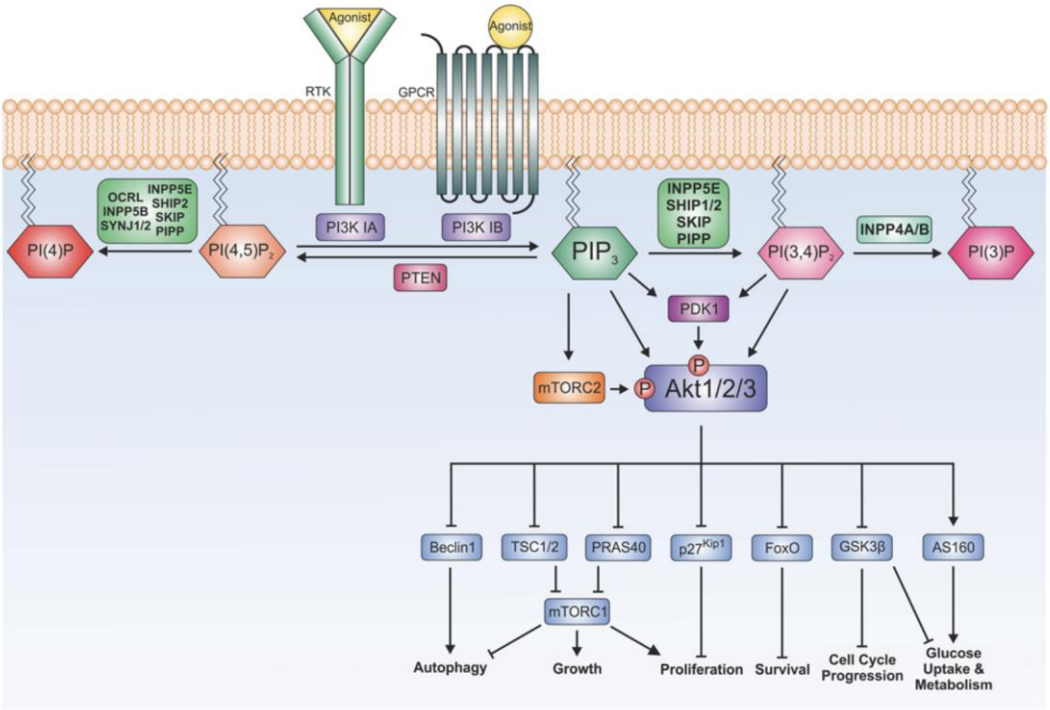

Figure 2. PIP_3 synthesis and degradation pathways and activation of Akt downstream of RTKs or GPCRs. PIP_3 is generated from $PI(4,5)P_2$ by Class I PI3Ks, after which it can be dephosphorylated into $PI(4,5)P_2$ or $PI(3,4)P_2$ by PTEN or 5-phosphatases, respectively (30).

1.1.2. Phosphatidylinositol 3,4-bisphosphate [$PI(3,4)P_2$]

$PI(3,4)P_2$ is a low-abundance yet functionally important phosphoinositide that shares several characteristics with PIP_3, but also exhibits distinct biological roles. Its distribution within the cell is determined by its route of synthesis and is primarily enriched at the plasma membrane and endosomal compartments. $PI(3,4)P_2$ is generated through two major biosynthetic pathways: first, via the dephosphorylation of PIP_3 at the 5-position by phosphatases such as SHIP1 and SHIP2, which occurs at the plasma membrane, and second, through the direct phosphorylation of PI4P by class II PI3Ks (PI3KC2), a route that predominates at endocytic vesicles and plays a key role in endocytosis (31, 32). $PI(3,4)P_2$ is subsequently broken down by the 4-phosphatases INPP4A and INPP4B, which convert it into phosphatidylinositol 3-phosphate (PI3P) (33).

Historically considered merely a metabolic intermediate or breakdown product of PIP_3, $PI(3,4)P_2$ has more recently emerged as a signaling lipid in its own right, with distinct effectors and functions (34). Several proteins exhibit selective binding to $PI(3,4)P_2$, including TAPP1 and Akt2, underscoring its independent role in intracellular

signaling. Like PIP_3, $PI(3,4)P_2$ is rapidly and transiently produced in response to extracellular cues such as growth factors and chemokines, and its accumulation is often spatially restricted to defined membrane regions.

Functionally, $PI(3,4)P_2$ contributes to key cellular processes including cytoskeletal remodeling, cell polarization, adhesion and migration (35). Its spatial and temporal regulation supports fine-tuned cellular responses to environmental stimuli. Importantly, disruptions in $PI(3,4)P_2$ signaling have been implicated in the pathogenesis of various diseases, including cancer, metabolic syndromes, and immune dysfunctions, further highlighting its emerging importance in both physiology and disease.

1.1.3. Phosphoinositide 3-kinases (PI3Ks)

PI3Ks constitute a family of lipid kinases that catalyze the phosphorylation of the 3-hydroxyl group on the inositol ring of phosphoinositides. This enzymatic activity results in the generation of key signaling lipids, including PI3P, $PI(3,4)P_2$ and PIP_3. These lipid products serve as second messengers that regulate a wide array of cellular processes.

PI3Ks are classified into three distinct classes, Class I, II, and III, based on their structural features, regulatory mechanisms, and substrate specificity (36). Class I PI3Ks are the most extensively studied and play a central role in growth factor signaling. They are heterodimeric enzymes composed of a catalytic subunit and a regulatory subunit (37). This class is further subdivided into Class IA, which is activated primarily by RTKs, and Class IB, which is activated by GPCRs. The primary lipid product of Class I PI3Ks is PIP_3, synthesized from $PI(4,5)P_2$ at the plasma membrane (38).

Class II PI3Ks, comprising PI3KC2α, PI3KC2β, and PI3KC2γ, are monomeric enzymes that do not possess regulatory subunits. Although less well-characterized than Class I, Class II PI3Ks have been implicated in pivotal processes such as clathrin-mediated endocytosis, intracellular membrane trafficking, and insulin signaling. Their lipid products include PI3P and $PI(3,4)P_2$, generated from PI and PI4P, respectively. Class III PI3K, represented solely by Vps34, specifically generates PI3P and is essential for autophagy, endosomal maturation and lysosomal trafficking (39, 40).

PI3K activity is tightly regulated by multiple mechanisms, including membrane recruitment, conformational changes and post-translational modifications such as phosphorylation and dephosphorylation. Dysregulation of PI3K signaling has been

associated with a wide spectrum of pathological conditions, including metabolic disorders, inflammatory diseases, and neurodegeneration. However, its role in cancer is especially prominent. Abnormal activation of the PI3K pathway leads to unchecked cellular proliferation, enhanced survival, metabolic reprogramming, and resistance to apoptosis (41, 42).

1.1.4. SH2-domain-containing inositol polyphosphate 5-phosphatase (SHIP)

SHIP enzymes are a class of lipid phosphatases that selectively hydrolyze the 5-phosphate group from phosphoinositides. Their primary substrate is PIP_3, which they convert into $PI(3,4)P_2$, thereby modulating key signaling events downstream of PI3K activation. Structurally, SHIP enzymes are composed of several functionally distinct domains. An N-terminal Src homology 2 (SH2) domain enables interaction with phosphorylated tyrosine residues on activated receptors or adaptor proteins. This is followed by a central catalytic domain responsible for the 5-phosphatase activity, and a C-terminal region that contains proline-rich motifs, NPXY sequences, and other interaction sites that facilitate binding to additional signaling partners. Two main isoforms of SHIP have been identified: SHIP1, which is primarily expressed in hematopoietic and immune cells, and SHIP2, which is more broadly expressed across diverse tissues (43, 44). These enzymes play critical roles in the regulation of immune responses, insulin signaling, and cell survival. SHIP2 is phosphorylated on multiple tyrosine and serine residues, which modulate its enzymatic activity, subcellular localization and interaction with adaptor proteins.

The involvement of SHIP enzymes in human disease is multifaceted. Dysregulation of SHIP activity has been implicated in conditions such as Alzheimer's disease, obesity, and type 2 diabetes (45, 46). In the context of cancer, their function remains complex and context-dependent (47). On the one hand, SHIP-mediated depletion of PIP_3 can attenuate Akt signaling, supporting a tumor suppressor role. On the other hand, the enzymatic product $PI(3,4)P_2$ can itself activate specific Akt isoforms, thereby potentially contributing to pro-tumorigenic signaling. As a result, SHIP enzymes have attracted attention in cancer research, with current investigations examining whether inhibiting their activity could offer a viable therapeutic approach (48).

1.2. Epidermal growth factor receptor (EGFR) and insulin receptor

The epidermal growth factor receptor (EGFR) and the insulin receptor (IR) are both members of the RTK family and share several key signaling characteristics. Both receptors activate class I phosphoinositide 3-kinases (PI3Ks), leading to elevated PIP_3 levels and subsequent recruitment and activation of Akt kinase. Despite these similarities, they also exhibit notable differences in their signaling mechanisms. Specifically, EGFR and IR engage distinct adaptor proteins to mediate PI3K and Akt activation, and they trigger divergent downstream pathways (49, 50). For instance, EGFR stimulation activates phospholipase C-γ (PLCγ), resulting in intracellular calcium mobilization and activation of protein kinase C (PKC) isoforms (50, 51). In contrast, IR signaling can promote the activation of Rho and Rab family GTPases, which are involved in facilitating glucose uptake in skeletal muscle (49, 52). Importantly, $PI(3,4)P_2$ has been implicated in the signaling networks of both receptors. However, its precise regulatory mechanisms and relative functional contributions remain incompletely defined.

1.3. Plekstrin homology (PH) domains

PH domains are short protein segments of roughly 120 amino acids that are present in numerous intracellular signaling proteins (53). These domains exhibit considerable variability in their ability to recognize and bind specific phosphoinositide species, some display high selectivity for a single PIP, while others can interact with several types. This binding specificity plays a key role in directing PH domain-containing proteins to particular membrane regions, thereby facilitating the coordination of cellular signaling pathways. PH domains are found in a wide range of signaling molecules, such as kinases, phospholipases, guanine nucleotide exchange factors (GEFs), and GTPase-activating proteins (GAPs), highlighting their diverse functional roles in cell regulation (54). Due to their high specificity and affinity for distinct phosphoinositide species, certain PH domains have been adapted as molecular biosensors to visualize dynamic lipid signaling events and track changes in phosphoinositide distribution in living cells (55).

Although PH domains are traditionally recognized for mediating plasma membrane localization via binding to phosphoinositides such as PIP_3, recent studies indicate that lipid binding alone does not fully explain their membrane-targeting behavior.

Increasing evidence shows that many PH domains also rely on lipid-independent interactions with membrane-associated proteins or structural elements to achieve proper localization (56, 57). For instance, in the case of dynamin, the intrinsic phosphoinositide-binding capacity of its PH domain is insufficient for membrane association, yet its localization is still modulated by inositol lipid signaling, implying the involvement of additional regulatory mechanisms (58-60). Moreover, overexpression of isolated PH domains has been shown to competitively interfere with the function of endogenous membrane-associated proteins. Notably, certain PH domain mutations that retain phosphoinositide binding but disrupt protein-protein interactions diminish this inhibitory effect. These findings highlight the importance of both lipid-dependent and lipid-independent mechanisms in ensuring the correct localization and regulatory function of PH domains at the plasma membrane, as illustrated by studies on Akt and GRP1 (61).

1.3.1. General receptor for phosphoinositides-1 (GRP1)

GRP1 is a member of the cytohesin family of GEFs that activate ADP-ribosylation factor (Arf) GTPases, thereby playing a pivotal role in regulating vesicular trafficking and actin cytoskeleton dynamics in mammalian cells (62). Central to GRP1's membrane targeting is its PH domain, which binds specifically to PIP_3, a critical determinant of its recruitment to the plasma membrane and subsequent cellular function (63). While electrostatic interactions with negatively charged phospholipids, such as phosphatidylserine, may contribute to transient membrane association, they are insufficient to support stable localization in the absence of specific lipid interactions (64-66).

The isolated PH domain of GRP1 has become a widely used biosensor for visualizing PIP_3 dynamics at the plasma membrane (55, 67, 68). However, its membrane binding is now understood to involve more than lipid recognition alone. Studies have shown that protein-protein interactions are also essential for its proper localization. This was demonstrated by point mutations (I307E and K340L) that preserve PIP_3 binding but disrupt membrane association and abolish the dominant-negative effects typically induced by PH domain overexpression (61). These findings led to the identification of the active, GTP-bound form of Arf6 as a critical non-lipid binding partner (69), emphasizing

the dual requirement of both lipid and protein interactions for GRP1's stable membrane recruitment and function.

1.3.2. Protein kinase B (Akt)

Akt comprises three isoforms, Akt1, Akt2, and Akt3, that share considerable structural similarity yet exhibit distinct tissue-specific expression patterns and physiological roles (70). Structurally, Akt consists of three major domains: a PH domain, a kinase domain, and a regulatory tail. Akt functions as a pivotal effector in the PI3K signaling pathway and regulates numerous essential cellular processes. Its activation is initiated by RTK stimulation, which promotes PI3K activity and leads to the generation of PIP_3 at the plasma membrane (15). Akt is subsequently recruited to PIP_3-enriched membrane regions via its PH domain, where it undergoes full activation through phosphorylation at two key residues: threonine 308 by PDK1 and serine 473 by mTORC2 (71). Once activated, Akt phosphorylates a wide array of substrates distributed across the cytosol, plasma membrane, and nucleus (72).

In addition to PIP_3, the PH domain of Akt, particularly that of the Akt2 isoform, can also bind $PI(3,4)P_2$ (73), thus Akt activation may be modulated by multiple phosphoinositide species. Moreover, Akt has been shown to associate with phosphatidylserine at a separate binding site, which enhances its affinity for PIP_3 and promotes membrane recruitment (74). Beyond its well-characterized lipid interactions, Akt is also believed to participate in protein-protein interactions that further regulate its localization and activity. Although the exact binding partners remain unidentified, evidence for such interactions comes from mutational studies which reveal that substitutions at threonine 34 within the PH domain (e.g., T34L and T34F) selectively disrupt non-lipid interactions without affecting lipid binding, as reflected by the absence of dominant-negative effects with these mutants (61).

2. Objectives

This study aimed to investigate receptor-specific regulation of phosphoinositide signaling and to develop improved tools for monitoring PIP_3 dynamics in mammalian cells. The objectives can be divided into two groups:

2.1. To investigate the dynamics and regulation of $PI(3,4)P_2$ production in response to EGF and insulin signaling:

- To compare the plasma membrane dynamics of PIP_3 and $PI(3,4)P_2$ following stimulation with EGF and insulin in mammalian cells.
- To elucidate the enzymatic mechanisms governing $PI(3,4)P_2$ production at the plasma membrane, with a specific focus on the role and contribution of SHIP2.
- To explore the mechanism of EGF-induced SHIP2 phosphorylation and its potential impact on the phosphatase activity of the enzyme.

2.2. To optimize PH domain-based biosensors for improved detection of plasma membrane PIP_3:

- To evaluate the impact of targeted mutations that disrupt non-lipid interactions on the localization and performance of Akt and GRP1 PH-domains.
- To adapt the novel biosensors for compatibility with diverse experimental methodologies, including live-cell imaging and BRET-based approaches.

3. Methods

3.1. Cell culture

HEK293-AT1 cells, a stable HEK293-derived line expressing the type-1A rat angiotensin II receptor (AT1AR) (75), along with HEK293A cells (Thermo Fisher Scientific, Cat. No. R70507) and HeLa cells (ATCC, CCL-2), were used in this study. All cell lines were maintained in Dulbecco's modified Eagle's medium (DMEM; Gibco, Cat. No. 11995065) supplemented with 10% fetal bovine serum (FBS; Biosera, FB-1200), 50 U/ml penicillin, and 50 µg/ml streptomycin (Gibco, Cat. No. 15140-122). HEK293-AT1 cells were additionally treated with 5 µg/ml Plasmocin (InvivoGen, ant-mpp) to prevent mycoplasma contamination and were routinely tested to confirm mycoplasma-free status. Cells were cultured in 10 cm culture dishes and maintained at 37°C in a humidified incubator with 5% CO_2.

3.2. DNA constructs

To investigate receptor-specific phosphoinositide signaling, a range of expression constructs were used or generated during this study.

EGFR constructs:

The coding sequence of the human epidermal growth factor receptor (EGFR), previously described in the literature, was cloned into the pEGFP-N1 vector (Clontech) containing either the cytomegalovirus (CMV) or thymidine kinase (TK) promoter. In these constructs, the EGFP coding region was replaced by the EGFR sequence using NheI and Bsp1407I restriction enzymes.

BRET-based biosensors:

Previously established bioluminescence resonance energy transfer (BRET) biosensors specific for PIP_3 and $PI(3,4)P_2$ were used, including:

- L10-mVenus-T2A-Btk-PH-Luciferase
- L10-mVenus-T2A-NES-Luciferase-GRP1-PH
- L10-mVenus-T2A-Luciferase-TAPP1-2xPH

To improve sensor sensitivity and affinity, tandem PH domain-containing variants were generated.

- Btk tandem constructs (L10-mVenus-T2A-Btk-2xPH-Luciferase and mVenus-Btk-2xPH): A second Btk-PH domain was inserted between the first PH domain and luciferase coding region using the AgeI restriction site. The two PH domains were linked by the DPPVAAGAGGAG sequence.
- GRP1 tandem constructs (L10-mVenus-T2A-NES-Luciferase-GRP1-2xPH): A second GRP1-PH domain was inserted between the first GRP1-PH and luciferase sequences using the BglII restriction site, linked by the SSREGS sequence.

Mutant constructs:

GRP1-PH domain biosensors containing point mutations (I307E and K340L) were created by replacing the wild-type PH domain in the above constructs using BglII and EcoRI restriction enzymes. Fluorescent protein-tagged versions of both monomeric and tandem GRP1-PH constructs were generated by inserting the PH domain sequence into a pEGFP-C1 backbone in which the GFP was replaced with an N-terminal nuclear export signal (NES)-tagged Venus fluorescent protein.

SHIP2 constructs:

Mammalian expression plasmids encoding either wild-type (WT) or phosphatase domain-deleted (PD) human SHIP2 were obtained from Addgene (Plasmid #214907 and #214901, respectively).

All constructs were verified by DNA sequencing prior to use in experiments.

3.3. Confocal microscopy

HEK293-AT1 or HEK293A cells were seeded at a density of 3×10^4 cells per well onto poly-L-lysine-coated IBIDI 8-well µ-Slides (Cat. No. 80826). Poly-L-lysine coating was performed using a 0.001% solution for 1 hour at room temperature. Cells were cultured in DMEM at 37 °C for 24 hours prior to transfection.

Transfection was carried out by replacing the culture medium with 200 µl of transfection mixture per well, containing 0.2 µg total plasmid DNA and 0.33 µl

Lipofectamine 2000 (Thermo Fisher Scientific, Cat. No. 11668019). After 6 hours of incubation at 37 °C, the transfection medium was replaced with 300 µl of fresh DMEM supplemented with FBS and antibiotics. Cells were imaged 24-26 hours post-transfection.

For microscopy, cells were examined using a Zeiss LSM 710 laser confocal microscope equipped with a 63×/1.4 oil-immersion objective. The microscope objective was maintained at 30 °C where indicated. Prior to imaging, cells were serum-depleted for 5 hours, and the medium was replaced with a modified Krebs-Ringer buffer (120 mM NaCl, 4.7 mM KCl, 1.2 mM $CaCl_2$, 0.7 mM $MgSO_4$, 10 mM glucose, and 10 mM Na-HEPES, pH 7.4) at room temperature. For stimulation experiments, EGF or insulin were added in an additional volume of 100 µl.

Image analysis was performed using Fiji (ImageJ) and Adobe Photoshop. Only linear adjustments were applied during image processing to preserve data integrity.

3.4. Bioluminescence resonance energy transfer (BRET) measurements

BRET assays were performed to monitor dynamic changes in plasma membrane phosphoinositide levels in living cells. HEK293-AT1, HEK293A, or HeLa cells were first dissociated using 0.25% trypsin (Lonza, BE17-160E) and subsequently seeded onto poly-L-lysine-coated white 96-well plates (Greiner Bio-One, Cat. No. 655083) at a density of 6×10^4 cells per well. The coating was performed with 0.001% poly-L-lysine for 1 hour at room temperature. Transfection was carried out simultaneously by adding 0.03-0.04 µg of total plasmid DNA and 0.25 µl Lipofectamine 2000 per well in Opti-MEM reduced serum medium (Gibco, Cat. No. 31985047).

For optimal receptor expression, both HEK-derived cell lines were transfected with EGFR plasmids, as our previous work has demonstrated variable endogenous EGFR expression across HEK cell populations. Serum starvation was carried out for 5 hours prior to BRET measurements in most experiments, unless otherwise specified (as is the case when comparing serum-rich and serum-deprived conditions in Figure 3).

BRET measurements were carried out 28 hours post-transfection. Before data acquisition, the medium was replaced with 50 µl per well of modified Krebs–Ringer buffer and cells were incubated for 1 hour at 37 °C. For pre-treatment experiments, chemical agents were added 30 minutes prior to measurement. Measurements were conducted at 37 °C using a Varioskan LUX Multimode Microplate Reader (Thermo

Fisher Scientific). The assay was initiated by adding 40 µl of 5 µM coelenterazine-H (Regis Technologies, 1-361304-200), a membrane-permeable luciferase substrate, and luminescence was recorded at 480 nm and 530 nm using emission filters with a detection time of 250 ms per wavelength.

Reagents used for stimulation were freshly prepared in modified Krebs-Ringer buffer and added in a volume of 20 µl per well. In the case of vanadate treatment, a working solution was freshly prepared by mixing 30 µM hydrogen peroxide and 100 µM sodium orthovanadate in a 1:1 ratio immediately prior to application.

All BRET measurements were performed in two biological replicates. Emission signals at 530 nm and 480 nm were used to calculate BRET ratios (530 nm/480 nm), which reflect proximity-based energy transfer between donor and acceptor fluorophores. Because absolute BRET values can vary depending on biosensor expression levels, data normalization was performed. To this end, basal (resting) levels were set to 100%, while 0% was defined using a control construct expressing cytoplasmic luciferase alone.

3.5. Knockdown experiments

For gene knockdown experiments, cells were seeded in 6-well culture plates at a density of 1.5×10^5 cells per well. After 24 hours, the culture medium was replaced with fresh DMEM, and small interfering RNA (siRNA) transfection was performed using a 200 µl mixture containing 6 µl of Lipofectamine RNAiMAX (Thermo Fisher Scientific, Cat. No. 13778150) per well, along with 120 pmol of the respective siRNAs.

Targeted gene silencing was achieved using ON-TARGETplus SMARTpool siRNA reagents (Horizon Discovery), which consist of a mixture of four individual siRNA sequences directed against a single gene target. The following siRNA pools were used: SHIP2 (Cat. No. L-004152-00-0005), PI3KC2A (Cat. No. L-006771-00-0005), and PI3KC2B (Cat. No. L-006772-00-0005). A non-targeting siRNA pool (ON-TARGETplus Non-targeting Pool; Cat. No. D-001810-10-05) served as the negative control.

Forty-eight hours post-siRNA transfection, cells were transfected for either subsequent BRET assays or protein analysis by immunoblotting, as described in the corresponding sections.

3.6. Western blot

Western blot analysis was primarily employed to assess the phosphorylation status of SHIP2, although additional signaling proteins were also examined. Cells were cultured in 6-well plates at a density of 4×10^5 cells per well in DMEM and incubated at 37 °C. The following day, only HEK293A cells were subjected to transient transfection using a 200 µl mixture containing 0.5 µg/well of the indicated EGFR expression plasmids and 2 µl/well of Lipofectamine 2000. HeLa cells were used without transfection to allow the analysis of endogenous EGFR responses.

Approximately 23 hours after seeding (in case of HeLa) or transfection (in case of HEK293A), cells were serum-starved for 5 hours to induce a quiescent state. Where applicable, pharmacological pretreatments were applied 30 minutes prior to stimulation, as specified in the figure legends. Agonist stimulation was typically performed for 5 minutes unless stated otherwise, after which cellular responses were rapidly terminated by placing the plates on ice. Wells were then washed with ice-cold modified Krebs–Ringer buffer, and cells were lysed by scraping in 2× Laemmli buffer supplemented with 5% 2-mercaptoethanol and protease/phosphatase inhibitors (cOmplete Protease Inhibitor Cocktail, Roche, Cat. No. 11836145001). Lysates were stored at -80 °C until use.

Immediately prior to electrophoresis, lysates were sonicated briefly and boiled at 95 °C for 10 minutes. Equal volumes (15 µl) of each sample were loaded onto 4-15% SDS-polyacrylamide gradient gels (Bio-Rad, Cat. No. 4561083). Gel electrophoresis was performed at 100 V for 10 minutes, followed by 130 V for 80 minutes. Proteins were then transferred onto polyvinylidene difluoride (PVDF) membranes (Bio-Rad, Cat. No. 1704156) using the Trans-Blot Turbo Transfer System (Bio-Rad).

Membranes were blocked for 1 hour at room temperature in TBST containing 5% fat-free milk powder. Primary antibodies were diluted 1:1000 in the same blocking solution and incubated with the membranes overnight at 4 °C. On the next day, after three 10-minute washes with TBST, membranes were incubated for 1 hour at room temperature with the appropriate horseradish peroxidase (HRP)-conjugated secondary antibody: either anti-rabbit (Cell Signaling Technology, #7074) or anti-mouse (Cell Signaling Technology, #7076), diluted 1:5000 in TBST with 5% milk. Membranes were washed again three times in TBST before signal detection.

Protein bands were visualized using enhanced chemiluminescence with the Immobilon Western HRP substrate reagent and imaged with an Azure c600 imaging system. Quantification of band intensities was performed using ImageJ software, with background subtraction applied to all measurements. Western blot data shown in the figures represent results from at least three independent experiments.

The following primary antibodies were used:

- Rabbit anti-phospho-SHIP2 (Tyr986/987, Cell Signaling Technology, #2008)
- Rabbit anti-phospho-SHIP2 (Tyr1135, Thermo Fisher Scientific, PA5104651)
- Rabbit anti-SHIP2 (Cell Signaling Technology, #2839)
- Rabbit anti-Akt (Cell Signaling Technology, #4691)
- Rabbit anti-phospho-Akt (Ser473, Cell Signaling Technology, #4060)
- Rabbit anti-ERK1/2 (Cell Signaling Technology, #9102)
- Mouse anti-phospho-ERK1/2 (Thr202/Tyr204, Cell Signaling Technology, #9106)
- Mouse anti-EGFR (Santa Cruz Biotechnology, sc-373746)
- Mouse anti-phospho-EGFR (Tyr1068, Cell Signaling Technology, #2236)

3.7. Statistical analysis

All statistical analyses were performed using SigmaPlot version 10.0. The specific statistical tests applied to each dataset, including post hoc tests following ANOVA where appropriate, are detailed in the respective figure legends. Prior to hypothesis testing, the software automatically evaluated for normal distribution and equal variance of the data. Parametric tests, such as t-test or ANOVA, were employed only when both criteria were satisfied. Otherwise, non-parametric alternatives, such as ANOVA on ranks, were applied.

Sample sizes for each experimental condition are provided in the figure legends. All quantitative results are expressed as the mean ± SD.

4. Results

4.1. Characterization of PH domain-based biosensors for monitoring plasma membrane phosphoinositides

To investigate PI dynamics at the PM, we took advantage of the principle that specific lipid-binding domains, most notably PH domains, enable recruitment of cytosolic proteins to membranes in a phosphoinositide-dependent manner. By genetically fusing these domains to fluorescent proteins, we generated sensors capable of reporting on the subcellular distribution of PIPs, particularly under varying stimulatory conditions.

In our study, for the selective detection of PIP_3, we employed two distinct PH domain constructs derived from GRP1 and Btk, both of which have been extensively validated in prior studies (34, 55, 67, 68). Additionally, for the detection of $PI(3,4)P_2$, we used the PH domain construct based on TAPP1 in tandem (TAPP1-2xPH), a well-established probe for this lipid species.

Initial characterization of these constructs was carried out using confocal microscopy in HEK293-AT1 cells, a modified HEK293 cell line stably expressing the rat angiotensin II receptor type 1A. Cells were transiently transfected to express either a membrane-anchored Venus, a yellow fluorescent protein which was directed to the PM using the Lck targeting sequence (L10-Venus), or Venus-tagged PH domain constructs. Given the known dependence of PIP_3 synthesis as well as the synthesis of other PIP species on growth factor signaling, we compared cells cultured under normal serum conditions (control) with those subjected to 5 hours of serum withdrawal (5 hr SD). As anticipated, the L10-Venus construct remained confined to the PM in all conditions, serving as a stable membrane marker. In contrast, the PH domain-containing sensors showed condition-dependent localization: under serum-rich conditions, GRP1-PH displayed prominent PM association, while Btk-PH and TAPP1-2xPH were more cytosolic, with the latter showing faint membrane localization. Upon serum deprivation, both Btk-PH and TAPP1-2xPH were completely confined to the cytosol. GRP1-PH also showed reduced membrane localization, however, a notable fraction of the sensor remained associated with the PM **(Figure 3A)**.

To enable more sensitive and quantitative assessment of plasma membrane-associated phosphoinositides, we adapted our constructs for use in bioluminescence resonance energy transfer (BRET) assays. For this, the lipid-binding domains were fused to luciferase, serving as the BRET donor, while the membrane-anchored Venus construct was employed as the acceptor. Both donor and acceptor were encoded within the same plasmid construct, separated by a T2A sequence. This sequence ensures that translation is interrupted at this site and equimolar expression of the two proteins, which is essential for reliable and interpretable BRET measurements. The arrangement of the used BRET constructs is shown in **Figure 3B**. This setup allows for real-time detection PIP dynamics at the plasma membrane, where increased binding of the sensor to membrane-localized phosphoinositides brings the donor and acceptor into closer proximity, resulting in an elevated BRET signal. A detailed description of this method has been published previously (67, 76).

We then used our BRET constructs and assessed the basal BRET signals, measured prior to any external stimulation, as indicators of the resting membrane localization and relative affinity of our biosensors. In agreement with the confocal microscopy observations, GRP1-PH exhibited a markedly higher basal BRET ratio under serum-rich conditions compared to Btk-PH and TAPP1-2xPH, reflecting its stronger association with the plasma membrane. Upon serum starvation, the basal BRET signals for both GRP1-PH and TAPP1-2xPH were significantly reduced, consistent with diminished levels of PIP_3 and $PI(3,4)P_2$ at the membrane under growth factor-depleted conditions **(Figure 3C)**.

These comparative analyses underscore fundamental differences in the behavior of the GRP1 and Btk PIP_3 sensors. The observed divergence in their dynamics and localization justified the use of both GRP1-PH and Btk-PH biosensors in subsequent experiments to obtain a broader view of PIP_3 dynamics across various cellular states.

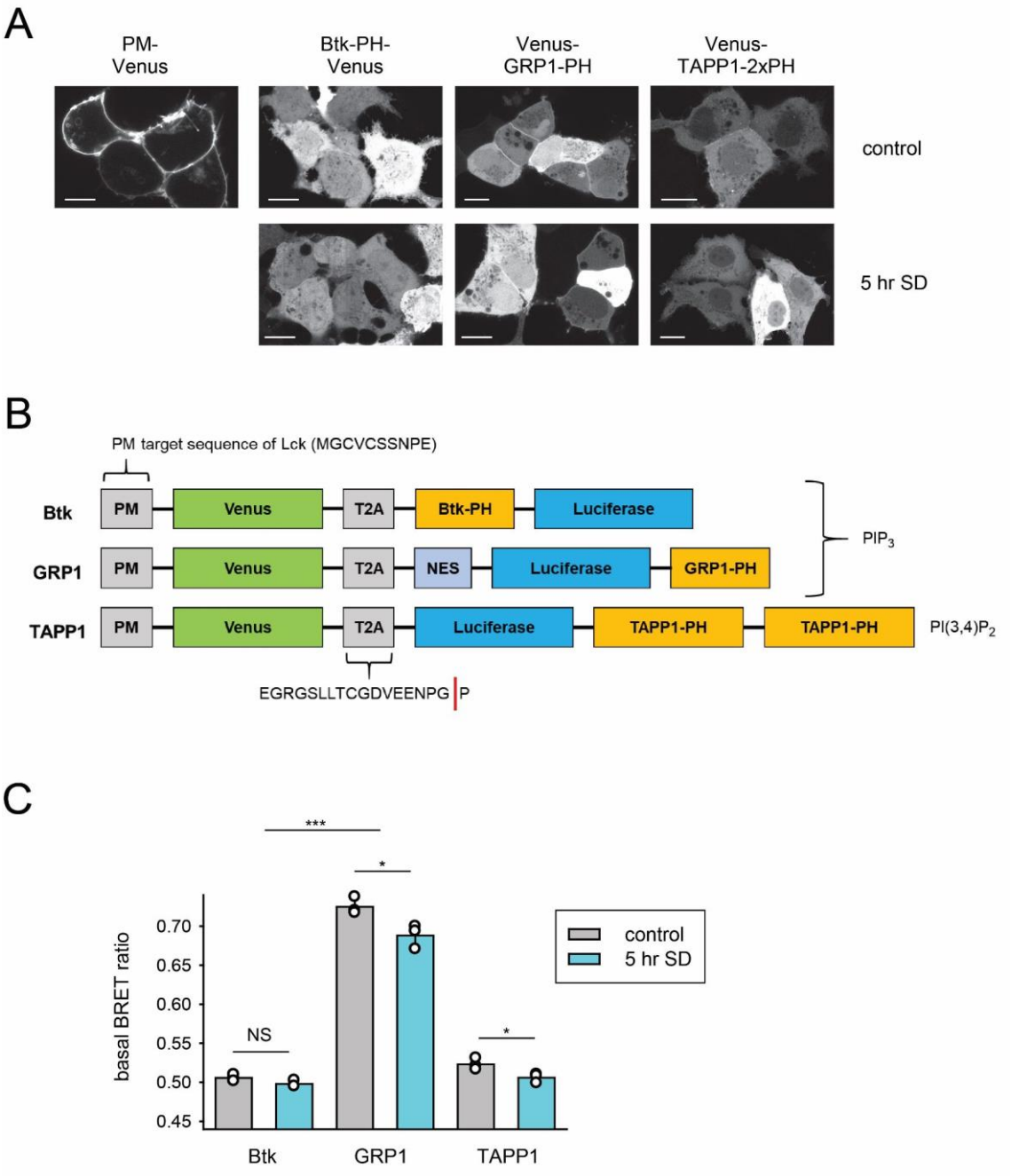

Figure 3. Characterization and evaluation of the biosensors used for following PM phosphoinositides. (**A**) Representative confocal images of HEK293-AT1 cells expressing plasma membrane-targeted Venus or Venus-tagged PH-domains. Images are shown for cells under control conditions and after 5 hours of serum deprivation, for comparison. Scale bar: 10 μm. (**B**) Illustration of the domain architecture of the BRET-based biosensors used in this study. "PM" denotes the plasma membrane targeting sequence derived from Lck (L10), and "T2A" refers to a viral peptide sequence. Although these constructs are transcribed as a single mRNA, translation is interrupted at the T2A site (indicated by the red line), resulting in two distinct polypeptides and ensuring equimolar amounts of both BRET donor and acceptor. (**C**) Bar graph showing the basal BRET ratios of the indicated biosensors measured in serum-rich or serum-deprived conditions. Data

represent mean ± SD from 3 independent experiments. Statistical analysis was performed using two-way ANOVA and Holm–Sidak post hoc test. Only relevant comparisons are shown: *$p < 0.05$, ***$p < 0.001$; NS: not significant ($p > 0.05$). NES: nuclear export signal; SD: serum deprivation. Source: own figure (77).

4.2. Using our BRET-based sensors to follow PIP dynamics following EGF and insulin stimulation in HEK293-AT1 cells

To investigate stimulus-specific changes in plasma membrane phosphoinositide composition, we utilized the BRET-based biosensors described previously in HEK293-AT1 cells. We focused our investigation on the effects of stimulating RTKs, such as EGFR, which are known activators of PI3K signaling pathways that produce both PIP_3 and $PI(3,4)P_2$.

Initially, we examined the cellular response to EGF. For this, cells were transiently co-transfected with the biosensor constructs alongside the EGFR, in order to account for the unpredictable expression of endogenous EGFR observed in HEK293-derived lines. 28 hours later and following 5 hours of serum deprivation, cells were stimulated with EGF (100 ng/ml), and the resulting changes in BRET signal were measured. In this context, an increase in BRET ratio reflects enhanced membrane association of the sensor and is interpreted as a rise in the corresponding lipid at the plasma membrane. EGF stimulation produced a modest elevation in PIP_3 levels, as detected by both the GRP1-PH and Btk-PH sensors. In contrast, the TAPP1-2xPH sensor showed a robust increase in $PI(3,4)P_2$ with EGF stimulation (**Figure 4A**, blue traces).

To validate the observed PIP_3 dynamics and assess sensor performance under a different RTK signaling context, we compared the EGF-induced response with that elicited by insulin. Cells were treated with 70 nM insulin, a concentration chosen to match the magnitude of the $PI(3,4)P_2$ response observed with EGF. Under these conditions, insulin stimulation resulted in a substantially larger increase in PIP_3 levels compared to EGF, in addition to elevating $PI(3,4)P_2$ (**Figure 4A**, red traces).

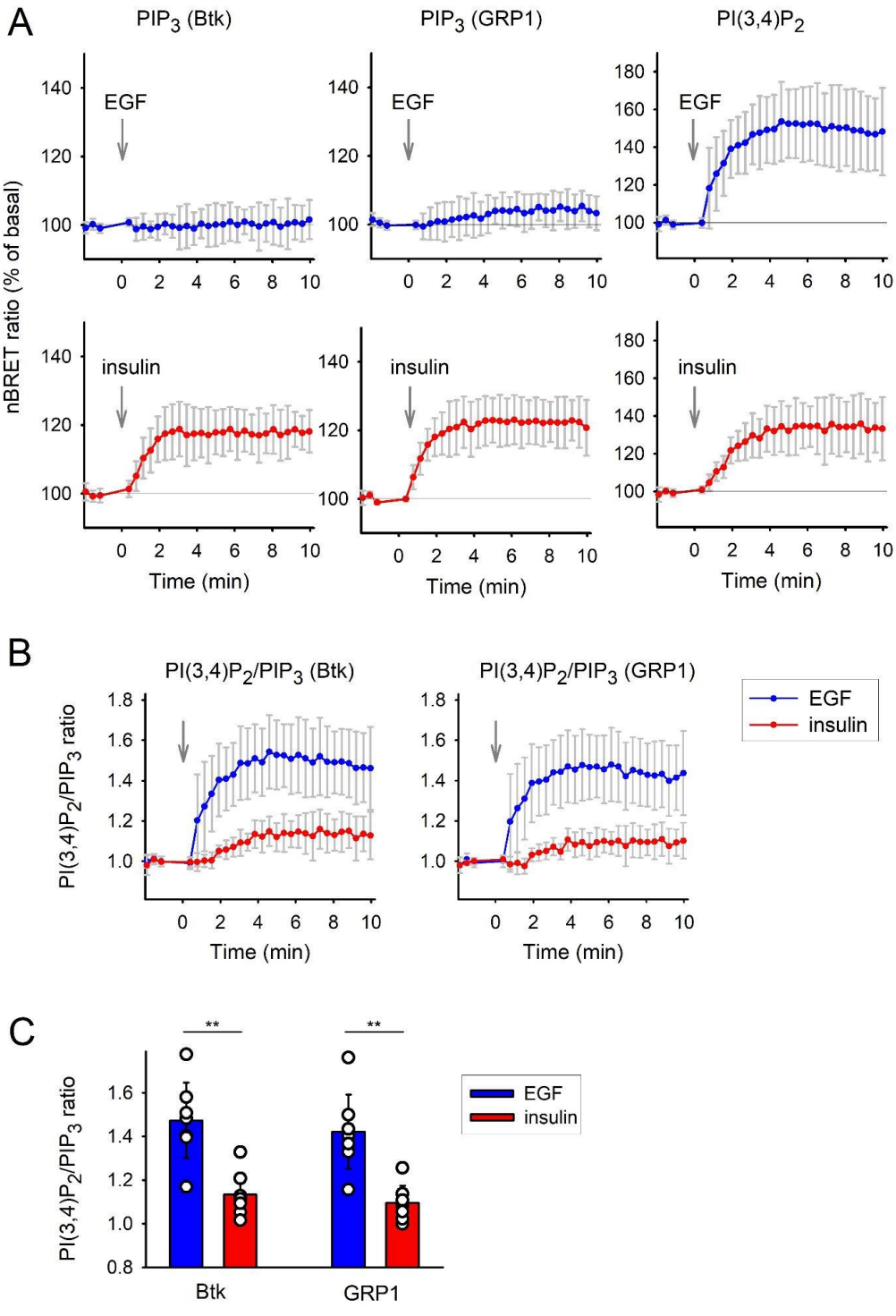

Figure 4. Analysis of plasma membrane phosphoinositide dynamics in response to EGF and insulin stimulation in HEK293-AT1 cells. (**A**) Real-time BRET measurements were used to monitor PM levels of PIP_3 and $PI(3,4)P_2$ following stimulation. HEK293-AT1 cells were transiently transfected with an EGFR expression construct driven by the CMV promoter, along with phosphoinositide biosensors: Btk-PH or GRP1-PH for PIP_3 detection, and TAPP1-2xPH for $PI(3,4)P_2$ detection. Twenty-eight hours post-

transfection, and after 5 hours of serum deprivation, cells were stimulated with either EGF (100 ng/ml, blue curves) or insulin (70 nM, red curves) at the time point indicated by the arrows. BRET ratios were calculated and normalized to baseline levels (set to 100%). Data represent mean ± SD from 7 independent experiments, each conducted in duplicate. (**B**) To highlight differences in the lipid responses to the two stimuli, $PI(3,4)P_2/PIP_3$ ratios were calculated by using the TAPP1-2xPH signal with either the Btk-PH or GRP1-PH signal for PIP_3. (**C**) Bar graphs display the $PI(3,4)P_2/PIP_3$ ratio at the end of the stimulation period, calculated as the mean of the last 5 time points shown in panel B. Comparisons between EGF and insulin conditions were performed using unpaired, two-tailed t-tests for each sensor. **$p< 0.01$. Source: own figure (77).

To more clearly illustrate the relative differences in lipid generation between the two stimuli, we calculated the ratio of $PI(3,4)P_2/PIP_3$ under both EGF and insulin treatment. These ratios were derived by comparing the TAPP1 sensor response to that of either the Btk- or GRP1-based PIP_3 sensors. Notably, EGF stimulation yielded significantly higher $PI(3,4)P_2/PIP_3$ ratios than insulin **(Figure 4B-C)**, suggesting that the balance of phosphoinositide production is stimulus-dependent and that EGF favors the accumulation of $PI(3,4)P_2$ relative to PIP_3 more strongly than insulin does.

4.3. Effect of EGF and insulin stimulation on PIP_3 and $PI(3,4)P_2$ levels in HEK293A cells

To validate and expand upon our findings obtained in the HEK293-AT1 cell line, we next investigated phosphoinositide dynamics in HEK293A cells, a more commonly utilized and broadly characterized human embryonic kidney cell line. In this experimental series, we introduced a newly engineered BRET-based biosensor, Btk-2xPH, a tandem construct designed to enhance PIP_3-binding affinity relative to the previously employed single-domain Btk-PH sensor. This design was intended to address the lower basal BRET ratio observed with Btk-PH in comparison to GRP1-PH (see **Figure 3C**), which reflects its weaker affinity for PIP_3.

Using confocal microscopy, we evaluated the subcellular localization of the tandem sensor. Under serum-deprived conditions, Btk-2xPH exhibited predominantly cytosolic localization. However, following insulin treatment (70 nM), the sensor rapidly translocated to the plasma membrane, indicating effective PIP_3 recognition **(Figure 5A)**. To complement this, we quantified the basal BRET ratios of the PIP_3 and $PI(3,4)P_2$ biosensors in HEK293A cells under serum-starved conditions, revealing subtle

differences when compared to the values obtained in HEK293-AT1 cells (**Figure 5B** compared to **Figure 3C**).

To investigate the impact of ligand dose on phosphoinositide signaling, we extended our analysis to include two concentrations of insulin (70 nM and 0.7 μM), alongside EGF (100 ng/ml). Cells were co-transfected with EGFR and the relevant BRET biosensors for PIP_3 (Btk-PH, GRP1-PH, and Btk-2xPH) and $PI(3,4)P_2$ (TAPP1-2xPH). Twenty-eight hours post-transfection, and following a 5-hour serum starvation period, cells were stimulated and BRET ratio changes were recorded. As shown in **Figure 5C**, both EGF and low-dose insulin elicited comparable increases in PIP_3 levels. However, EGF induced a more pronounced elevation in $PI(3,4)P_2$. Notably, high-dose insulin stimulation resulted in a larger increase in both measured PIP species compared to the lower concentration. Importantly, across all conditions, the tandem Btk-2xPH sensor consistently exhibited greater sensitivity to PIP_3 changes than its single-domain counterpart, supporting its superior binding affinity and utility for dynamic membrane lipid monitoring.

Next, we calculated the $PI(3,4)P_2/PIP_3$ ratio as an indicator of differential lipid dynamics between signaling pathways. Similar to our observations in HEK293-AT1 cells, stimulation with EGF produced higher $PI(3,4)P_2/PIP_3$ ratios than insulin, regardless of the PIP_3 sensor employed. Importantly, this trend persisted across both insulin concentrations, with no significant difference between the low- and high-dose conditions **(Figure 5D)**. Statistical analysis confirmed that the EGF-induced ratios were significantly elevated relative to both insulin treatments **(Figure 5E)**.

To better resolve the early dynamics of lipid signaling, we remeasured the $PI(3,4)P_2/PIP_3$ ratio using the newly developed tandem Btk-PH biosensor, this time employing the highest temporal resolution achievable in our BRET system (sampling every 2 seconds). This high-resolution analysis revealed a biphasic response pattern upon EGF stimulation: an initial, transient decrease in the ratio occurred immediately after ligand addition, followed by a gradual rise to a stable plateau level **(Figure 5F)**.

Interestingly, while the overall response patterns were conserved between HEK293-AT1 and HEK293A cells, the absolute $PI(3,4)P_2/PIP_3$ ratios differed between

the two lines. Specifically, HEK293A cells exhibited lower ratio values when calculated using the GRP1-PH sensor, compared to those observed in HEK293-AT1 cells (compare **Figures 5D-E and 4B-C**). Nevertheless, the relative difference between EGF and insulin stimulation was maintained, reinforcing the reproducibility of this signaling distinction across cellular models.

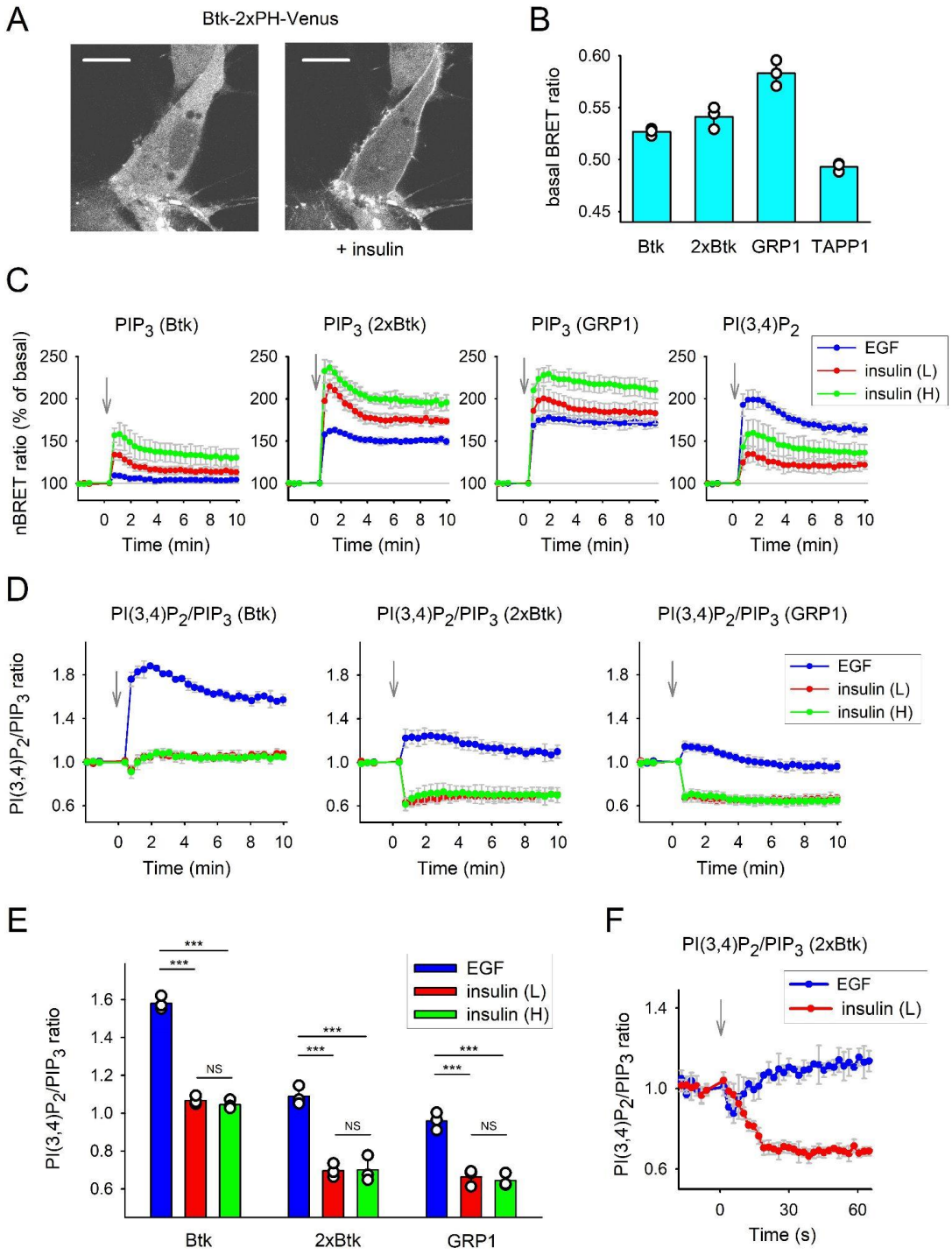

Figure 5. Effects of EGF and insulin stimulation on PM PIP levels in HEK293A cells. (**A**) Confocal microscopy was used to assess the intracellular distribution of the tandem Btk-2xPH PIP_3 biosensor tagged with Venus. Representative images show HEK293A cells following 5 hours of serum starvation, captured immediately before and 3 minutes after stimulation with 70 nM insulin. Scale bar: 10 μm. (**B**) Pre-stimulation (basal) BRET ratios of the indicated biosensors were measured in serum-starved HEK293A cells. Data are mean ± SD from 3 independent experiments. (**C**) BRET-based monitoring of PM phosphoinositide levels in response to RTK stimulation. HEK293A cells were co-transfected with a CMV-driven EGFR expression construct and one of the following biosensors: Btk, 2xBtk, or GRP1 for PIP_3, or TAPP1 for $PI(3,4)P_2$. 28 hours post-transfection and after a 5-hour serum starvation period, cells were stimulated with EGF (100 ng/ml; blue), low-dose insulin (70 nM; red), or high-dose insulin (0.7 μM; green), at the time point indicated by arrows. BRET ratios were normalized to pre-stimulation baselines (set to 100%) and are presented as mean ± SD from 3 independent experiments, each performed in duplicate. (**D**) To compare PIP dynamics of the stimuli, the $PI(3,4)P_2$ and PIP_3 BRET signals were used to calculate $PI(3,4)P_2/PIP_3$ ratios, applying each of the three PIP_3 sensors, as indicated. (**E**) Quantification of the last 5 measurement points from the $PI(3,4)P_2/PIP_3$ ratios (panel D) for each stimulus. Statistical comparisons were performed using one-way ANOVA followed by Holm–Sidak post hoc testing, separately for each biosensor. ***$p<0.001$; NS: $p>0.05$. (**F**) High-resolution temporal analysis of $PI(3,4)P_2/PIP_3$ ratio dynamics using the 2xBtk sensor. Experimental conditions mirrored those in panel D, with the exception that BRET data were acquired at the highest achievable temporal resolution (every 2 seconds). Results are shown as mean ± SD from 3 independent experiments. Source: own figure (77).

4.4. Dissecting the role of SHIP2 and class II PI3Ks in the EGF-induced PIP profile

Previous results from both HEK293-AT1 and HEK293A cell lines demonstrated that EGF stimulation leads to a disproportionate elevation of $PI(3,4)P_2$ relative to PIP_3 at the plasma membrane. To elucidate the enzymatic mechanisms underlying this shift in PM PIP levels, we focused on two established synthetic routes of $PI(3,4)P_2$ production: the dephosphorylation of PIP_3 by SHIP2, and the direct phosphorylation of PI4P by class II PI3Ks (78). These pathways and the specific molecular interventions we used to target them are summarized in **Figure 6A**.

Our investigation began in HEK293-AT1 cells, where we employed siRNA-mediated knockdown to selectively silence SHIP2 or class II PI3K isoforms. Forty-eight hours post-transfection, cells were co-transfected with EGFR and phosphoinositide biosensors, GRP1-PH or TAPP1-2xPH, to monitor PIP_3 and $PI(3,4)P_2$ dynamics, respectively. Following an additional 28-hour incubation and serum starvation, cells were stimulated with EGF, and BRET signals were recorded. SHIP2 knockdown resulted in a modest elevation of PIP_3 levels, but significantly blunted the $PI(3,4)P_2$ response compared

to control cells (**Figure 6B**, orange vs. black curves). In contrast, knockdown of class II PI3Ks led to a pronounced increase in EGF-induced $PI(3,4)P_2$ levels (**Figure 6B**, green curves). These opposing effects were reflected in the $PI(3,4)P_2/PIP_3$ ratios, where SHIP2 depletion reduced the ratio, while class II PI3K knockdown increased it, relative to control **(Figure 6C)**.

To validate the central role of SHIP2 in $PI(3,4)P_2$ generation, we repeated the knockdown experiments in HEK293A cells, this time targeting only SHIP2. Consistent with our earlier findings, SHIP2 silencing led to a mild accumulation of PIP_3 upon EGF stimulation, but a marked reduction in $PI(3,4)P_2$ production **(Figure 6D)**, resulting in a significantly lower $PI(3,4)P_2/PIP_3$ ratio compared to controls **(Figure 6E)**. These results strongly suggest that SHIP2 activity is the principal driver of EGF-induced $PI(3,4)P_2$ accumulation in both HEK cell models.

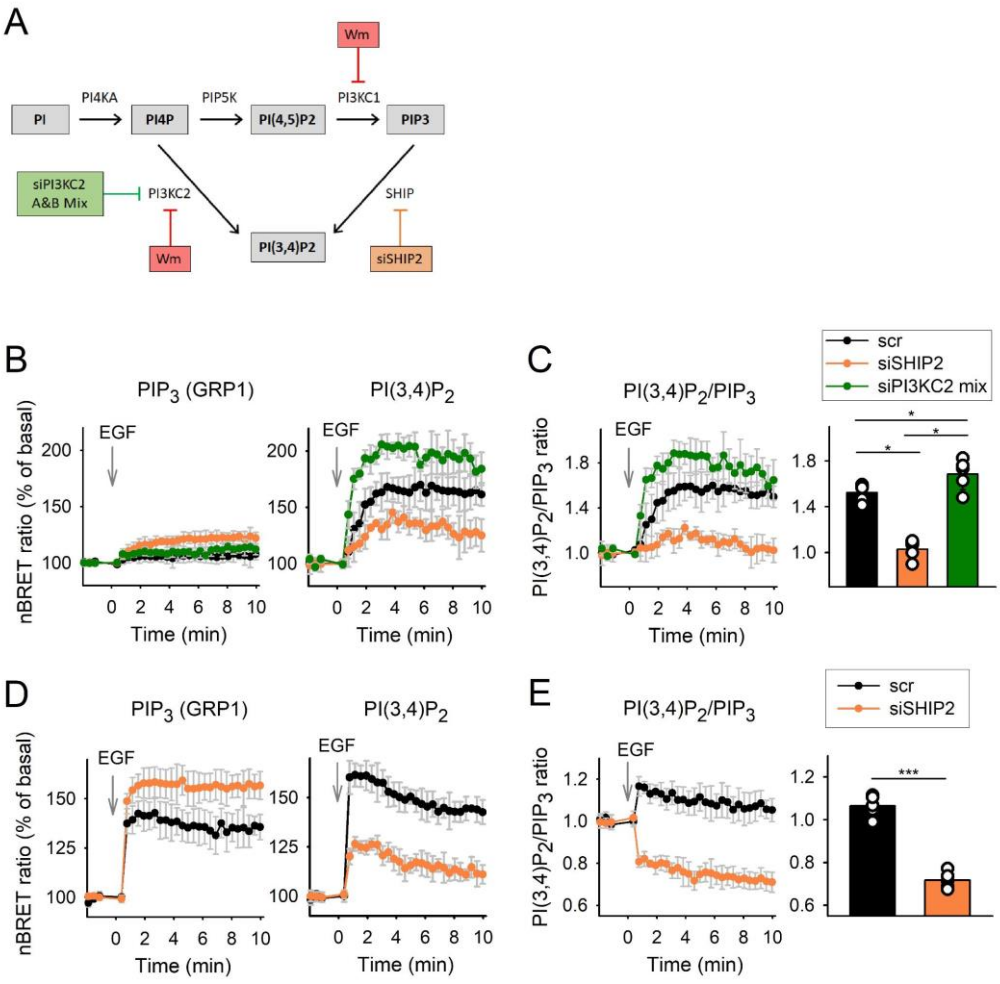

Figure 6. SHIP2 regulates $PI(3,4)P_2$ production in response to EGF stimulation (**A**) Overview of the two principal biosynthetic routes leading to $PI(3,4)P_2$ accumulation at the plasma membrane. The diagram also outlines the siRNAs and pharmacological tools used to selectively inhibit these pathways. (**B**) BRET measurements of PIP_3 and $PI(3,4)P_2$ dynamics in HEK293-AT1 cells following targeted gene silencing. Cells were first transfected with control (scr), SHIP2-specific (siSHIP2), or class II PI3K-specific (siPI3KC2) siRNAs. After 48 hours, cells were co-transfected with a CMV-driven EGFR expression construct and either the GRP1-PH biosensor (for PIP_3) or the TAPP1-2xPH biosensor (for $PI(3,4)P_2$). Following an additional 28-hour period and 5 hours of serum starvation, cells were stimulated with EGF (100 ng/mL) and BRET signals were calculated and normalized to pre-stimulation baselines. Curves represent mean ± SD (n=5). (**C**) Effects of SHIP2 and class II PI3K knockdown on the $PI(3,4)P_2/PIP_3$ ratio in HEK293-AT1 cells. Bar graph values represent the final phase of the measurement window (last 5 measurement points)**.** Statistical comparisons were made using ANOVA on ranks with Student-Newman-Keuls post hoc test. *$p<0.05$. (**D**) BRET analysis in HEK293A cells examining the impact of SHIP2 knockdown on phosphoinositide dynamics in response to EGF. Cells were transfected as described in panel B, and BRET changes were monitored following stimulation. Data are mean ± SD (n=5). (**E**) $PI(3,4)P_2/PIP_3$ ratio in SHIP2-silenced HEK293A cells compared to controls. Bar graph values represent the final phase of the measurement window (last 5 measurement points), and significance was assessed using an unpaired two-tailed t-test. ***$p<0.001$. Source: own figure (77).

We next investigated whether SHIP2 also contributes to $PI(3,4)P_2$ dynamics downstream of insulin signaling. Interestingly, SHIP2 knockdown had no measurable effect on the $PI(3,4)P_2/PIP_3$ ratio following insulin stimulation, implying a more limited role for SHIP2 in regulating the PIP profile in the insulin signaling pathway **(Figure 7A)**.

Although SHIP2 knockdown significantly reduced the $PI(3,4)P_2$ response to EGF, it did not abolish it entirely. To evaluate knockdown efficiency, we performed immunoblotting in HEK293A cells. This confirmed a strong but incomplete reduction in SHIP2 protein levels, while EGFR expression remained unaffected **(Figure 7B)**. To further assess specificity, we carried out rescue experiments in which exogenous expression of wild-type (WT) SHIP2 restored $PI(3,4)P_2$ production following knockdown, whereas a phosphatase-domain deleted (PD) SHIP2 mutant lacking the catalytic domain failed to do so **(Figure 7C)**.

Finally, to determine whether the observed $PI(3,4)P_2$ accumulation resulted from its increased synthesis or reduced degradation, we pretreated HEK293A cells with 300 nM wortmannin (Wm), a PI3K inhibitor, prior to EGF stimulation. Wortmannin

completely suppressed the rise in both PIP_3 and $PI(3,4)P_2$ **(Figure 7D)**, confirming that the $PI(3,4)P_2$ surge is driven by increased synthesis.

Taken together, these results demonstrate that the accumulation of $PI(3,4)P_2$ at the plasma membrane following EGF stimulation is primarily mediated by SHIP2 acting on PIP_3 produced through class I PI3K activity. These findings are further complemented by the biphasic behavior of the $PI(3,4)P_2/PIP_3$ ratio observed in high-resolution temporal analyses **(Figure 5F)**.

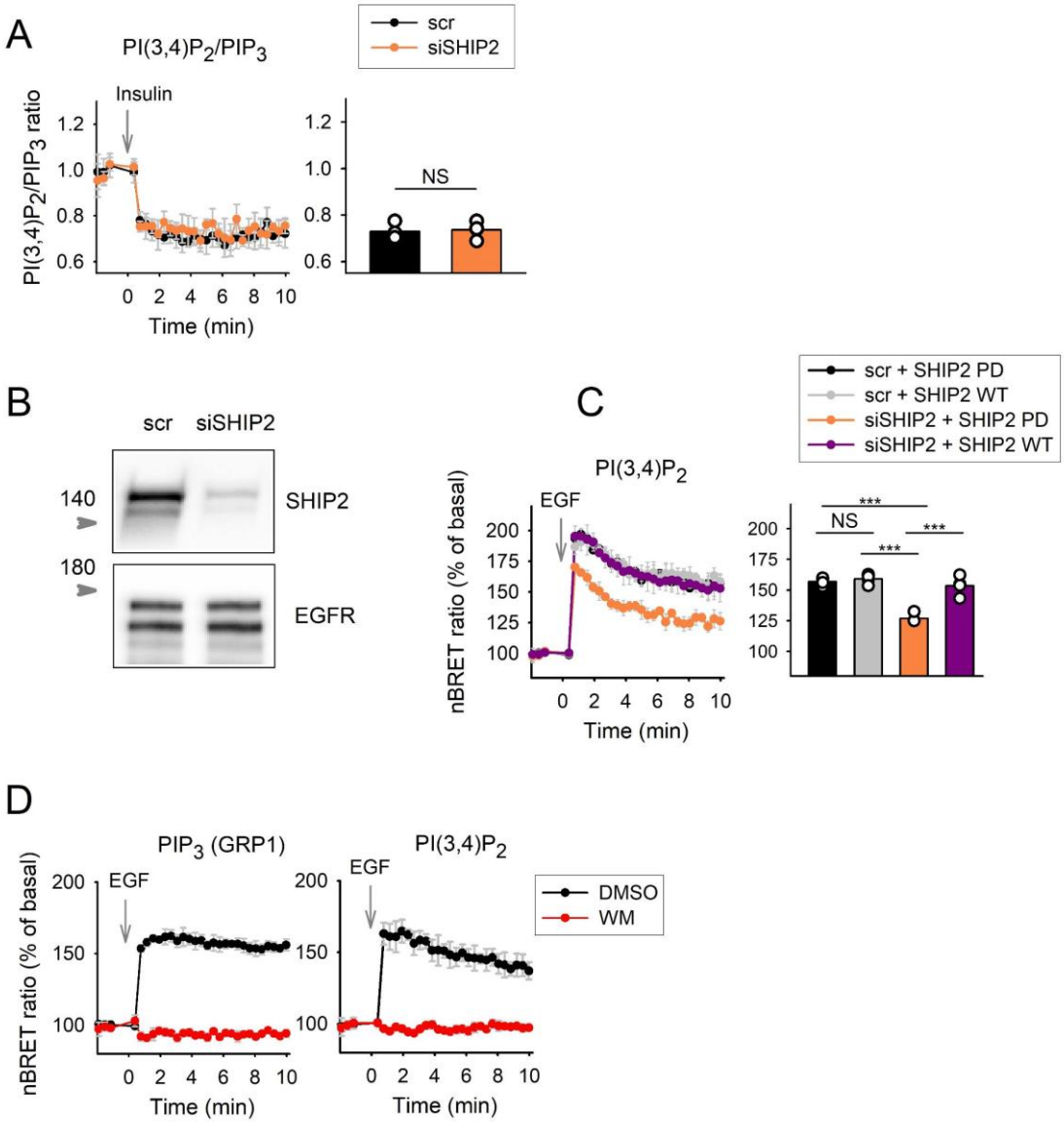

Figure 7. Validation of SHIP2 knockdown and the role of SHIP2 in insulin-induced PIP dynamics. (**A**) The effect of SHIP2 knockdown on the insulin induced $PI(3,4)P_2/PIP_3$ ratio in HEK293A cells. No statistically significant difference was observed (NS: $p > 0.05$,

unpaired two-tailed t-test). (**B**) Immunoblot validation of SHIP2 knockdown efficiency in HEK293A cells using antibodies against SHIP2 and EGFR. (**C**) Rescue experiments to confirm the specificity of SHIP2 knockdown. Cells were co-transfected with indicated siRNA and either wild-type (WT) SHIP2 or a phosphatase-deficient mutant (PD), in addition to EGFR and the $PI(3,4)P_2$ sensor. The bar graph displays the mean ± SD of the last 5 measurement points. Statistical comparisons were made using one-way ANOVA followed by Holm–Sidak post hoc test. ***$p < 0.001$; NS: not significant. (**D**) Inhibition of PI3K activity abolishes EGF-induced phosphoinositide accumulation. HEK293A cells expressing EGFR and phosphoinositide sensors were pretreated for 30 minutes with 300 nM wortmannin or DMSO prior to stimulation. Data are mean ± SD (n=3). Source: own figure (77).

4.5. SHIP2 phosphorylation dynamics in response to EGF and insulin

Having established that SHIP2 is the primary mediator of $PI(3,4)P_2$ accumulation downstream of EGF stimulation, we next sought to investigate its regulatory mechanism. Specifically, we examined the phosphorylation status of SHIP2, which has been associated with increased enzymatic activity (79). To this end, we compared the effects of EGF and insulin stimulation on SHIP2 phosphorylation in HEK293A cells.

To assess the influence of EGFR expression levels on SHIP2 regulation, cells were transfected with EGFR under the control of two different promoters: the cytomegalovirus (CMV) promoter to drive high-level overexpression and the thymidine kinase (TK) promoter to achieve more moderate, physiologically relevant expression. Twenty-eight hours post-transfection, cells were serum-starved for five hours and then stimulated for 5 minutes with either EGF (100 ng/mL) or insulin at low (70 nM) or high (0.7 µM) concentrations. Protein lysates were subsequently analyzed via Western blotting.

EGF stimulation led to robust phosphorylation of SHIP2 at both tyrosine residues 986/987 and 1135. In contrast, no phosphorylation was detected following insulin treatment, even at tenfold the used concentration **(Figure 8A)**. As anticipated, SHIP2 phosphorylation was more pronounced under high EGFR expression conditions, yet remained detectable with moderate EGFR expression levels.

To confirm that the concentration of the stimuli that we applied is effective and comparable we examined their effect on two additional pathways: Akt, a PI3K-dependent effector activated by both EGF and insulin, and ERK, a PI3K-independent target

selectively activated by EGF (50, 80). Consistent with their signaling specificity, Akt phosphorylation was observed following both stimuli, whereas ERK activation and EGFR phosphorylation were exclusive to EGF-treated cells. These patterns were consistent across both CMV and TK promoter-driven EGFR expression **(Figure 8A)**. Quantification of SHIP2 phosphorylation at Tyr1135 confirmed the observed differences and statistical significance across experimental groups **(Figure 8B).**

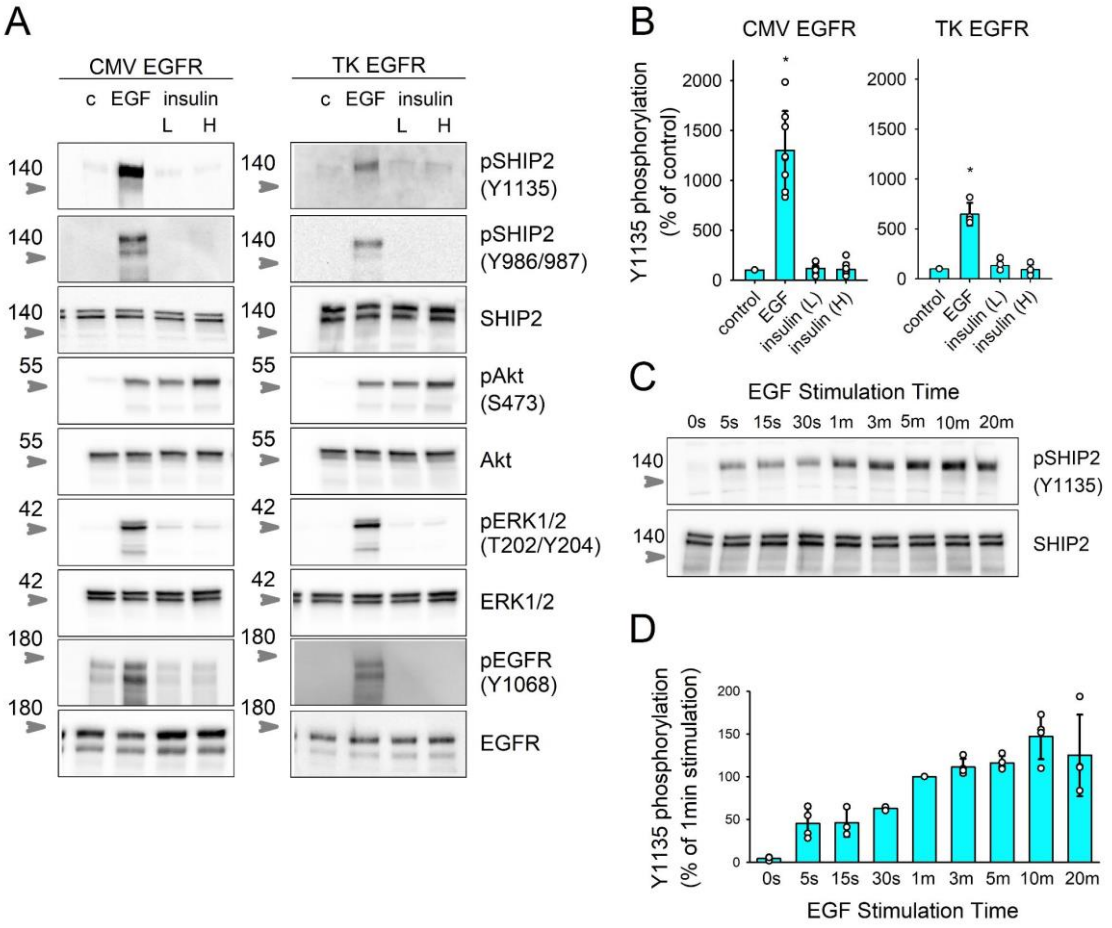

Figure 8. SHIP2 phosphorylation in response to EGFR activation. (**A**) To investigate the regulation of SHIP2 by RTK signaling, HEK293A cells were transfected with EGFR constructs under either the CMV promoter (high expression) or the TK promoter (moderate expression). Following a 5-hour serum starvation period, cells were stimulated for 5 minutes with EGF (100 ng/mL) or insulin at either 70 nM (low) or 0.7 µM (high) concentrations. Protein lysates were subjected to Western blot analysis using antibodies against the relevant total and phosphorylated proteins. Phospho-specific antibodies (denoted by "p-") target specific phosphorylation sites, as indicated in parentheses. Total protein levels served as loading controls, and molecular weight markers (in kDa) are noted with arrows. (**B**) Quantitative analysis of SHIP2 phosphorylation at tyrosine 1135, based on immunoblots shown in panel A. Data are presented separately for cells with high

(left panel) and moderate (right panel) EGFR expression. Values were normalized to unstimulated controls (set to 100%) in each experiment. Bar graphs represent the mean ± SD (n=8). Statistical significance was assessed using ANOVA on ranks followed by the Student–Newman–Keuls post hoc test. EGF stimulation induced a statistically significant increase in SHIP2 phosphorylation compared to all other conditions (*$p<0.05$). (**C**) Time-course analysis of SHIP2 phosphorylation at Tyr1135 following EGF stimulation. HEK293A cells overexpressing EGFR (CMV-driven) were stimulated for varying durations ranging from 5 seconds to 20 minutes, as indicated above each lane. The upper panel shows phospho-SHIP2 (Tyr1135), while the lower panel displays total SHIP2. The 140 kDa molecular weight marker is indicated. (**D**) Densitometric quantification of pSHIP2 (Tyr1135) from panel C. Values were normalized to the 1-minute stimulation time point (set to 100%) in each experiment. Data are mean ± SD (n=3-4). Source: own figure (77).

Given that our BRET-based lipid monitoring indicated that phosphoinositide dynamics are initiated rapidly following EGF stimulation **(see Figure 5F)**, we further investigated the temporal profile of SHIP2 phosphorylation at Tyr1135. Using a series of eight EGF stimulation durations, we observed that phosphorylation could be detected as early as 5 seconds after ligand addition, increasing progressively to peak levels at around 10 minutes **(Figures 8C-D)**. This finding strongly supports the notion that SHIP2 activation is an early and sustained event within the EGF signaling cascade.

To rule out the possibility that EGFR overexpression could artifactually affect lipid dynamics, we performed comparative BRET measurements under three expression conditions: endogenous EGFR, moderate overexpression via TK promoter, and high overexpression via CMV promoter. Across all conditions, EGF stimulation produced qualitatively similar $PI(3,4)P_2$ and PIP_3 responses, although higher receptor expression was associated with more sustained signaling kinetics (**Figure 9**, top panels). Notably, insulin-induced lipid profiles were unaffected by EGFR overexpression (**Figure 9**, bottom panels). Together, these findings show that the $PI(3,4)P_2$ increase with EGF stimulation can be attributed to the phosphorylation-driven activation of SHIP2, at functionally relevant tyrosine sites.

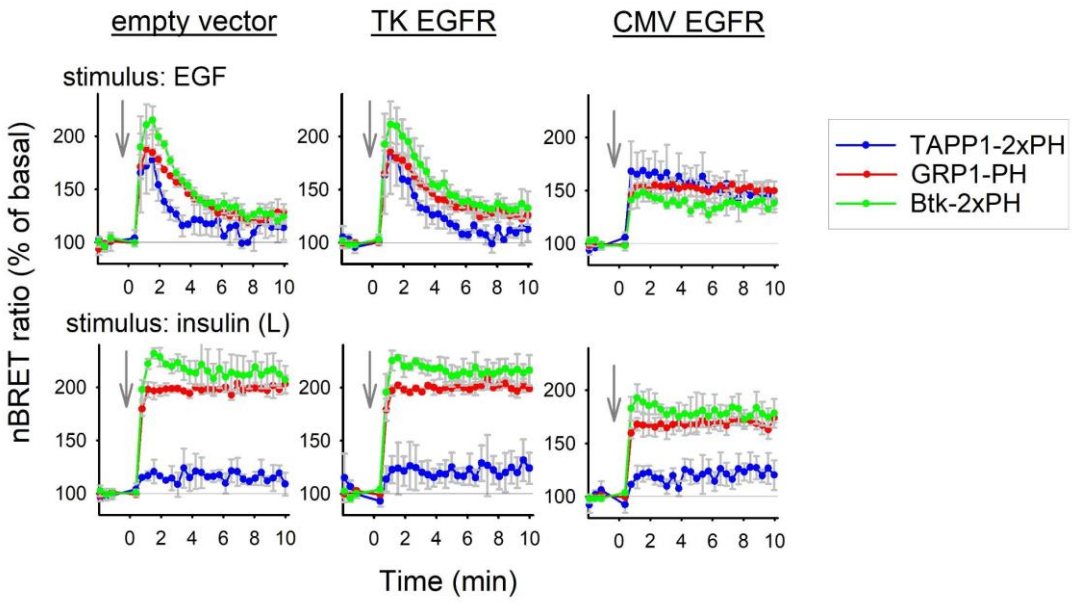

Figure 9. The effect of EGFR overexpression level on PIP signaling pattern. BRET-based measurements of PIP_3 and $PI(3,4)P_2$ levels in HEK293A cells expressing EGFR at different levels (CMV, TK, or endogenous) and co-transfected with the appropriate phosphoinositide biosensors (as described in Figure 5). Following serum starvation, cells were stimulated with EGF (100 ng/mL) or insulin (70 nM), and BRET ratios were calculated. Arrows indicate the time of stimulation. Data are shown as mean ± SD (n=3). Source: own figure (77).

4.6. Phosphoinositide signaling dynamics in HeLa cells with endogenous EGFR expression

While HEK293-derived cell lines have proven useful for dissecting phosphoinositide signaling, their variable endogenous EGFR expression often necessitates artificial receptor overexpression to ensure consistent responsiveness to EGF. To evaluate whether the observed lipid signaling dynamics are representative of physiological conditions, we extended our analysis to HeLa cells, which endogenously express EGFR at stable levels and are known to respond robustly to both EGF and insulin stimulation (81-83).

HeLa cells were transfected with biosensors specific for PIP_3 and $PI(3,4)P_2$, and 28 hours later serum starved cells were treated with EGF (100 ng/mL) or insulin (70 nM), and changes in BRET ratios were calculated. The resulting phosphoinositide profiles were similar to those observed in HEK293A and HEK293-AT1 cells. Specifically, insulin elicited a greater increase in PIP_3 levels, whereas EGF produced a more substantial

accumulation of PI(3,4)P_2 (**Figure 10A**, red and blue curves, respectively). Furthermore, calculation of the PI(3,4)P_2/PIP_3 ratio revealed a consistent trend: EGF stimulation yielded a higher ratio than insulin **(Figures 10B-C)**, mirroring the outcomes previously seen in HEK cell lines. These findings confirm that the surge of PI(3,4)P_2 in response to EGF is not a consequence of EGFR overexpression but is instead a characteristic feature of this signaling pathway.

To further corroborate these results, we performed immunoblotting to assess SHIP2 phosphorylation in HeLa cells following ligand stimulation. Consistent with prior observations in HEK293A cells, EGF, but not insulin, induced phosphorylation of SHIP2 at tyrosine residues 986/987 and 1135 **(Figure 10D)**. All other immunoblotting results were consistent with those seen in HEK293A cells.

Taken together, these results demonstrate that the distinct lipid signaling responses observed following EGF and insulin stimulation are not restricted to HEK-derived cell systems or dependent on EGFR overexpression. Rather, the preferential production of PI(3,4)P_2 in response to EGF, along with the associated SHIP2 phosphorylation, appears to be a generalizable feature of receptor tyrosine kinase signaling in mammalian cells. This reinforces the physiological relevance of our findings and highlights SHIP2 as a key player selectively activated downstream of EGFR.

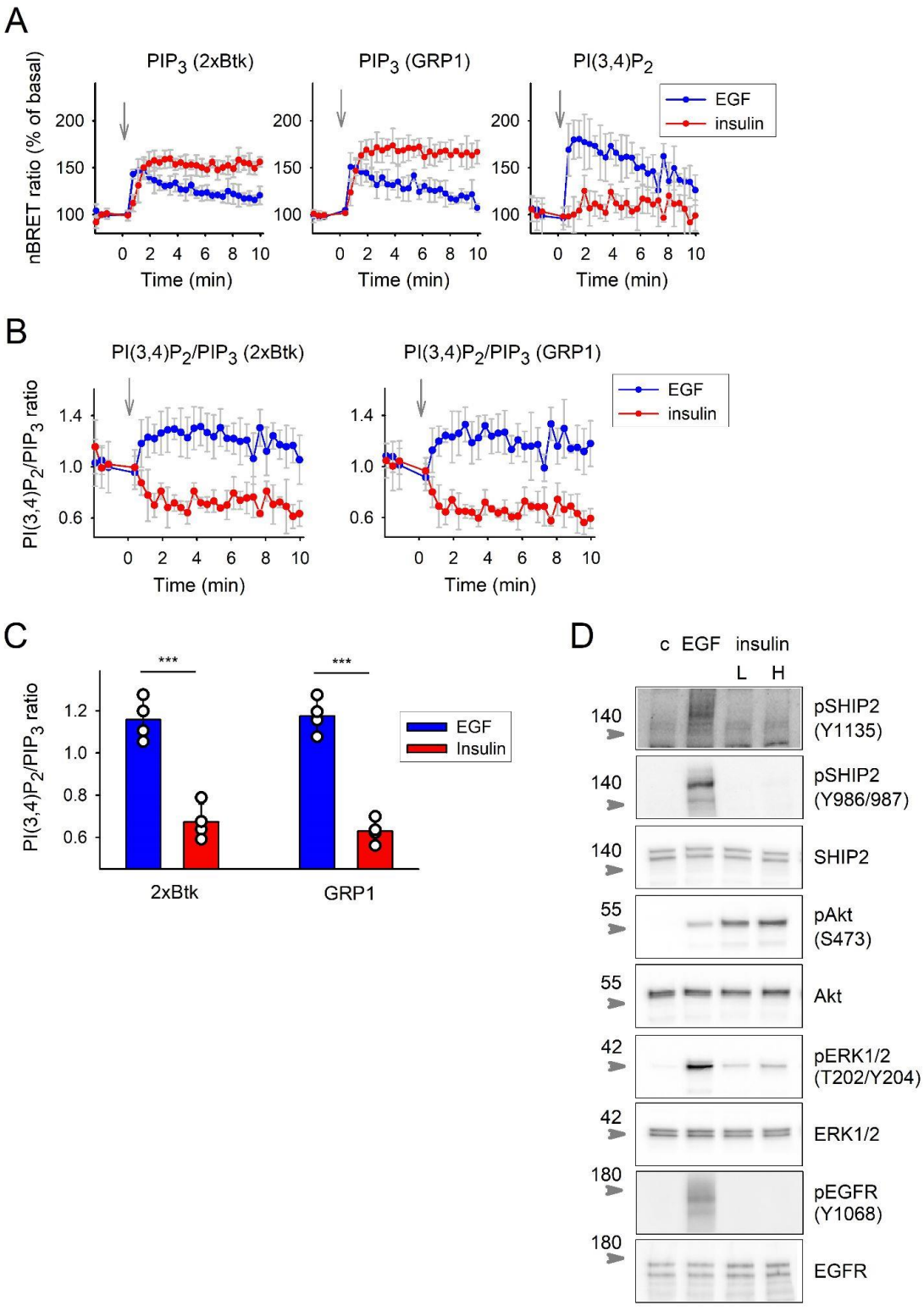

Figure 10. Differential phosphoinositide signaling and SHIP2 phosphorylation in HeLa cells following EGF and insulin stimulation. (**A**) To assess plasma membrane lipid dynamics under physiological EGFR expression, HeLa cells were transiently transfected with the indicated PIP_3 and $PI(3,4)P_2$ biosensors. After 28 hours, cells were stimulated

with either EGF (100 ng/mL; blue curves) or insulin (70 nM; red curves). BRET ratios were calculated and normalized. Data are mean ± SD (n=4). (**B**) PI(3,4)P_2/PIP_3 ratios were calculated in the case of HeLa cells. (**C**) The calculated PI(3,4)P_2/PIP_3 ratios for each treatment are presented as bar graphs, with values representing the average of the final five time points from each BRET time course. Statistical differences between EGF- and insulin-stimulated conditions were determined using unpaired, two-tailed t-tests for each biosensor. ***$p < 0.001$. (**D**) HeLa cells were subjected to the same western blotting analysis conducted in HEK293A cells. Antibodies detecting total protein levels were used as loading controls. Phosphorylation-specific antibodies are denoted by "p" and their respective target residues are indicated in parentheses. Molecular weights (in kDa) are marked alongside each blot with arrows. Source: own figure (77).

4.7. PLCγ-induced calcium signal regulates SHIP2 phosphorylation in EGFR pathway

Having observed robust phosphorylation of SHIP2 in response to EGFR activation, we sought to dissect the upstream mechanisms responsible for this modification. While both EGFR and IR are receptor tyrosine kinases that converge on shared pathways such as PI3K activation, a distinguishing feature of EGFR signaling is its ability to mobilize intracellular calcium through PLCγ activation (50, 51). This prompted us to examine the involvement of both calcium signaling and PI3K activity in SHIP2 phosphorylation.

We first evaluated the role of calcium by pretreating EGFR-transfected, serum-starved HEK293A cells with the calcium chelator BAPTA-AM or DMSO control prior to EGF or insulin stimulation. Western blot analysis revealed that calcium chelation caused a significant reduction in SHIP2 phosphorylation at both Y1135 and Y986/987 following EGF treatment **(Figure 11A)**. To verify the effectiveness of BAPTA-AM, we monitored intracellular calcium changes using our previously established BRET-based calcium biosensor (84). This confirmed that BAPTA-AM effectively suppressed the EGF-induced calcium rise **(Figure 11B)**.

To assess PI3K involvement, we repeated the experiment using the PI3K inhibitor wortmannin. A 30-minute pretreatment partially suppressed SHIP2 phosphorylation in response to EGF, and efficient PI3K inhibition was confirmed via a complete loss of Akt phosphorylation **(Figure 11C)**. Notably, when both pathways were inhibited simultaneously using BAPTA-AM and wortmannin, SHIP2 phosphorylation was further diminished, indicating an additive effect **(Figures 11D-E)**.

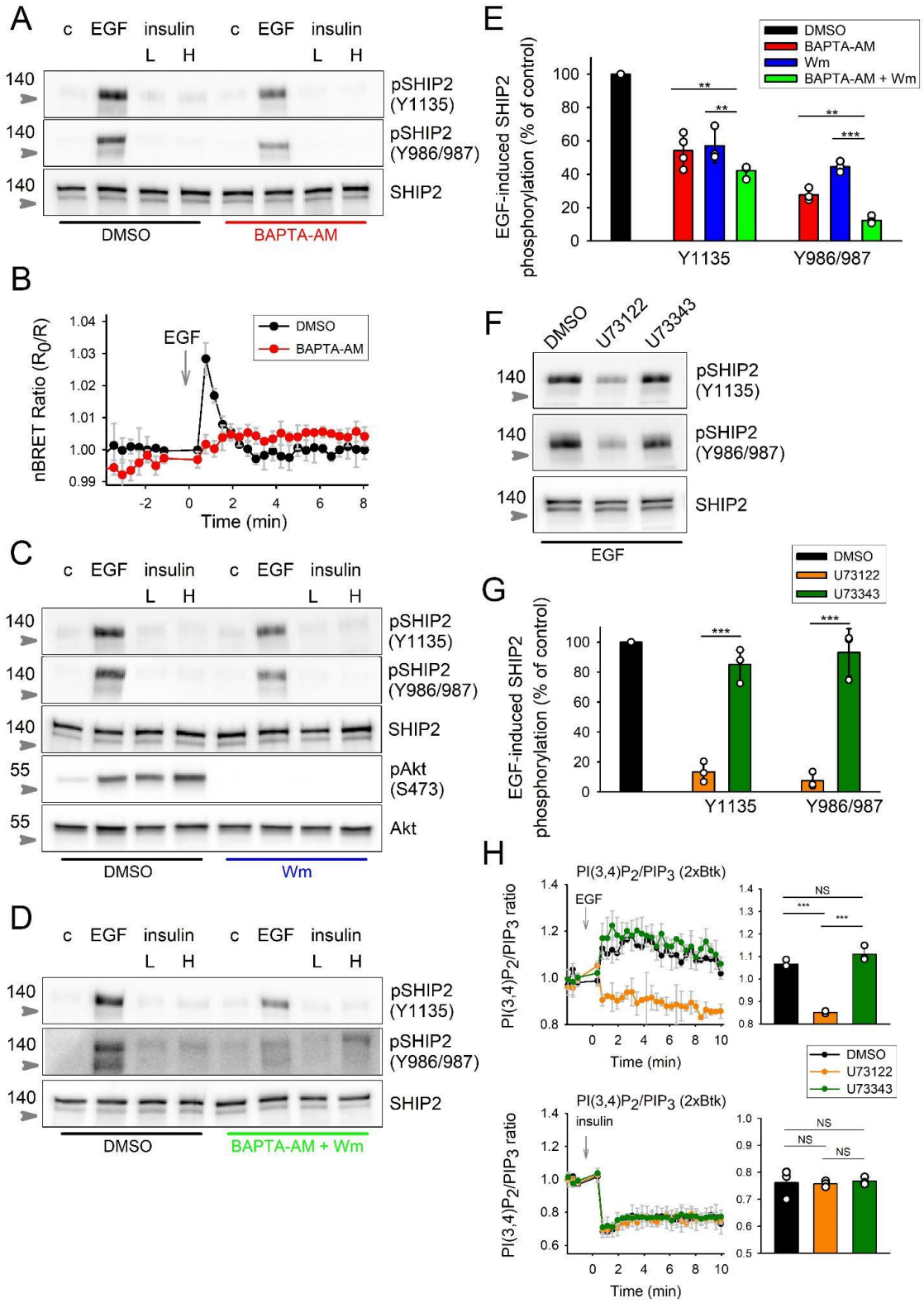

Figure 11. Investigating upstream signaling mechanisms responsible for SHIP2 phosphorylation upon EGF stimulation. (**A**) Western blot showing SHIP2 phosphorylation at Y1135 and Y986/987 in HEK293A cells overexpressing EGFR (CMV), serum-starved, pretreated for 30 min with BAPTA-AM (20 μM) or DMSO, and

stimulated for 5 min with EGF, low-dose (L) or high-dose (H) insulin. Total SHIP2 served as a loading control. (**B**) Cytoplasmic calcium levels measured by BRET confirmed effective buffering by BAPTA-AM after EGF stimulation. (**C-D**) SHIP2 phosphorylation following 30 min pretreatment with wortmannin (100 nM) alone or combined with BAPTA-AM. Akt phosphorylation was tested to ensure effective wortmannin activity. (**E**) Quantification of phospho-SHIP2 levels (Y1135 and Y986/987) under each condition. $^{**}p < 0.01$, $^{***}p < 0.001$. (**F-G**) PLC inhibition with U73122, but not inactive analog U73343, significantly reduced EGF-induced SHIP2 phosphorylation. (**H**) BRET-based analysis of $PI(3,4)P_2/PIP_3$ ratios showed a marked reduction after PLC inhibition with EGF, but not insulin. Bar graphs are the average of the final 5 time points. $^{***}p < 0.001$; NS: not significant. Source: own figure (77).

To directly implicate PLCγ in this process, we utilized the PLC inhibitor U73122 along with its inactive analogue U73343 as a control. Cells pretreated with U73122 showed a marked decrease in EGF-induced SHIP2 phosphorylation at both targeted tyrosine residues, while the control treatments had no effect **(Figure 11F)**. Quantitative analysis confirmed the significance of this inhibition **(Figure 11G)**.

To determine whether this phosphorylation translates to altered SHIP2 function, we examined the impact of PLC inhibition on PIP lipid dynamics using BRET-based biosensors. Following EGF stimulation, PLC inhibition caused a substantial reduction in the $PI(3,4)P_2/PIP_3$ ratio, suggesting impaired SHIP2-mediated lipid conversion. In contrast, insulin-induced responses remained unchanged **(Figure 11H)**.

In summary, these findings identify both calcium mobilization and PI3K activity as important contributors to SHIP2 phosphorylation following EGFR activation. Specifically, PLCγ-dependent calcium signaling plays a central role in this process and directly influences SHIP2 function at the plasma membrane, thereby shaping the distinct phosphoinositide pattern downstream of EGFR.

4.8. Evaluation of GRP1-PH and Akt-PH mutants for specific detection of PM PIP_3 dynamics

PH domains are widely utilized in biosensor design due to their ability to bind specific phosphoinositides, allowing monitoring of lipid signaling dynamics. However, PH domains are also known to engage in lipid-independent interactions with proteins, which can confound the interpretation of lipid-specific responses. To address this, we investigated the performance of engineered PH domain variants that retain lipid-binding

capability without protein-binding affinity. Our goal was to evaluate whether such mutants provide more selective and precise readouts of PM PIP_3 dynamics, independent of protein-mediated recruitment.

We focused on two well-established PIP_3-binding domains: those of GRP1 and Akt. Mutant forms of these domains with impaired protein-protein interaction potential were utilised and compared to the wild-type form. For GRP1-PH, we examined the K340L and I307E mutants, while for Akt-PH, we used the T34L and T34F mutants. All constructs were incorporated into BRET-based biosensor designs, in which the PH domains (wild-type or mutant) were fused to luciferase (BRET donor), while the acceptor fluorophore Venus was anchored to the plasma membrane using an Lck targeting sequence. This donor-acceptor configuration enabled us to monitor the PM localization of each biosensor in living cells with high temporal resolution. All chosen mutants maintain their ability to bind lipids but show disrupted protein interaction capability (61, 69). The used biosensor domain arrangements as well as the mutations sites are shown in **Figure 12A**.

HEK293A cells were used as the experimental model and were co-transfected with the EGFR expression construct, along with one of the biosensors. After 28 hours, serum-starved cells were stimulated with either EGF (100 ng/mL), insulin (70 nM), or sodium orthovanadate (100 nM), the latter serving as a broad-spectrum phosphatase inhibitor known to elevate PIP_3 levels. BRET ratios were then calculated to assess biosensor recruitment to the plasma membrane.

As shown in **Figure 12B**, wild-type GRP1-PH responded robustly to all three stimuli, with significant increases in the BRET ratio indicative of enhanced PM association. In contrast, the K340L and I307E mutants displayed only modest BRET increases under the same conditions. When responses were quantified 10 minutes post-stimulation, both GRP1-PH mutants showed significantly attenuated responses relative to wild-type **(Figure 12C)**, suggesting that a substantial portion of wild-type sensor recruitment is facilitated by protein interactions.

We next applied the same experimental strategy to compare wild-type Akt-PH with its T34L and T34F mutants. While wild-type Akt-PH demonstrated strong BRET

responses to all stimuli (**Figure 12D**, left), both mutants retained a comparable dynamic profile, albeit with slightly reduced amplitude (**Figure 12D**, middle and right). These results suggest that, unlike GRP1-PH, the functionality of Akt-PH biosensors is less reliant on protein-mediated interactions.

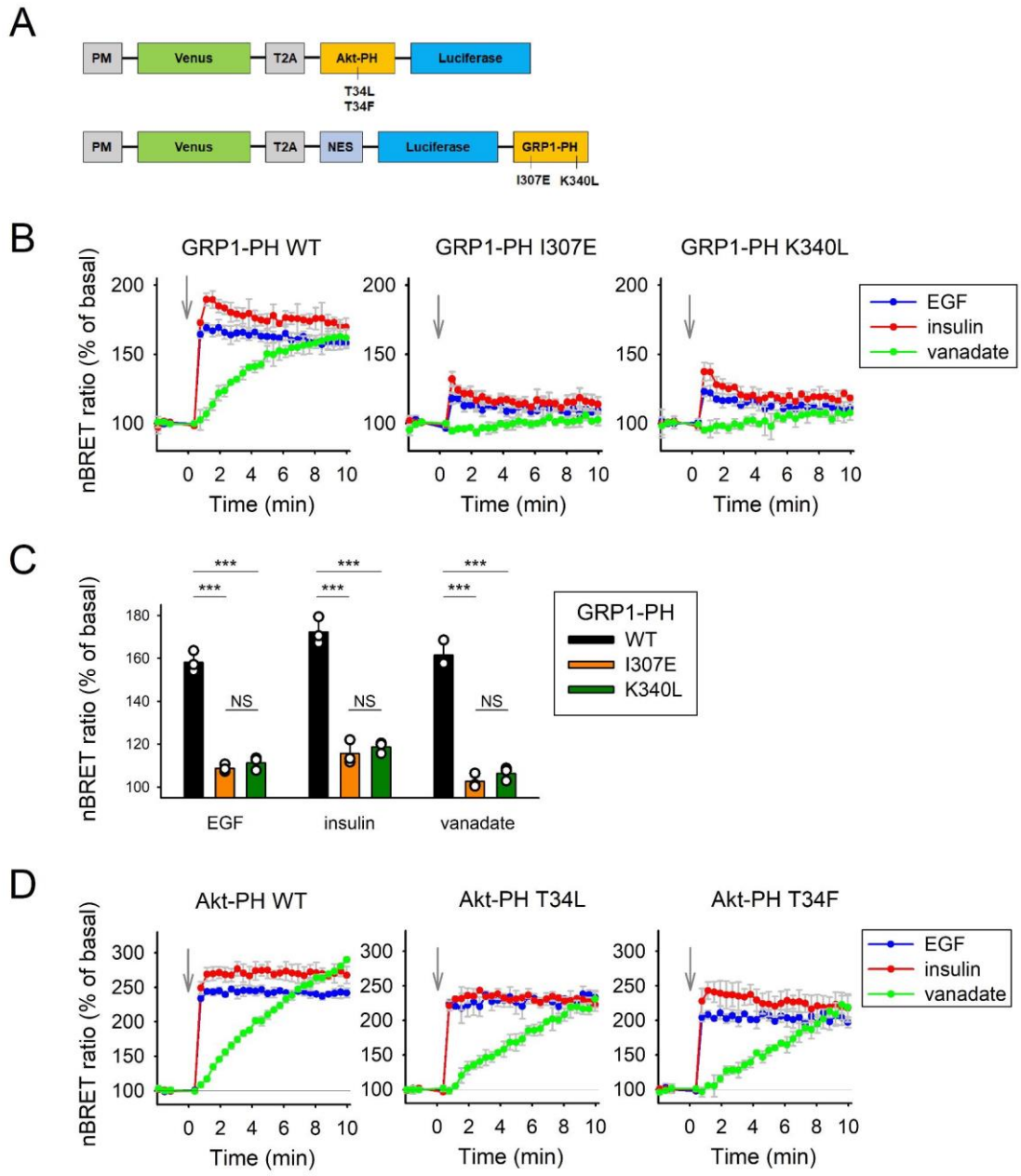

Figure 12. Evaluation of GRP1-PH and Akt-PH biosensor mutants for selective detection of PM PIP_3 dynamics (**A**) Diagram illustrating the structural organization of the BRET-based biosensors used to monitor PIP_3 levels. Each construct consists of a PH domain (from either GRP1 or Akt) fused to luciferase, along with a Venus acceptor directed to the plasma membrane via the Lck targeting sequence. Mutations known to disrupt

protein-protein interactions while preserving lipid binding are indicated within each PH domain. (**B**) PIP_3 dynamics were measured in HEK293A cells using GRP1-PH-based BRET biosensors. Cells were transiently co-transfected with EGFR and either wild-type (WT) or mutant (I307E or K340L) GRP1-PH constructs. After 28 hours, and following 5 hours of serum starvation, cells were stimulated with EGF (100 ng/mL; blue curves), insulin (70 nM; red curves), or sodium orthovanadate (100 nM; green curves). BRET ratios were then calculated and normalized. Results are presented as mean ± SD (n=3). (**C**) To quantitatively compare the performance of WT and mutant GRP1-PH biosensors, the final 5 data points from each curve in panel B were averaged and statistically analyzed. One-way ANOVA followed by Holm–Sidak post hoc testing was applied separately for each stimulus. Significant differences between WT and mutant responses are indicated (*** $p<0.001$; NS: not significant). (**D**) A similar experimental approach was used to evaluate Akt-PH-based BRET sensors. Cells were transfected with EGFR and either WT or mutant (T34L or T34F) Akt-PH constructs. Treatments, BRET ratio normalization, and analysis were performed as described in panel B. Data are shown as mean ± SD (n=3). Source: own figure (85).

In summary, our comparative analyses revealed that protein interactions play a significant role in the membrane recruitment of the GRP1-PH biosensor, complicating its interpretation in dynamic signaling contexts. While the use of GRP1-PH mutants can eliminate this confounding factor, their diminished sensitivity limits their utility for detecting subtle lipid changes. In contrast, the strong membrane recruitment observed with Akt-PH mutants indicates that their performance is less reliant on non-lipid interactions.

4.9. Improving the affinity and performance of mutant GRP1-PH-based biosensors through tandem domain engineering

In our earlier experiments, GRP1-PH domain mutants demonstrated significantly reduced responsiveness to PIP_3-elevating stimuli compared to their wild-type counterpart (see **Figure 12C**). This attenuation likely stemmed from a decrease in overall membrane affinity due to the loss of protein interactions, despite intact lipid binding. To address this limitation, we constructed tandem versions of these mutant sensors, a widely used strategy known to enhance lipid-binding strength through increased avidity.

Following the established experimental workflow, HEK293A cells were co-transfected with EGFR and the newly designed tandem-domain GRP1-PH mutants. After a 28-hour expression period and 5 hours of serum starvation, cells were stimulated with EGF (100 ng/mL), insulin (70 nM), or sodium vanadate (100 nM), and BRET ratio changes were

monitored. The tandem mutant biosensors displayed markedly greater BRET signal increases in response to all stimuli compared to their single-domain predecessors **(Figure 13A)**, achieving signal amplitudes comparable to the wild-type GRP1-PH sensor (see **Figure 12C**). This enhancement was quantitatively confirmed by averaging the BRET ratios across the final five time points of each stimulation **(Figure 13B)**.

To further assess membrane association, we analyzed the basal BRET ratios (in the absence of stimulation) of all GRP1-PH sensor variants. As anticipated, the wild-type sensor exhibited the highest basal BRET values, reflecting both lipid and protein interactions. In contrast, single-domain mutant sensors showed significantly lower basal ratios, consistent with reduced plasma membrane residency due to the absence of protein-mediated recruitment. Importantly, tandem mutants exhibited a higher basal BRET signal compared to the single mutants, highlighting the increased membrane affinity conferred by the tandem architecture **(Figure 13C)**. These findings collectively indicate that tandem-domain GRP1-PH mutants maintain lipid selectivity while regaining robust membrane targeting, thereby representing an optimized tool for monitoring PIP_3 signaling without protein interaction interference.

To evaluate the spatial distribution and imaging compatibility of these sensors, we performed confocal microscopy on Venus-tagged versions of the wild-type, single-mutant, and tandem-mutant GRP1-PH constructs. In serum-starved HEK293A cells, all biosensors primarily localized to the cytoplasm, with additional nuclear presence observed in all constructs except the K340L single mutant. Upon EGF stimulation, cells expressing the tandem K340L sensor exhibited a rapid and pronounced translocation of the fluorescent signal to the plasma membrane. This confirms not only the sensor's responsiveness to dynamic PIP_3 changes but also its suitability for live-cell imaging applications.

In summary, our tandem-domain GRP1-PH mutants successfully restore membrane affinity and signaling responsiveness lost through mutation, without reintroducing protein-binding artifacts. This makes them highly reliable biosensors for both BRET-based and microscopy-based analyses of PIP_3 dynamics in live cells.

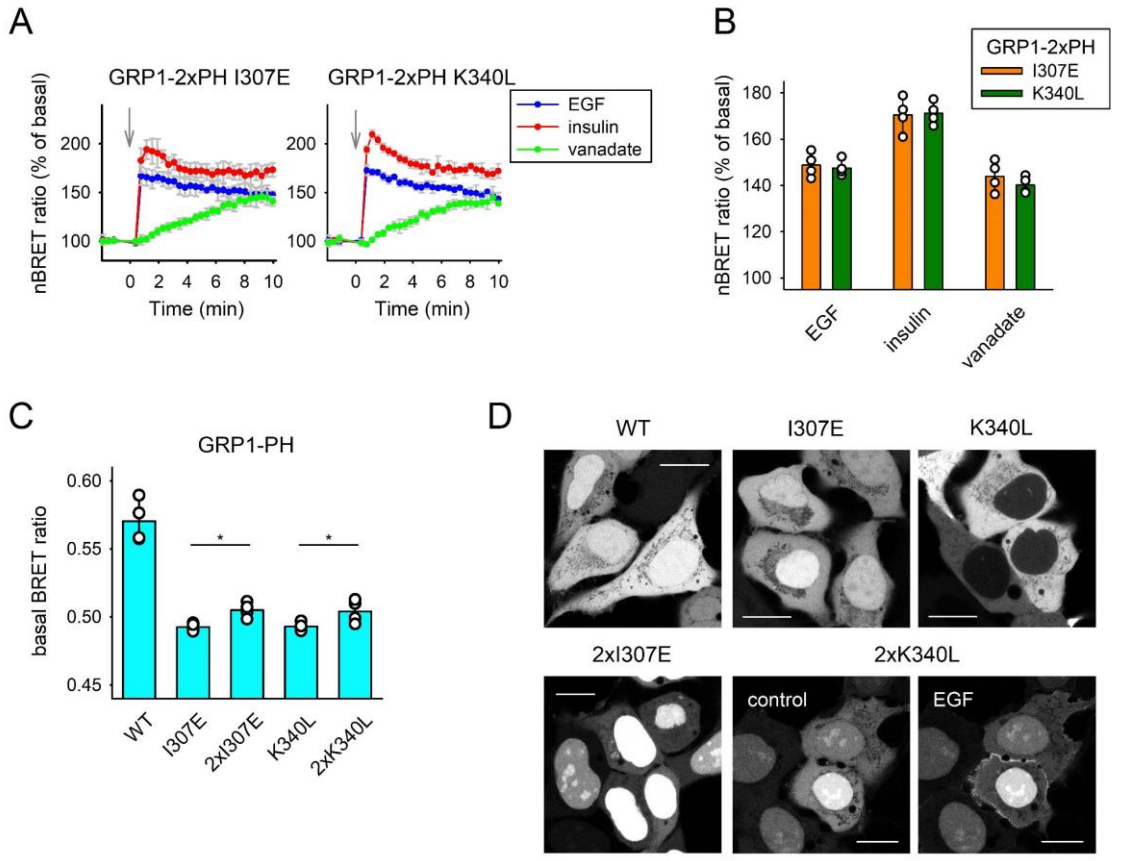

Figure 13. Enhanced PIP_3 detection by tandem-domain mutant GRP1-PH biosensors (**A**) PIP_3 dynamics were monitored in HEK293A cells using tandem-domain GRP1-PH mutants engineered to enhance membrane affinity. Cells were co-transfected with EGFR and either the duplicated I307E or K340L GRP1-PH mutant biosensors. Following 28 hours of expression and 5 hours of serum starvation, cells were stimulated with EGF (100 ng/mL), insulin (70 nM), or sodium orthovanadate (100 nM), and BRET ratio changes were recorded. Experimental conditions and BRET normalization were identical to those described in Figure 11B. Data are mean ± SD (n=4). (**B**) To quantify sensor responsiveness, the final five time points from the curves in panel A were averaged for each condition. Bar graphs depict the mean ± SD for each treatment. (**C**) Basal (pre-stimulation) BRET ratios were compared across wild-type, mutant single-domain, and mutant tandem-domain GRP1-PH biosensors to assess differences in steady-state membrane association. Data were derived from the experiments shown in Figures 11B and 12A. Bar graphs show the mean ± SD from 4 independent experiments. Statistical analysis was conducted using ANOVA on ranks with Student–Newman–Keuls post hoc test, performed separately for each mutation. All mutant constructs showed significantly different basal BRET values compared to wild-type. * $p < 0.05$. (**D**) Representative confocal microscopy images of HEK293A cells expressing Venus-tagged versions of the indicated GRP1-PH constructs under serum-starved conditions. Cells expressing the tandem K340L mutant were also imaged five minutes after EGF stimulation. In these experiments the confocal microscope objective was maintained at 30 °C. Scale bar: 10 µm. Source: own figure (85).

5. Discussion

In this work, we employed a BRET-based approach to monitor dynamic changes in plasma membrane phosphoinositides, particularly focusing on the interplay between PIP_3 and $PI(3,4)P_2$ following receptor tyrosine kinase activation. By comparing cellular responses to EGF and insulin stimulation, it became evident that these two growth factors elicit distinct lipid signaling profiles, despite their many overlapping signaling cascades.

Throughout the study, multiple biosensors were employed to monitor PIP_3 levels, each based on the PH domains of either GRP1 or Btk. Although these constructs contain only the lipid-binding region of their parent proteins, they exhibited differing behaviors under identical experimental conditions. This variability was evident in both the confocal imaging and BRET measurements, where GRP1-PH consistently showed higher membrane association at baseline compared to Btk-PH. These differences are likely attributable to variations in lipid-binding affinity or kinetics, but may also reflect the influence of sensor configuration, including the spatial orientation of the BRET donor and acceptor, which can impact signal strength independently of lipid binding (86). To improve sensitivity and overcome the relatively modest signal amplitude observed with the single Btk-PH sensor, we developed a tandem version with enhanced avidity. This modified sensor exhibited a slightly elevated basal BRET signal and showed a notably larger dynamic range upon receptor stimulation. These results are consistent with previous findings highlighting the very sensitive, threshold-like behavior of Btk's lipid interactions, which are tightly coupled to PIP_3 density at the plasma membrane (87). The improved responsiveness of the tandem sensor makes it a valuable tool for detecting subtle changes in lipid signaling.

One of the central findings of our investigation was the consistently higher $PI(3,4)P_2/PIP_3$ ratio observed after EGF treatment relative to insulin in both HEK-derived and HeLa cells **(Figures 4, 5 and 10)**. This suggests that EGF signaling selectively favors the accumulation of $PI(3,4)P_2$, likely through specific modulation of lipid phosphatases. To dissect the underlying mechanisms, we examined the role of SHIP2, a 5-phosphatase known to convert PIP_3 to $PI(3,4)P_2$. Using targeted siRNA knockdown and rescue strategies, coupled with high time resolution BRET measurements, the data revealed that SHIP2 plays a dominant role in regulating $PI(3,4)P_2$ levels during EGF signaling **(Figures**

6 and 7). This regulatory effect was not observed during insulin stimulation, highlighting a stimulus-specific involvement of SHIP2 in phosphoinositide turnover.

Interestingly, SHIP2 itself underwent phosphorylation at two previously recognized tyrosine residues (79) in response to EGF but not insulin, further pointing to its selective activation within the EGF signaling axis **(Figure 8)**. Investigating this phosphorylation revealed that while class I PI3K activity contributes to SHIP2 modification, the rise in intracellular calcium downstream of PLC appears to be the primary driver. This conclusion was supported by experiments showing that both PI3K inhibition and calcium chelation reduced SHIP2 phosphorylation, with the latter having a more pronounced effect. Moreover, pharmacological inhibition of PLC almost completely abolished SHIP2 phosphorylation and sharply reduced the $PI(3,4)P_2/PIP_3$ ratio following EGF stimulation **(Figure 11)**, suggesting a direct functional link between PLC-mediated calcium signaling and SHIP2 activation.

Further complexity was observed when examining the potential role of class II PI3Ks in $PI(3,4)P_2$ synthesis. Despite previous reports positioning class II enzymes as key sources of $PI(3,4)P_2$ (31), knockdown of class II PI3Ks unexpectedly led to elevated PM $PI(3,4)P_2$ levels after EGF stimulation **(Figure 6)**. One possible explanation is that class II PI3K is required for EGFR internalization (31). Thus, its inhibition could prolong EGFR activity at the PM, indirectly enhancing $PI(3,4)P_2$ synthesis.

To assess how SHIP2 phosphorylation varies over time, we monitored phosphorylation at one of the tyrosine residues following multiple durations of EGF stimulation. Phosphorylation was detectable within seconds and increased progressively, peaking around 10 minutes **(Figure 8)**. These dynamics, together with concurrent high time resolution lipid measurements, imply that tyrosine phosphorylation enhances SHIP2 activity, though whether this effect is mediated by conformational changes, altered localization, or direct catalytic activation remains an open question. Prior reports have offered differing interpretations of SHIP2 phosphorylation, with some suggesting enhancement of activity (79, 88) and others emphasizing the role of membrane recruitment (89).

To validate the relevance of these findings in different experimental systems, we compared results obtained in HEK293-AT1 cells, which we have utilized in several studies (75, 76, 90), with those in HEK293A and HeLa cells. While the general pattern of PIP responses was preserved, notable cell line-dependent differences were observed, particularly in PIP_3 dynamics, which appeared more robust in the HEK293A background and relatively modest in HEK293-AT1 cells. This may reflect variations in basal PI3K activity, as suggested by higher baseline BRET signals in HEK293-AT1 cells. However, despite these baseline differences, the $PI(3,4)P_2/PIP_3$ ratios remained consistent across the cell lines in response to EGF and insulin, reinforcing the robustness of this metric in distinguishing between signaling outputs.

EGFR expression levels were another factor considered. Due to variable endogenous expression in HEK cells, we employed both moderate (TK promoter-driven) and strong (CMV promoter-driven) EGFR overexpression systems in these cells. Lipid dynamics were consistent across all receptor expression levels, suggesting that receptor overexpression does not artificially distort signaling behavior **(Figure 9)**. These findings were corroborated in HeLa cells, which express endogenous EGFR and IR, confirming that the observed signaling patterns are not artifacts of overexpression systems.

The functional relevance of the differential $PI(3,4)P_2$ production between EGF and insulin signaling was explored in the context of Akt isoform activation. Given prior evidence that Akt1 and Akt2 preferentially respond to PIP_3 and $PI(3,4)P_2$ (73), respectively, we hypothesized that EGF stimulation might preferentially activate Akt2 based on its previously detailed PIP profile. However, immunoblot analyses failed to reveal isoform-specific phosphorylation differences between the two stimuli, indicating that additional layers of regulation likely buffer this effect or that Akt activation alone is insufficient to capture the nuanced impact of $PI(3,4)P_2$ dynamics. As this was a negative finding,weI did not include these results in this thesis work.

While PLC inhibition via U73122 provided critical insights into the calcium-dependence of SHIP2 phosphorylation **(Figure 11)**, the known off-target effects (91, 92) and context-dependent behavior of this compound must be acknowledged. Although calcium chelation produced similar results, limitations inherent to the used PLC inhibitor underscore the need for improved pharmacological tools in dissecting PLC-dependent

signaling events (93, 94). Altogether, this work demonstrates that EGF and insulin, despite sharing upstream activation of PI3K, diverge substantially in their control of phosphoinositide signaling, particularly in how they regulate SHIP2 activity and the balance of PIP_3 and $PI(3,4)P_2$ at the plasma membrane. These differences likely contribute to distinct cellular outcomes and highlight the nuanced, context-specific nature of lipid signaling. Understanding these pathways not only enhances our knowledge of receptor-specific signaling but also has potential implications for targeted therapeutic strategies, especially in diseases where phosphoinositide metabolism is dysregulated (48).

In a complementary set of experiments, we sought to improve the specificity and interpretability of PIP_3 biosensors by examining how protein interactions influence their membrane association. To this end, we utilized previously described mutations in the PH domains of Akt and GRP1 that selectively disrupt non-lipid interactions while preserving affinity for PIP_3. These modifications were designed to reduce off-target recruitment driven by interactions with endogenous proteins.

While the mutant Akt-PH constructs showed little change in membrane association compared to the wild-type, similar mutations introduced into GRP1-PH led to a substantial reduction in both basal and stimulus-induced membrane localization after EGF, insulin, or vanadate treatment. This indicates that GRP1-PH membrane binding in cells is more strongly influenced by protein-mediated interactions than that of Akt-PH **(Figure 12)**.

Although these GRP1 mutants displayed improved lipid specificity, their reduced signal amplitude limited their suitability for tracking dynamic lipid changes. To address this limitation, we generated tandem mutant GRP1-PH constructs. These tandem sensors demonstrated restored membrane responsiveness and signal magnitudes comparable to those of the wild-type construct. They were successfully applied in both BRET-based assays and confocal microscopy, where the tested tandem mutant construct showed robust translocation to the plasma membrane following EGF stimulation **(Figure 13)**. Collectively, these engineered constructs expand the toolkit for investigating PIP_3 signaling with improved resolution and selectivity.

To further characterize phosphoinositide signaling under upstream conditions other than RTK stimulation, we examined cellular responses to vanadate treatment. Unlike EGF or insulin, which triggered a rapid increase followed by a plateau in PIP_3 levels, vanadate induced a slow, progressive increase in BRET signal over the entire observation window. This distinct temporal profile reflects the mechanism of action of vanadate, which involves the inhibition of phosphatases rather than activation of receptor-linked kinases. As a result, PIP_3 accumulates gradually without the sharp rise and plateau seen in the other examined signaling pathways **(Figures 12 and 13)** (95). These findings emphasize how the nature of the upstream signal can influence not only the amplitude but also the temporal dynamics of lipid signaling responses.

In earlier microscopy-based studies, we had observed that fluorescently tagged GRP1-PH biosensors frequently accumulated in both the cytosol and nucleus (61). To minimize nuclear localization in our study, a NES sequence was incorporated into the constructs (77). While this modification led to partial exclusion from the nucleus in most variants, only the single K340L mutant exhibited complete nuclear export. Surprisingly, the tandem mutant GRP1-PH constructs retained strong nuclear localization despite the presence of the NES **(Figure 13)**. This suggests that the increased molecular size or structural conformation of the tandem configuration may interfere with efficient nuclear export.

6. Conclusions

The major conclusions of our studies are as follows:

6.1. Investigation of the dynamics and regulation of PI(3,4)P_2 production in response to EGF and insulin signaling:

- We found that PI(3,4)P_2 and PIP_3 exhibit temporally and quantitatively distinct dynamics at the plasma membrane in response to EGF and insulin. EGF preferentially promoted sustained PI(3,4)P_2 accumulation relative to PIP_3, highlighting receptor-specific phosphoinositide responses.
- Our data confirmed SHIP2 as the major phosphatase responsible for PI(3,4)P_2 generation downstream of EGF, with minimal involvement following insulin stimulation. siRNA-mediated knockdown of SHIP2 reduced EGF-induced PI(3,4)P_2 accumulation, validating its enzymatic role.
- We identified that EGF-induced SHIP2 phosphorylation is calcium-dependent and mediated through PLC signaling. This post-translational modification enhances SHIP2 phosphatase activity, contributing to increased PI(3,4)P_2 levels during EGF signaling.

6.2. Optimizing PH domain-based biosensors for improved detection of plasma membrane PIP_3:

- Targeted mutations in the GRP1-PH domain significantly reduced non-specific protein-mediated membrane association, thereby enhancing lipid selectivity. However, these mutations also led to a substantial reduction in signal intensity, necessitating the development of tandem versions of the mutated constructs to restore signal strength and enable their practical application in live-cell assays. In contrast, Akt-PH mutants retained strong membrane responsiveness, indicating lower dependence on protein interactions.
- The optimized tandem GRP1-PH constructs were successfully validated in both BRET-based assays and confocal imaging. These biosensors reliably tracked PIP_3 dynamics with improved specificity and versatility across experimental platforms.

7. Summary

This study explored the regulation of phosphoinositide signaling with a focus on receptor-specific control of PIP_3 and $PI(3,4)P_2$ dynamics in mammalian cells. Using BRET-based biosensors we monitored lipid changes at the plasma membrane in response to distinct stimuli, particularly EGF and insulin. Despite activating overlapping pathways, these ligands produced divergent phosphoinositide profiles, with EGF consistently generating a higher $PI(3,4)P_2/PIP_3$ ratio. This difference was shown to be driven largely by the differential regulation of SHIP2 by the two agents.

Further analysis revealed that SHIP2 activation is regulated through stimulus-specific tyrosine phosphorylation, which was dependent on PLC-mediated calcium influx and, to a lesser extent, PI3K activity. Inhibition of SHIP2 phosphorylation via PLC blockade significantly reduced $PI(3,4)P_2$ levels, highlighting a functional role for phosphorylation in enhancing the phosphatase activity of SHIP2.

In parallel, we optimized lipid biosensors for more selective PIP_3 detection. Mutations in GRP1-PH domains that disrupted non-lipid interactions improved specificity but considerably reduced signal strength. This limitation was addressed by developing tandem mutated GRP1-PH constructs, which restored signal amplitude and demonstrated robust responsiveness to EGF stimulation in both BRET and confocal microscopy. These optimized biosensors provide a more reliable tool for monitoring the localization and dynamics of PIP_3.

Overall, this work provides new mechanistic insights into the regulation of $PI(3,4)P_2$ production, particularly via SHIP2, and delivers improved biosensors for studying PIP_3 signaling. These advances contribute to a deeper understanding of how growth factors uniquely shape phosphoinositide signaling landscapes and have potential implications for therapeutic targeting in diseases linked to dysregulated lipid metabolism.

8. References

1. Posor Y, Jang W, Haucke V. Phosphoinositides as membrane organizers. Nat Rev Mol Cell Biol. 2022;23(12):797-816.
2. Irvine RF. A short history of inositol lipids. J Lipid Res. 2016;57(11):1987-94.
3. Dickson EJ, Hille B. Understanding phosphoinositides: rare, dynamic, and essential membrane phospholipids. Biochem J. 2019;476(1):1-23.
4. Shewan A, Eastburn DJ, Mostov K. Phosphoinositides in cell architecture. Cold Spring Harb Perspect Biol. 2011;3(8):a004796.
5. De Matteis MA, Fico M, Venditti R. Regulation and function of PI4P at the Golgi complex. Biochim Biophys Acta Mol Cell Biol Lipids. 2025;1870(5):159626.
6. Batrouni AG, Baskin JM. The chemistry and biology of phosphatidylinositol 4-phosphate at the plasma membrane. Bioorg Med Chem. 2021;40:116190.
7. Itoh T, Takenawa T. Phosphoinositide-binding domains: Functional units for temporal and spatial regulation of intracellular signalling. Cell Signal. 2002;14(9):733-43.
8. Hammond GRV, Burke JE. Novel roles of phosphoinositides in signaling, lipid transport, and disease. Curr Opin Cell Biol. 2020;63:57-67.
9. Kutateladze TG. Translation of the phosphoinositide code by PI effectors. Nat Chem Biol. 2010;6(7):507-13.
10. Oh BC. Phosphoinositides and intracellular calcium signaling: novel insights into phosphoinositides and calcium coupling as negative regulators of cellular signaling. Exp Mol Med. 2023;55(8):1702-12.
11. Hou X, Chen Y, Carrillo ND, Cryns VL, Anderson RA, Sun J, Wang S, Chen M. Phosphoinositide signaling at the cytoskeleton in the regulation of cell dynamics. Cell Death Dis. 2025;16(1):296.
12. Blunsom NJ, Cockcroft S. Phosphatidylinositol synthesis at the endoplasmic reticulum. Biochim Biophys Acta Mol Cell Biol Lipids. 2020;1865(1):158471.
13. Burke JE. Structural Basis for Regulation of Phosphoinositide Kinases and Their Involvement in Human Disease. Mol Cell. 2018;71(5):653-73.
14. Lolicato F, Nickel W, Haucke V, Ebner M. Phosphoinositide switches in cell physiology - From molecular mechanisms to disease. J Biol Chem. 2024;300(3):105757.

15. Buckles TC, Ziemba BP, Masson GR, Williams RL, Falke JJ. Single-Molecule Study Reveals How Receptor and Ras Synergistically Activate PI3Kalpha and PIP(3) Signaling. Biophys J. 2017;113(11):2396-405.
16. Singh N, Reyes-Ordonez A, Compagnone MA, Moreno JF, Leslie BJ, Ha T, Chen J. Redefining the specificity of phosphoinositide-binding by human PH domain-containing proteins. Nat Commun. 2021;12(1):4339.
17. Suzuki H, Matsuda S, Terauchi Y, Fujiwara M, Ohteki T, Asano T, Behrens TW, Kouro T, Takatsu K, Kadowaki T, Koyasu S. PI3K and Btk differentially regulate B cell antigen receptor-mediated signal transduction. Nat Immunol. 2003;4(3):280-6.
18. McNamara CR, Degterev A. Small-molecule inhibitors of the PI3K signaling network. Future Med Chem. 2011;3(5):549-65.
19. Boletta A. Emerging evidence of a link between the polycystins and the mTOR pathways. Pathogenetics. 2009;2(1):6.
20. Truebestein L, Hornegger H, Anrather D, Hartl M, Fleming KD, Stariha JTB, Pardon E, Steyaert J, Burke JE, Leonard TA. Structure of autoinhibited Akt1 reveals mechanism of PIP(3)-mediated activation. Proc Natl Acad Sci U S A. 2021;118(33).
21. Sugiyama MG, Fairn GD, Antonescu CN. Akt-ing Up Just About Everywhere: Compartment-Specific Akt Activation and Function in Receptor Tyrosine Kinase Signaling. Front Cell Dev Biol. 2019;7:70.
22. Manna P, Jain SK. Phosphatidylinositol-3,4,5-triphosphate and cellular signaling: implications for obesity and diabetes. Cell Physiol Biochem. 2015;35(4):1253-75.
23. Larsen M, Hoffman MP, Sakai T, Neibaur JC, Mitchell JM, Yamada KM. Role of PI 3-kinase and PIP3 in submandibular gland branching morphogenesis. Dev Biol. 2003;255(1):178-91.
24. Hawkins PT, Stephens LR. Emerging evidence of signalling roles for PI(3,4)P2 in Class I and II PI3K-regulated pathways. Biochem Soc Trans. 2016;44(1):307-14.
25. Hasegawa J. New insights into the regulation and roles of phosphatidylinositol 3,4-bisphosphate. J Biochem. 2024;176(5):339-45.
26. Kashiwada M, Lu P, Rothman PB. PIP3 pathway in regulatory T cells and autoimmunity. Immunol Res. 2007;39(1-3):194-224.
27. Huang X, Liu G, Guo J, Su Z. The PI3K/AKT pathway in obesity and type 2 diabetes. Int J Biol Sci. 2018;14(11):1483-96.

28. Luongo F, Colonna F, Calapa F, Vitale S, Fiori ME, De Maria R. PTEN Tumor-Suppressor: The Dam of Stemness in Cancer. Cancers (Basel). 2019;11(8).
29. Denley A, Gymnopoulos M, Kang S, Mitchell C, Vogt PK. Requirement of phosphatidylinositol(3,4,5)trisphosphate in phosphatidylinositol 3-kinase-induced oncogenic transformation. Mol Cancer Res. 2009;7(7):1132-8.
30. Eramo MJ, Mitchell CA. Regulation of PtdIns(3,4,5)P3/Akt signalling by inositol polyphosphate 5-phosphatases. Biochem Soc Trans. 2016;44(1):240-52.
31. Posor Y, Eichhorn-Gruenig M, Puchkov D, Schoneberg J, Ullrich A, Lampe A, Muller R, Zarbakhsh S, Gulluni F, Hirsch E, Krauss M, Schultz C, Schmoranzer J, Noe F, Haucke V. Spatiotemporal control of endocytosis by phosphatidylinositol-3,4-bisphosphate. Nature. 2013;499(7457):233-7.
32. Wang H, Loerke D, Bruns C, Muller R, Koch PA, Puchkov D, Schultz C, Haucke V. Phosphatidylinositol 3,4-bisphosphate synthesis and turnover are spatially segregated in the endocytic pathway. J Biol Chem. 2020;295(4):1091-104.
33. Reed DE, Shokat KM. INPP4B and PTEN Loss Leads to PI-3,4-P2 Accumulation and Inhibition of PI3K in TNBC. Mol Cancer Res. 2017;15(6):765-75.
34. Ray J, Sapp DG, Fairn GD. Phosphatidylinositol 3,4-bisphosphate: Out of the shadows and into the spotlight. Curr Opin Cell Biol. 2024;88:102372.
35. Gozzelino L, De Santis MC, Gulluni F, Hirsch E, Martini M. PI(3,4)P2 Signaling in Cancer and Metabolism. Front Oncol. 2020;10:360.
36. Safaroghli-Azar A, Sanaei MJ, Pourbagheri-Sigaroodi A, Bashash D. Phosphoinositide 3-kinase (PI3K) classes: From cell signaling to endocytic recycling and autophagy. Eur J Pharmacol. 2023;953:175827.
37. Salamon RS, Backer JM. Phosphatidylinositol-3,4,5-trisphosphate: tool of choice for class I PI 3-kinases. Bioessays. 2013;35(7):602-11.
38. Kriplani N, Hermida MA, Brown ER, Leslie NR. Class I PI 3-kinases: Function and evolution. Adv Biol Regul. 2015;59:53-64.
39. Yoshioka K. Class II phosphatidylinositol 3-kinase isoforms in vesicular trafficking. Biochem Soc Trans. 2021;49(2):893-901.
40. Balla T. Phosphoinositides: tiny lipids with giant impact on cell regulation. Physiol Rev. 2013;93(3):1019-137.

41. Jean S, Kiger AA. Classes of phosphoinositide 3-kinases at a glance. J Cell Sci. 2014;127(Pt 5):923-8.
42. Zhao W, Qiu Y, Kong D. Class I phosphatidylinositol 3-kinase inhibitors for cancer therapy. Acta Pharm Sin B. 2017;7(1):27-37.
43. Muraille E, Pesesse X, Kuntz C, Erneux C. Distribution of the src-homology-2-domain-containing inositol 5-phosphatase SHIP-2 in both non-haemopoietic and haemopoietic cells and possible involvement of SHIP-2 in negative signalling of B-cells. Biochem J. 1999;342 Pt 3(Pt 3):697-705.
44. Muller SM, Jucker M. The Functional Roles of the Src Homology 2 Domain-Containing Inositol 5-Phosphatases SHIP1 and SHIP2 in the Pathogenesis of Human Diseases. Int J Mol Sci. 2024;25(10).
45. Ando K, Kucukali F, Doeraene E, Nagaraj S, Antonelli EM, Thazin Htut M, Yilmaz Z, Kosa AC, Lopez-Guitierrez L, Quintanilla-Sanchez C, Aydin E, Ramos AR, Mansour S, Turbant S, Schurmans S, Sleegers K, Erneux C, Brion JP, Leroy K, Brain Bank Neuro CEBNN. Alteration of gene expression and protein solubility of the PI 5-phosphatase SHIP2 are correlated with Alzheimer's disease pathology progression. Acta Neuropathol. 2024;147(1):94.
46. Thomas MP, Erneux C, Potter BV. SHIP2: Structure, Function and Inhibition. Chembiochem. 2017;18(3):233-47.
47. Ramos AR, Ghosh S, Erneux C. The impact of phosphoinositide 5-phosphatases on phosphoinositides in cell function and human disease. J Lipid Res. 2019;60(2):276-86.
48. Kerr WG, Pedicone C, Dormann S, Pacherille A, Chisholm JD. Small molecule targeting of SHIP1 and SHIP2. Biochem Soc Trans. 2020;48(1):291-300.
49. Petersen MC, Shulman GI. Mechanisms of Insulin Action and Insulin Resistance. Physiol Rev. 2018;98(4):2133-223.
50. Wee P, Wang Z. Epidermal Growth Factor Receptor Cell Proliferation Signaling Pathways. Cancers (Basel). 2017;9(5).
51. Delos Santos RC, Bautista S, Lucarelli S, Bone LN, Dayam RM, Abousawan J, Botelho RJ, Antonescu CN. Selective regulation of clathrin-mediated epidermal growth factor receptor signaling and endocytosis by phospholipase C and calcium. Mol Biol Cell. 2017;28(21):2802-18.

52. Klip A, Sun Y, Chiu TT, Foley KP. Signal transduction meets vesicle traffic: the software and hardware of GLUT4 translocation. Am J Physiol Cell Physiol. 2014;306(10):C879-86.

53. Lemmon MA. Pleckstrin homology (PH) domains and phosphoinositides. Biochem Soc Symp. 2007(74):81-93.

54. Ingley E, Hemmings BA. Pleckstrin homology (PH) domains in signal transduction. J Cell Biochem. 1994;56(4):436-43.

55. Idevall-Hagren O, De Camilli P. Detection and manipulation of phosphoinositides. Biochim Biophys Acta. 2015;1851(6):736-45.

56. Godi A, Di Campli A, Konstantakopoulos A, Di Tullio G, Alessi DR, Kular GS, Daniele T, Marra P, Lucocq JM, De Matteis MA. FAPPs control Golgi-to-cell-surface membrane traffic by binding to ARF and PtdIns(4)P. Nat Cell Biol. 2004;6(5):393-404.

57. Liu Y, Kahn RA, Prestegard JH. Interaction of Fapp1 with Arf1 and PI4P at a membrane surface: an example of coincidence detection. Structure. 2014;22(3):421-30.

58. Bethoney KA, King MC, Hinshaw JE, Ostap EM, Lemmon MA. A possible effector role for the pleckstrin homology (PH) domain of dynamin. Proc Natl Acad Sci U S A. 2009;106(32):13359-64.

59. Szaszak M, Gaborik Z, Turu G, McPherson PS, Clark AJ, Catt KJ, Hunyady L. Role of the proline-rich domain of dynamin-2 and its interactions with Src homology 3 domains during endocytosis of the AT1 angiotensin receptor. J Biol Chem. 2002;277(24):21650-6.

60. Yu JW, Mendrola JM, Audhya A, Singh S, Keleti D, DeWald DB, Murray D, Emr SD, Lemmon MA. Genome-wide analysis of membrane targeting by S. cerevisiae pleckstrin homology domains. Mol Cell. 2004;13(5):677-88.

61. Varnai P, Bondeva T, Tamas P, Toth B, Buday L, Hunyady L, Balla T. Selective cellular effects of overexpressed pleckstrin-homology domains that recognize PtdIns(3,4,5)P3 suggest their interaction with protein binding partners. J Cell Sci. 2005;118(Pt 20):4879-88.

62. Jackson TR, Kearns BG, Theibert AB. Cytohesins and centaurins: mediators of PI 3-kinase-regulated Arf signaling. Trends Biochem Sci. 2000;25(10):489-95.

63. Malaby AW, van den Berg B, Lambright DG. Structural basis for membrane recruitment and allosteric activation of cytohesin family Arf GTPase exchange factors. Proc Natl Acad Sci U S A. 2013;110(35):14213-8.

64. Corbin JA, Dirkx RA, Falke JJ. GRP1 pleckstrin homology domain: activation parameters and novel search mechanism for rare target lipid. Biochemistry. 2004;43(51):16161-73.

65. He J, Haney RM, Vora M, Verkhusha VV, Stahelin RV, Kutateladze TG. Molecular mechanism of membrane targeting by the GRP1 PH domain. J Lipid Res. 2008;49(8):1807-15.

66. Lai CL, Srivastava A, Pilling C, Chase AR, Falke JJ, Voth GA. Molecular mechanism of membrane binding of the GRP1 PH domain. J Mol Biol. 2013;425(17):3073-90.

67. Varnai P, Gulyas G, Toth DJ, Sohn M, Sengupta N, Balla T. Quantifying lipid changes in various membrane compartments using lipid binding protein domains. Cell Calcium. 2017;64:72-82.

68. Varnai P, Balla T. Live cell imaging of phosphoinositide dynamics with fluorescent protein domains. Biochim Biophys Acta. 2006;1761(8):957-67.

69. Cohen LA, Honda A, Varnai P, Brown FD, Balla T, Donaldson JG. Active Arf6 recruits ARNO/cytohesin GEFs to the PM by binding their PH domains. Mol Biol Cell. 2007;18(6):2244-53.

70. Basu A, Lambring CB. Akt Isoforms: A Family Affair in Breast Cancer. Cancers (Basel). 2021;13(14).

71. Yung HW, Charnock-Jones DS, Burton GJ. Regulation of AKT phosphorylation at Ser473 and Thr308 by endoplasmic reticulum stress modulates substrate specificity in a severity dependent manner. PLoS One. 2011;6(3):e17894.

72. Yudushkin I. Control of Akt activity and substrate phosphorylation in cells. IUBMB Life. 2020;72(6):1115-25.

73. Liu SL, Wang ZG, Hu Y, Xin Y, Singaram I, Gorai S, Zhou X, Shim Y, Min JH, Gong LW, Hay N, Zhang J, Cho W. Quantitative Lipid Imaging Reveals a New Signaling Function of Phosphatidylinositol-3,4-Bisphophate: Isoform- and Site-Specific Activation of Akt. Mol Cell. 2018;71(6):1092-104 e5.

74. Huang BX, Akbar M, Kevala K, Kim HY. Phosphatidylserine is a critical modulator for Akt activation. J Cell Biol. 2011;192(6):979-92.

75. Hunyady L, Baukal AJ, Gaborik Z, Olivares-Reyes JA, Bor M, Szaszak M, Lodge R, Catt KJ, Balla T. Differential PI 3-kinase dependence of early and late phases of recycling of the internalized AT1 angiotensin receptor. J Cell Biol. 2002;157(7):1211-22.

76. Toth JT, Gulyas G, Hunyady L, Varnai P. Development of Nonspecific BRET-Based Biosensors to Monitor Plasma Membrane Inositol Lipids in Living Cells. Methods Mol Biol. 2019;1949:23-34.

77. Damouni A, Toth DJ, Barsi S, Nagy DK, Kasbary A, Hunyady L, Cserzo M, Varnai P. Differential activation of the inositol 5-phosphatase SHIP2 by EGF and insulin signaling pathways. J Biol Chem. 2025;301(7):110275.

78. Goulden BD, Pacheco J, Dull A, Zewe JP, Deiters A, Hammond GRV. A high-avidity biosensor reveals plasma membrane PI(3,4)P(2) is predominantly a class I PI3K signaling product. J Cell Biol. 2019;218(3):1066-79.

79. Prasad NK, Werner ME, Decker SJ. Specific tyrosine phosphorylations mediate signal-dependent stimulation of SHIP2 inositol phosphatase activity, while the SH2 domain confers an inhibitory effect to maintain the basal activity. Biochemistry. 2009;48(27):6285-7.

80. Sampaio C, Dance M, Montagner A, Edouard T, Malet N, Perret B, Yart A, Salles JP, Raynal P. Signal strength dictates phosphoinositide 3-kinase contribution to Ras/extracellular signal-regulated kinase 1 and 2 activation via differential Gab1/Shp2 recruitment: consequences for resistance to epidermal growth factor receptor inhibition. Mol Cell Biol. 2008;28(2):587-600.

81. Uchida T. Stimulation of phospholipid synthesis in HeLa cells by epidermal growth factor and insulin: activation of choline kinase and glycerophosphate acyltransferase. Biochim Biophys Acta. 1996;1304(2):89-104.

82. Kamentseva RS, Kharchenko MV, Gabdrahmanova GV, Kotov MA, Kosheverova VV, Kornilova ES. EGF, TGF-alpha and Amphiregulin Differently Regulate Endometrium-Derived Mesenchymal Stromal/Stem Cells. Int J Mol Sci. 2023;24(17).

83. Martinez Baez A, Castro Romero I, Chihu Amparan L, Castaneda JR, Ayala G. The Insulin Receptor Substrate 2 Mediates the Action of Insulin on HeLa Cell Migration via the PI3K/Akt Signaling Pathway. Curr Issues Mol Biol. 2023;45(3):2296-308.

84. Gulyas G, Toth JT, Toth DJ, Kurucz I, Hunyady L, Balla T, Varnai P. Measurement of inositol 1,4,5-trisphosphate in living cells using an improved set of resonance energy transfer-based biosensors. PLoS One. 2015;10(5):e0125601.

85. Damouni A, Toth DJ, Schonek A, Kasbary A, Boros AP, Varnai P. Optimizing PH Domain-Based Biosensors for Improved Plasma Membrane PIP(3) Measurements in Mammalian Cells. Cells. 2025;14(14).

86. Molinari P, Casella I, Costa T. Functional complementation of high-efficiency resonance energy transfer: a new tool for the study of protein binding interactions in living cells. Biochem J. 2008;409(1):251-61.

87. Chung JK, Nocka LM, Decker A, Wang Q, Kadlecek TA, Weiss A, Kuriyan J, Groves JT. Switch-like activation of Bruton's tyrosine kinase by membrane-mediated dimerization. Proc Natl Acad Sci U S A. 2019;116(22):10798-803.

88. Elong Edimo W, Derua R, Janssens V, Nakamura T, Vanderwinden JM, Waelkens E, Erneux C. Evidence of SHIP2 Ser132 phosphorylation, its nuclear localization and stability. Biochem J. 2011;439(3):391-401.

89. Phee H, Jacob A, Coggeshall KM. Enzymatic activity of the Src homology 2 domain-containing inositol phosphatase is regulated by a plasma membrane location. J Biol Chem. 2000;275(25):19090-7.

90. Gulyas G, Sohn M, Kim YJ, Varnai P, Balla T. ORP3 phosphorylation regulates phosphatidylinositol 4-phosphate and Ca(2+) dynamics at plasma membrane-ER contact sites. J Cell Sci. 2020;133(6).

91. Huang W, Barrett M, Hajicek N, Hicks S, Harden TK, Sondek J, Zhang Q. Small molecule inhibitors of phospholipase C from a novel high-throughput screen. J Biol Chem. 2013;288(8):5840-8.

92. Scott SA, Mathews TP, Ivanova PT, Lindsley CW, Brown HA. Chemical modulation of glycerolipid signaling and metabolic pathways. Biochim Biophys Acta. 2014;1841(8):1060-84.

93. Compeer MG, Janssen GM, De Mey JG. Endothelin-1 and endothelin-2 initiate and maintain contractile responses by different mechanisms in rat mesenteric and cerebral arteries. Br J Pharmacol. 2013;170(6):1199-209.
94. Bill CA, Vines CM. Phospholipase C. Adv Exp Med Biol. 2020;1131:215-42.
95. Batty IH, van der Kaay J, Gray A, Telfer JF, Dixon MJ, Downes CP. The control of phosphatidylinositol 3,4-bisphosphate concentrations by activation of the Src homology 2 domain containing inositol polyphosphate 5-phosphatase 2, SHIP2. Biochem J. 2007;407(2):255-66.

9. Bibliography of the candidate's publications

9.1. Publications relevant to the dissertation

I. Damouni , Amir; Tóth, Dániel J; , Barsi, Szilvia; Nagy, Dániel Károly; Kasbary, Alexander; Hunyady, László; Cserző, Miklós; Várnai, Péter. Differential activation of the inositol 5-phosphatase SHIP2 by EGF and insulin signaling pathways. Journal of Biological Chemistry, 2025, 301(7), 110275. **IF(2024): 3.9**

II. Damouni, Amir; Tóth, Dániel J.; Schönek, Aletta; Kasbary, Alexander; Boros, Adél P.; Várnai, Péter. Optimizing PH Domain-Based Biosensors for Improved Plasma Membrane PIP3 Measurements in Mammalian Cells. Cells, 2025, 14(14), 1125. **IF(2024): 5.2**

Cumulative impact factor: 9.1

9.2. Publications unrelated to the dissertation

I. Tóth, Dániel J.; Tóth, József T.; Damouni, Amir; Hunyady, László; Várnai, Péter; Effect of hormone-induced plasma membrane phosphatidylinositol 4,5-bisphosphate depletion on receptor endocytosis suggests the importance of local regulation in phosphoinositide signaling. Scientific Reports, 2024, 14, Article 291. **IF (2024): 3.9**

II. Gém, Janka Borbála; Kovács, Kinga Bernadett; Barsi, Szilvia; Hadadnejadtehrani, Sahar; Damouni, Amir; Turu, Gábor; Tóth, András Dávid; Várnai, Péter; Hunyady, László; Balla, András. Role of LMCD1 in the Long-Term Effects of Angiotensin II in Vascular Smooth Muscle Cells. International Journal of Molecular Sciences, 2025, 26(9), 4053. **IF(2024): 4.9**

Cumulative impact factor of all publications: 17.9

Cumulative impact factor of first author publications: 9.1

10. Acknowledgements

Completing this thesis has been a transformative journey that goes far beyond the acquisition of academic knowledge. It represents years of scientific exploration, critical thinking, and personal growth, and stands as a testament to the value of perseverance, curiosity, and collaboration in research. Through this process, I have come to appreciate that even the most complex challenges can be navigated with the right mentorship and the support of those around me. I am deeply grateful to everyone who has guided, inspired, and encouraged me along the way, and I look forward to carrying these experiences into my future contributions to science and medicine.

I would like to express my deepest gratitude to my supervisor, Prof. Dr. Péter Várnai, for his unwavering support, generous guidance, and constant encouragement throughout my PhD journey. His door was always open, whether for scientific advice, thoughtful discussions, or simply a few words of motivation. Beyond being an exceptional mentor, I am honored to call him a friend. I am also immensely thankful to Dr. Dániel Tóth, whose steady guidance and kindness were invaluable to me during the most critical phases of my research and publication efforts. His patience, expertise, and willingness to share his knowledge made a profound impact on my growth as a scientist. Finally, I extend my heartfelt thanks to the entire Department of Physiology at Semmelweis University for providing a nurturing and inspiring environment in which I was able to carry out my postgraduate work.

With all my heart, I would like to thank my family for their love, support, and guidance, not only throughout my PhD studies, but across every step of my medical and academic journey. To my beloved grandmother Aida, my parents Ibrahim and Nadera, and my dear brothers Tamer and Bassel, your belief in me has been my anchor, and nothing I have achieved would have been possible without your constant presence and encouragement. A special and heartfelt thank you goes to my wonderful partner, Leandra, who has patiently endured more conversations about phosphoinositides than any reasonable person ever should. Her strength, warmth, and unwavering support through the grueling manuscript reviews, every long experimental day, and every small victory have made this journey not only possible, but meaningful.

JBC RESEARCH ARTICLE

Differential activation of the inositol 5-phosphatase SHIP2 by EGF and insulin signaling pathways

Received for publication, November 28, 2024, and in revised form, May 8, 2025 Published, Papers in Press, May 22, 2025,
https://doi.org/10.1016/j.jbc.2025.110275

Amir Damouni[1], Dániel J. Tóth[1,2], Szilvia Barsi[1], Dániel Károly Nagy[1], Alexander Kasbary[1], László Hunyady[1], Miklós Cserző[2], and Péter Várnai[1,2,*]

From the [1]Department of Physiology, Faculty of Medicine, Semmelweis University, Budapest, Hungary; [2]HUN-REN–SU Molecular Physiology Research Group, Hungarian Research Network and Semmelweis University, Budapest, Hungary

Reviewed by members of the JBC Editorial Board. Edited by Kirill Martemyanov

The importance of phosphatidylinositol 3,4,5- trisphosphate (PIP_3) in cell signaling has been well established. Despite phosphatidylinositol 3,4-bisphosphate [$PI(3,4)P_2$] emerging as an actor independent of PIP_3, its exact signaling role remains poorly understood, and the precise dynamics of $PI(3,4)P_2$ and PIP_3 upon receptor tyrosine kinase (RTK) stimulation are still inadequately investigated. In this study, we employed bioluminescence resonance energy transfer (BRET) sensors to monitor plasma membrane phosphoinositide (PIP) dynamics in HEK293-derived and HeLa cells following stimulation with epidermal growth factor (EGF) and insulin. Our findings reveal significant differences in PIP regulation: The increase in $PI(3,4)P_2$ compared to PIP_3 was larger with EGF stimulation relative to insulin. Using siRNA-mediated knockdown, we identified SH2-domain containing inositol polyphosphate 5-phosphatase 2 (SHIP2) as the key enzyme responsible for $PI(3,4)P_2$ production in the EGF pathway, which was further supported by a bioinformatics analysis. Moreover, we detected increased phosphorylation at two tyrosine sites in SHIP2 upon EGF stimulation, which was shown to be dependent on PI3K activation and PLC-induced calcium signal. These findings help refine our understanding of receptor-specific phosphoinositide dynamics and the enzymatic machinery involved, as well as their potential influence on downstream cellular responses.

Phosphoinositides (PIPs) are a class of specialized phospholipids that exist in dynamic pools, undergoing rapid interconversion by various enzymes (1). Despite their low abundance, these molecules are vital regulators of numerous essential cellular processes, primarily through their interactions with effector proteins that contain specific lipid-binding domains (2). There are seven distinct types of PIPs, each characterized by unique phosphorylation patterns on the 3-, 4-, and 5- hydroxyl groups of the inositol ring. PIPs are distributed across different intracellular membranes, where they are key to defining membrane identity (3). Furthermore, they act as crucial second messengers, with those localized to the plasma membrane (PM) playing a particularly central role in signal transduction (1). Moreover, dysregulation of PIP metabolism has been implicated in a range of pathologies, including cancer and metabolic disorders (4, 5).

Phosphatidylinositol 3,4,5-trisphosphate (PIP_3) has long been recognized as a crucial signaling molecule, particularly in receptor tyrosine kinase (RTK) signaling cascades. Activation of RTKs triggers the phosphorylation of phosphatidylinositol 4,5-bisphosphate [$PI(4,5)P_2$] at the 3-position by class I phosphatidylinositol 3-kinases (PI3Ks), leading to generation of PIP_3 at the PM (6). PIP_3 then acts as a critical signaling lipid, recruiting and activating various effector proteins, including protein kinase B (PKB or Akt), a serine/threonine kinase essential for regulating cell survival, growth, and proliferation (7, 8). Additionally, PIP_3 is involved in a wide range of other cellular processes, such as exocytosis, cytoskeletal remodeling, apoptosis, and metabolism (9).

Once formed, PIP_3 can be either dephosphorylated back to $PI(4,5)P_2$ by the 3-phosphatase PTEN or converted into phosphatidylinositol 3,4-bisphosphate [$PI(3,4)P_2$] by 5-phosphatases, such as SH2-domain-containing inositol polyphosphate 5-phosphatase (SHIP) enzymes (10, 11). Previously regarded as merely a degradation product of PIP_3, $PI(3,4)P_2$ has recently gained recognition as an active signaling molecule with functions that are, at least partially, independent of PIP_3 (12). Studies have revealed that $PI(3,4)P_2$ plays crucial roles in regulating cytoskeletal organization, cell polarization, and migration (13). Additionally, $PI(3,4)P_2$ can also be synthesized directly from phosphatidylinositol 4-phosphate (PI4P) *via* the catalytic action of class II PI3Ks (PI3KC2), a pathway that is pivotal for endocytosis (14, 15).

As $PI(3,4)P_2$ emerges as a distinct and important signaling molecule, understanding the enzymes that regulate its synthesis and turnover becomes increasingly critical. Central to this regulation are the SHIP enzymes, which play a key role in modulating $PI(3,4)P_2$ levels at the PM. Two major isoforms of SHIP exist: SHIP1, predominantly found in hematopoietic cells, and SHIP2, which is more widely expressed across various tissues (16, 17). SHIP enzymes have been linked to various diseases, such as Alzheimer's disease and metabolic disorders (18, 19). The role of SHIP enzymes in cancer is complex and remains a topic of debate (20). On the one hand, by reducing PIP_3 levels, SHIP enzymes can act as tumor suppressors. However, their product, $PI(3,4)P_2$, can also

* For correspondence: Péter Várnai, varnai.peter@semmelweis.hu.

activate Akt isoforms, raising the possibility of oncogenic functions as well (17). Consequently, SHIP enzymes have become targets of interest in cancer research, with ongoing studies exploring their suppression as a potential therapeutic strategy (21).

Epidermal growth factor receptor (EGFR) and insulin receptor (IR) both belong to the RTK family and share many similar features and downstream signaling pathways, including activation of PI3Ks, consequent elevation of PIP_3 levels, and recruitment and activation of the Akt kinase. However, there are also substantial differences in their signaling patterns: They use a different set of adaptor proteins for PI3K and Akt activation and activate divergent downstream pathways (22, 23). As an example, EGFR stimulation involves activation of phospholipase C-gamma (PLCγ), which in turn generates a calcium signal and activates protein kinase C isoforms (22, 24), whereas IR stimulation can lead to activation of Rho and Rab family GTPases to promote glucose uptake in skeletal muscle (23, 25). $PI(3,4)P_2$ has been implicated in the signaling network of both EGFR and IR, but its relative contribution and the details of its regulation are still not entirely understood.

In this study, we investigated the dynamics, effects, and mechanisms of PM PIP levels after stimulation of EGFR and IR in both HEK293-derived and HeLa cells. Leveraging a sensitive bioluminescence resonance energy transfer (BRET)-based method and utilizing various PIP biosensors, we were able to demonstrate a distinctive pattern of changes in PIP_3 and $PI(3,4)P_2$ levels depending on the activated receptor. With knockdown experiments, we confirmed the central role of the SHIP2 enzyme in orchestrating the phosphoinositide cellular response to EGF stimulation. We also demonstrated that SHIP2 undergoes PI3K- and PLC-dependent phosphorylation in EGFR signaling, while remaining unaffected in the context of insulin stimulation.

Results

Monitoring plasma membrane phosphoinositide levels with BRET-based biosensors

As many of the effects of PIPs are mediated by the recruitment of soluble proteins to the membrane *via* specific PI- recognizing domains, such as the pleckstrin homology (PH) domain, we leveraged this mechanism to monitor PM phosphoinositide changes by fusing specific PH domains to fluorescent proteins to follow their localization. For this, we used lipid-binding domains that have been recognized and extensively employed in the field. To follow changes in PIP_3, we used two distinct peptide domains: the PH domain from the GRP1 protein and the PH domain of Bruton's tyrosine kinase (Btk), while for $PI(3,4)P_2$ we used the PH domain of the TAPP1 protein in tandem (TAPP1-2xPH).

First, we assessed the intracellular localization of our lipid-binding PH domains with confocal microscopy in HEK293-AT1 cells, a HEK293-derived line stably expressing the type-1A rat angiotensin II receptor. These cells were transfected to express either the yellow fluorescent protein Venus directed to the cell membrane using the targeting sequence of Lck (L10), or the lipid-binding domains, also tagged with Venus. Since production of PIP_3 and its derivatives is known to be dependent on serum-derived factors, we captured images of native cells (control) and compared them to images captured following 5 h of serum deprivation. As expected, membrane-targeted Venus was confined to the PM. However, the biosensors exhibited varied intracellular localization. Specifically, in control cells kept in serum-containing medium, Btk-PH was localized in the cytosol, whereas GRP1-PH exhibited a clear association with the PM. TAPP1-2xPH also associated with the membrane, although less distinctly (Fig. 1*A*, upper images). In contrast, following 5-h serum starvation, the membrane association of GRP1-PH, although still present, was noticeably diminished. Concurrently, both Btk-PH and TAPP1-2xPH were restricted to the cytosol, with no evident membrane association (Fig. 1*A*, lower images).

Given the higher sensitivity of BRET for observing PIP dynamics, we adapted our confocal microscopy sensors into BRET sensors to monitor PIP levels upon receptor stimulation. To achieve this, we fused the lipid-binding domains to the BRET donor molecule, luciferase. Concurrently, to specifically monitor PIP levels at the PM we anchored the BRET acceptor, Venus, to the cell membrane using the above-mentioned targeting sequence (Fig. 1*B*). This setup allows for direct monitoring of PIP levels at the PM as shifts in PIP concentrations result in altered recruitment of the lipid-binding domains, thereby modulating the BRET signal. A more precise description of the method was published recently (26, 27).

To compare our BRET-based biosensors, we calculated the basal BRET ratio (in the absence of stimuli) of the three sensors, which correlates with the resting PM localization of the lipid-binding domains, in native (control) and 5-h serum starved cells. Consistent with the confocal images, the basal BRET ratio in the control cells was markedly higher for GRP1-PH compared to the Btk-PH and TAPP1-2xPH sensors. Notably, 5-hour-long serum starvation resulted in decreased basal BRET ratios for GRP1-PH and TAPP1-2xPH when compared to their respective control states (Fig. 1*C*). Taken together, these findings highlight the distinct intracellular localization and cellular dynamics of the two PIP_3 biosensors, Btk-PH and GRP1-PH. These differences prompted us to use both biosensors during our experiments, which allows for a more comprehensive assessment of fluctuations in PIP_3 levels.

Comparison of EGF and insulin effects on PIP levels in HEK293-AT1 cells

We employed our BRET-based biosensors described earlier to quantify alterations in PM PIP levels in response to different stimuli, using HEK293-AT1 cells. Tyrosine kinase receptors are known to activate PI3K and generate PIP_3 and also $PI(3,4)P_2$, so we decided to first test the effects of EGF stimulation on these lipids. HEK293-AT1 cells were transfected with the above-mentioned biosensors, and to overcome the variability associated with endogenous EGFR expression in HEK293-derived cell lines, cells were also transfected with EGFR.

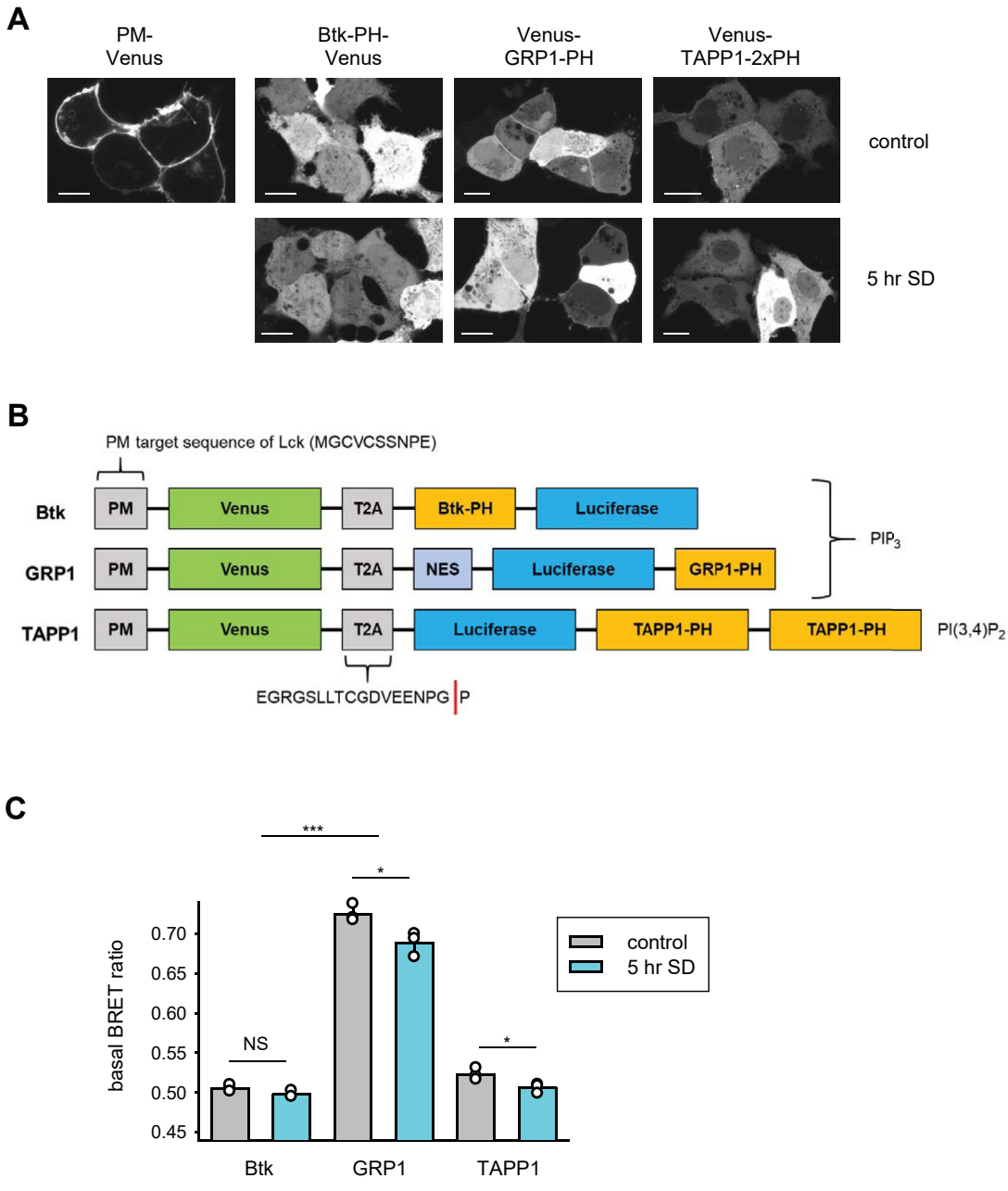

Figure 1. Biosensors for plasma membrane phosphoinositide detection. *A*, representative confocal images of native (control) or 5 h serum-starved HEK293-AT1 cells expressing plasma membrane targeted Venus or the indicated lipid-binding domains tagged with Venus. Scale bar: 10 μm. *B*, schematic representations of domain structures of the phosphoinositide BRET-based biosensors used in this study. PM represents the plasma membrane target sequence of Lck, while T2A is a viral protein sequence. The sequence is transcribed as a single mRNA molecule, but translation is interrupted between the two amino acids indicated by the *red line*, resulting in two separate polypeptide chains. *C*, the bar graph shows the basal BRET ratios of the indicated sensors measured in native cells or after 5 h of serum deprivation. Data are the mean ± SD of 3 independent experiments. Statistical significance was tested with two-way ANOVA and Holm-Sidak *post hoc* test, with only the comparisons of interest indicated. NS: $p > 0.05$, *$p < 0.05$, ***$p < 0.001$ between the Btk-PH group and GRP1-PH group. NES, nuclear export signal; SD, serum deprivation.

28 h after transfection, we applied 100 ng/ml EGF stimulation to serum-starved HEK293-AT1 cells and subsequently calculated changes in the BRET ratio, which represents the lipid-dependent membrane binding of the PH domains of the sensors. An increase in the signal of a particular sensor upon stimulation represents an elevation in the corresponding PIP level at the PM. EGF stimulation resulted in a slight increase in PIP_3 levels measured with both sensors, coupled with a pronounced rise in $PI(3,4)P_2$ levels (Fig. 2*A*, blue curves). Since the changes for both PIP_3 sensors were surprisingly low, we chose to confirm their lipid binding affinity by comparing the PIP profile of EGF stimulation to that of another tyrosine kinase receptor, the insulin receptor. We treated the cells with an insulin concentration that elicited a $PI(3,4)P_2$ response comparable to that of EGF, which was determined to be 70 nM. In contrast to the EGF response, insulin stimulation led to a substantial increase in both PIP_3 and $PI(3,4)P_2$ levels (Fig. 2*A*, red curves).

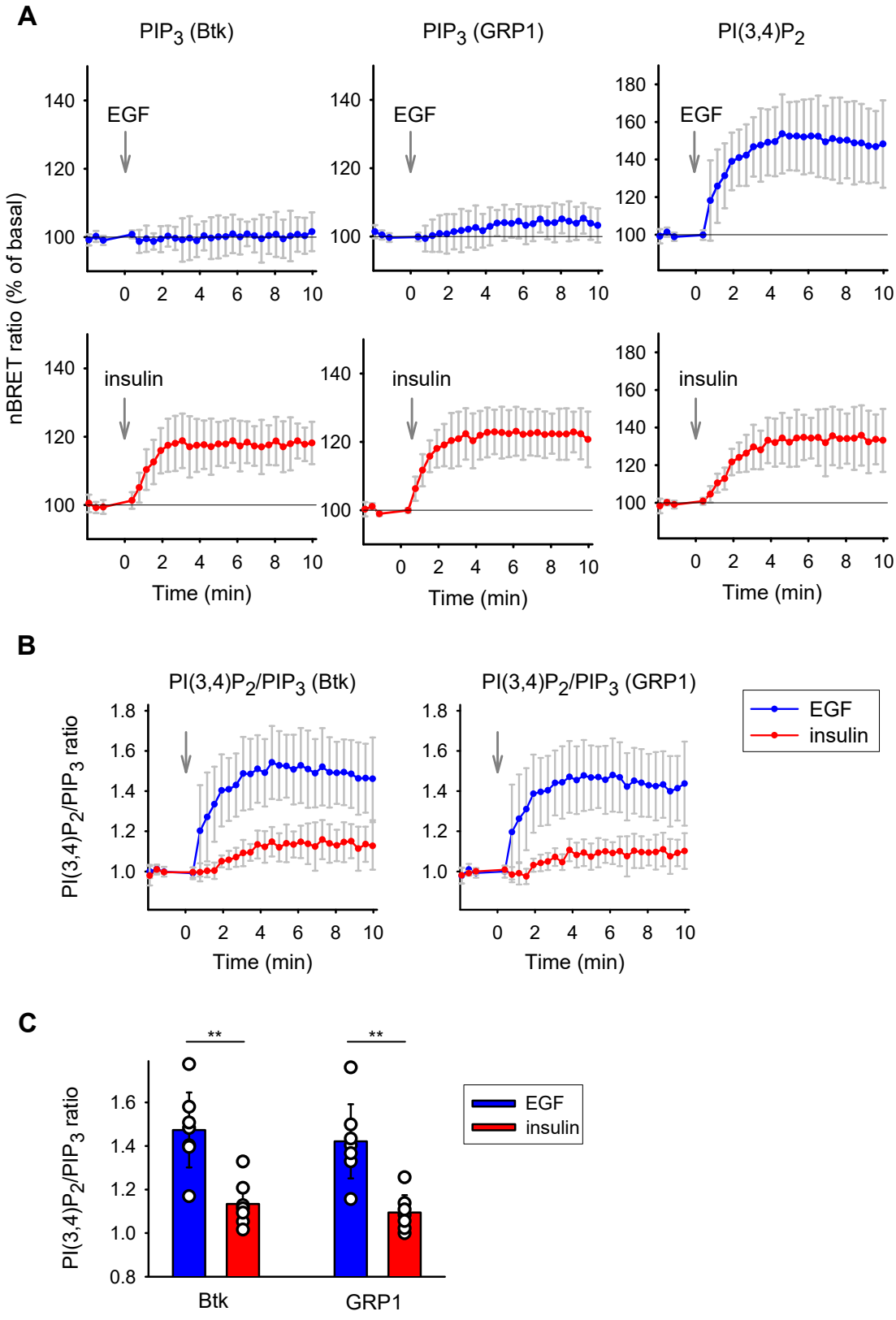

Figure 2. Comparison of EGF and insulin effects on plasma membrane PIP_3 and $PI(3,4)P_2$ levels in HEK293-AT1 cells. *A*, the levels of PIP_3 and $PI(3,4)P_2$ were measured with BRET in HEK293-AT1 cells. Cells were transiently transfected with CMV EGFR construct, as well as Btk-PH or GRP1-PH sensors to measure PIP_3, or TAPP1-2xPH sensor to measure $PI(3,4)P_2$. 28 h after transfection, serum-starved cells (5 h) were treated with EGF (100 ng/ml, *blue curves*) or insulin (70 nM, *red* curves) at time point indicated by the *arrows*, and the BRET ratio was calculated as described in Methods. BRET ratio values were normalized for the baselines (100%) for each curve. Data are the mean ± SD of 7 independent experiments, each performed in duplicate. *B*, for better comparison of EGF and insulin effects on PIP_3 and $PI(3,4)P_2$ levels, the $PI(3,4)P_2/PIP_3$ ratios were calculated, using either the Btk- or GRP1-based PIP_3 signal, and the

For better visualization of this different pattern, we calculated the $PI(3,4)P_2/PIP_3$ ratio under each stimulus condition. Ratios were calculated using the TAPP1-based sensor response for $PI(3,4)P_2$, and either the Btk- or GRP1-based signal for PIP_3. These ratios were significantly higher with EGF compared to insulin stimulation (Fig. 2, *B* and *C*), suggesting distinct cellular responses to these two stimuli in terms of phosphatidylinositol signaling.

Comparison of EGF and insulin effects on PIP levels in HEK293A cells

Building on our findings from the specialized HEK293-AT1 cells, we sought to extend the validity of our results by performing parallel experiments on a more ubiquitously utilized cell line, HEK293A. In this new set of experiments, we introduced a novel BRET PIP_3 biosensor, Btk-2xPH, a tandem version of the previously employed Btk-PH sensor, to overcome the lower affinity of the Btk-PH sensor compared to GRP1-PH, reflected by its significantly lower basal BRET ratio (Fig. 1*C*). Confocal microscopy experiments investigating the biosensor localization revealed a lack of PM association under serum-starved conditions. However, upon 70 nM insulin stimulation, a pronounced association with the PM was observed (Fig. 3*A*). We also checked the basal BRET ratios for each sensor in HEK293A cells under serum-starved conditions (Fig. 3*B*) which proved to be slightly different from those measured in the previous cell line (Fig. 1*C*).

In addition to EGF and the original insulin concentration, we also explored the effects of a tenfold increase in insulin concentration. Initially, we transfected HEK293A cells with EGFR and our specific biosensors targeting $PI(3,4)P_2$ and PIP_3, using all three PIP_3 sensors mentioned. After 28 h, serum-starved cells were stimulated with 100 ng/ml EGF or the two insulin concentrations (70 nM and 0.7 μM), and BRET ratio variations were calculated. Here, EGF and the original insulin concentration induced a similar increase in PIP_3, but a more significant elevation in $PI(3,4)P_2$ levels was observed with EGF (blue and red curves on Fig. 3*C*, respectively). Notably, the higher insulin concentration caused a more substantial increase in both $PI(3,4)P_2$ and PIP_3 levels compared to the previously used concentration (green and red curves on Fig. 3*C*, respectively). Response to all three stimuli were substantially higher for the tandem version of the Btk sensor compared to the original version, indicating a higher affinity for PIP_3. Taken together, these findings demonstrate that the Btk-2xPH biosensor can recognize PIP_3 in the PM with sufficiently high affinity, rendering it an additional tool for measuring its fluctuations.

Analysis of the $PI(3,4)P_2/PIP_3$ ratios demonstrated that, similar to HEK293-AT1 cells, EGF yielded a higher ratio than insulin regardless of the PIP_3 sensor used in the ratio calculation (Fig. 3*D*). Notably, the ratios were consistent across both insulin concentrations (green and red curves on Fig. 3*D*). We also tested these ratio changes statistically and found that EGF stimulation was significantly different from both insulin concentrations, but there was no difference between high and low insulin (Fig. 3*E*). Next, as our earliest post-stimulation time point was already near the plateau, we examined $PI(3,4)P_2/PIP_3$ ratio dynamics at the highest temporal resolution achievable with our setup (every 2 s), using the tandem Btk-PH sensor. This revealed a transient decrease in the ratio immediately following EGF stimulation, followed by a rise to its elevated level (Fig. 3*F*).

Surprisingly, despite the extensive similarities between the two cell lines, the absolute values of the ratios were different in the HEK293-AT1 and HEK293A cells. Specifically, the ratios in the HEK293A cells, calculated using the GRP1-PH sensor measurements (Fig. 3, *B* and *E*), were lower than those in HEK293-AT1 cells (Fig. 2, *B* and *C*), while maintaining the relative differences between EGF and insulin stimulation.

The effect of siRNA-mediated SHIP2 knockdown on EGF-induced plasma membrane PIP level changes

As EGF elicited a pronounced increase in PM $PI(3,4)P_2$ in both HEK cell lines, we next aimed to investigate the underlying mechanism responsible for this increase. There are two primary pathways through which $PI(3,4)P_2$ can be synthesized: either through the 5-phosphatase activity of SHIP2 enzyme which transforms PIP_3, produced by class I PI3Ks, into $PI(3,4)P_2$, or *via* the direct phosphorylation of PI4P by class II PI3Ks (Fig. 4*A*). Nevertheless, the consensus is that the predominant source of $PI(3,4)P_2$ is PIP_3 (28). To validate this consensus in our model, we employed siRNA-mediated knockdown of SHIP2 and class II PI3Ks. HEK293-AT1 cells were first transfected with the indicated siRNAs, 48 h later with EGFR and the GRP1-PH or TAPP1-2xPH sensors. 28 h later, serum-starved cells were stimulated with EGF and BRET ratios were calculated. With SHIP2 knockdown, we observed a slight increase in PIP_3 levels accompanied by a pronounced reduction in $PI(3,4)P_2$ levels compared to control (Fig. 4*B*, orange and black curves, respectively). Contrarily, knockdown of class II PI3Ks considerably amplified the EGF-induced $PI(3,4)P_2$ levels (Fig. 4*B*, green curves). Consequently, the $PI(3,4)P_2/PIP_3$ ratio upon EGF stimulation was decreased with SHIP2 knockdown and increased with class II PI3K knockdown when compared to control (Fig. 4*C*).

Similarly, the EGF-induced response was also tested in HEK293 A cells, targeting only SHIP2 as it effectively reduced $PI(3,4)P_2$ levels in the other cell line. Consistent with previous results, siRNA-mediated SHIP2 knockdown mildly elevated PIP_3 levels upon EGF stimulation while simultaneously substantially attenuating the rise in $PI(3,4)P_2$ (Fig. 4*D*), thereby significantly reducing the $PI(3,4)P_2/PIP_3$ ratio when compared to control (Fig. 4*E*). These findings suggest that mainly SHIP2 activity is responsible for the observed $PI(3,4)P_2$ surge upon EGF stimulation in both investigated cell lines. In contrast,

TAPP1-based sensor response for $PI(3,4)P_2$ in both cases. *C*, the bar graph shows the $PI(3,4)P_2/PIP_3$ ratio with each stimulus. Data are means ± SD of the last 5 measurement points of the curves from *panel B*. EGF- and insulin-induced changes were compared with an unpaired, two-tailed *t* test for each sensor separately. $^{**}p < 0.01$.

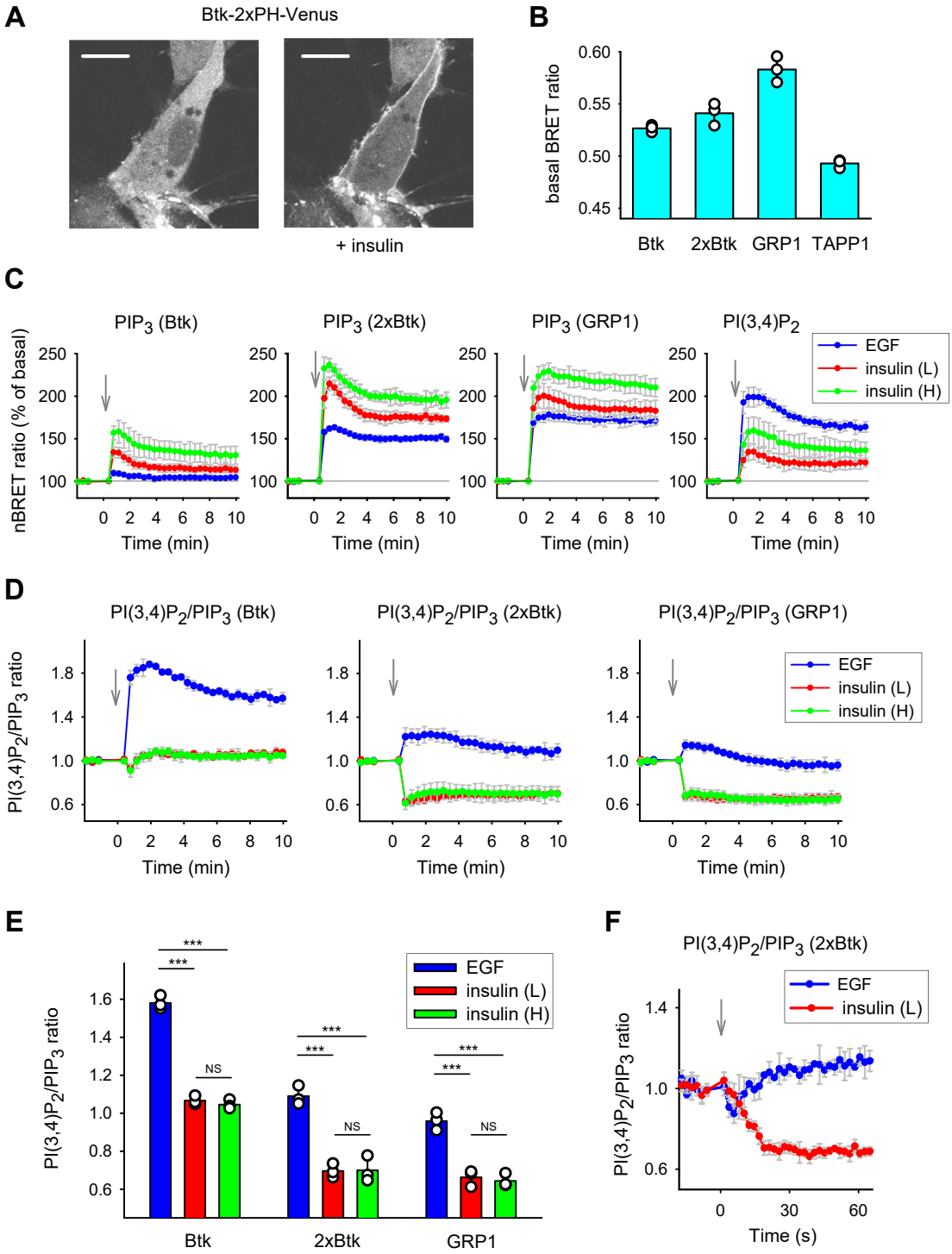

Figure 3. Comparison of EGF and insulin effects on plasma membrane PIP_3 and $PI(3,4)P_2$ levels in HEK293A cells. *A*, representative confocal images of serum starved (5 h) HEK293A cells expressing the Btk-2xPH biosensor tagged with Venus, before and 3 min after stimulation with 70 nM insulin, as indicated. Scale bar: 10 μm. *B*, the bar graph shows the basal BRET ratios of the indicated sensors measured in serum starved cells (5 h). Data are the mean ± SD of 3 independent experiments. *C*, the levels of PIP_3 and $PI(3,4)P_2$ were measured with BRET in HEK293A cells. Cells were transiently transfected with CMV EGFR construct, as well as with the Btk-PH, Btk-2xPH or GRP1-PH sensors to measure PIP_3, or with the TAPP1-2xPH sensor to measure $PI(3,4)P_2$. 28 h after the transfection, serum starved cells (5 h) were treated with EGF (100 ng/ml, *blue curves*), a low (L) or high (H) dose of insulin (70 nM and 0.7 μM, *red* and *green curves*, respectively), at time point indicated by the *arrows*. BRET ratios were calculated as described in Methods and were normalized for the baselines (100%) for each curve. Data are the mean ± SD of 3 independent experiments, each performed in duplicate. *D*, $PI(3,4)P_2/PIP_3$ ratios were calculated similarly to Figure 2*B* using all three PIP_3 sensors in the calculation, as indicated. *E*, the bar graph shows the $PI(3,4)P_2/PIP_3$ ratios with each stimulus. Data are means ± SD of the last 5 measurement points of the curves from *panel D*. For statistical analysis, one-way ANOVA with Holm-Sidak *post hoc* test was used, separately for each sensor. ***$p < 0.001$, NS $p > 0.05$. *F*, the $PI(3,4)P_2/PIP_3$ ratio was measured using the tandem Btk-PH sensor for PIP_3 detection. Experimental conditions were identical to those in *Panel D*, except data were collected at the highest achievable temporal resolution. Results are shown as mean ± SD of 3 independent experiments.

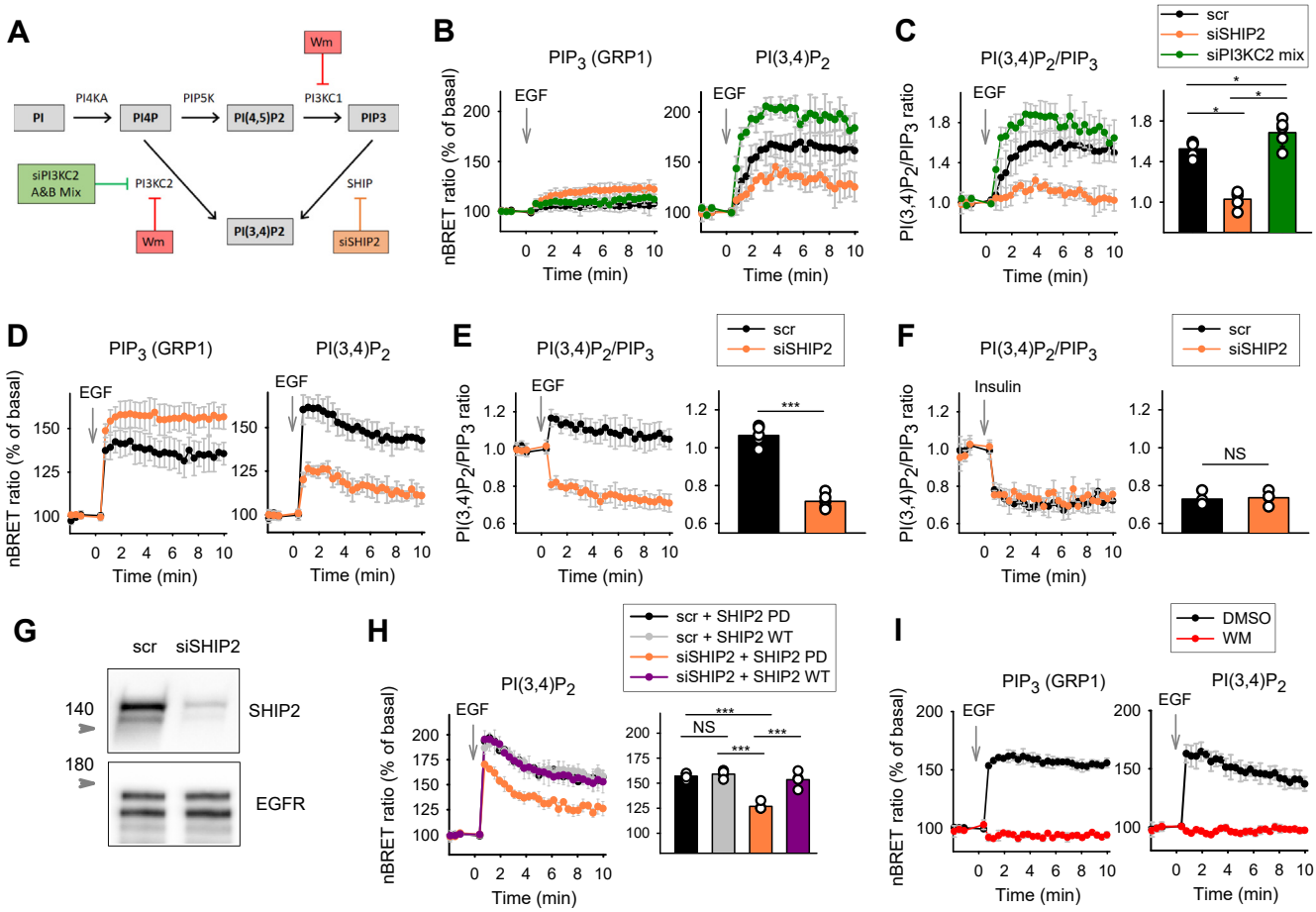

Figure 4. The effect of siRNA-mediated SHIP2 knockdown on EGF signaling pathway. *A*, schematic depiction of the two PI(3,4)P_2 synthetic pathways and the inhibitors used. PI(3,4)P_2 is synthesized either through the 5-phosphatase activity of the SHIP2 enzyme on PIP_3 or *via* the direct phosphorylation of PI4P by class II PI3Ks. *B*, the levels of PI(3,4)P_2 and PIP_3 were measured with BRET in HEK293-AT1 cells. Cells were transfected with scrambled control siRNA (scr – *black curves*) or siRNA targeting SHIP2 (siSHIP2 – *orange curves*) or PI3KC2 (siPI3KC2 mix – *green* curves). 48 h later, cells were transfected with CMV EGFR construct as well as the GRP1-PH sensor to measure PIP_3, or the TAPP1-2xPH sensor to measure PI(3,4)P_2. 28 h after transfection, serum starved cells (5 h) were treated with 100 ng/ml EGF, at time point indicated by the *arrows*, and the BRET ratio was calculated. BRET ratio values were normalized for the baselines (100%) for each curve. Data are the mean ± SD of 5 independent experiments, each performed in duplicate. *C*, the effects of siRNA-mediated knockdown of the PI(3,4)P_2 synthetic pathways on the EGF induced PI(3,4)P_2/PIP_3 ratio in HEK-AT1 cells (*left graph*). The bar graph shows the PI(3,4)P_2/PIP_3 ratio in case of each siRNA, calculated from the last 5 measurement points of the curves from the ratio graph. Data are mean ± SD and for statistical analysis ANOVA on ranks was used with Student-Neuman-Keuls *post hoc* test. *$p < 0.05$. *D*, the levels of PI(3,4)P_2 and PIP_3 following transfection with scrambled siRNA (*black curves*) or siSHIP2 (*orange curves*) were measured with BRET in HEK293A cells as detailed in panel B. Data are the mean ± SD of 5 independent experiments, each performed in duplicate. *E*, the effects of siRNA-mediated SHIP2 knockdown on the EGF-induced PI(3,4)P_2/PIP_3 ratio in HEK293A cells (*left graph*). The bar graph shows data as mean ± SD of the last 5 measurement points of the curves from the ratio graph, statistical significance was evaluated by unpaired, two-tailed *t* test. ***$p < 0.001$. *F*, the effects of siRNA-mediated SHIP2 knockdown on the insulin-induced PI(3,4)P_2/PIP_3 ratio in HEK293A cells (*left graph*). The bar graph shows data as mean ± SD of the last 5 measurement points of the curves from the ratio graph, statistical significance was evaluated by unpaired, two-tailed *t* test. NS: $p > 0.05$. *G*, lysates from HEK293A cells transfected with scrambled control siRNA (scr) or siRNA targeting SHIP2 (siSHIP2) were analyzed by Western blot using anti-SHIP2 and anti-EGFR antibodies. Molecular weights (in kDa) are indicated with *arrows*. *H*, the effects of siRNA-mediated SHIP2 knockdown and rescue on EGF-induced PI(3,4)P_2 level changes in HEK293A cells (*left graph*). Knockdown was carried out as specified in *panel D*, and for the rescue either wild-type (WT) or phosphatase domain deleted (PD) SHIP2 were co-transfected with CMV EGFR and the sensor for PI(3,4)P_2. The bar graph shows data as mean ± SD of the last 5 measurement points of the curves from the time-course graph, statistical significance was evaluated by one-way ANOVA with Holm-Sidak *post hoc* test. ***$p < 0.001$, NS: $p > 0.05$. *I*, the levels of PIP_3 and PI(3,4)P_2 were measured with BRET in HEK293A cells expressing the CMV EGFR construct. Cells were serum-starved (5 h) before being pre-treated with DMSO or wortmannin (Wm, 300 nM) for 30 min. Cells were then stimulated with EGF (100 ng/ml), as indicated by the arrows. Data are the mean ± SD of 3 independent experiments, each performed in duplicate.

SHIP2 knockdown had no effect on the PI(3,4)P_2/PIP_3 ratio following insulin stimulation, suggesting a restricted role of this phosphatase in insulin-induced PIP dynamics (Fig. 4*F*). Since SHIP2 knockdown did not result in complete inhibition of the PI(3,4)P_2 increase with EGF stimulation, we decided to assess the efficacy of SHIP2 depletion in HEK293A cells by immunoblotting, which demonstrated a marked but not complete reduction in SHIP2 protein levels, while EGFR expression remained unaffected (Fig. 4*G*). We further confirmed the specificity of the knockdown with rescue experiments, which showed that the exogenous expression of wild-type (WT), but not the phosphatase domain deleted (PD), SHIP2 was able to restore EGF-induced PI(3,4)P_2 dynamics after SHIP2 knockdown (Fig. 4*H*).

Furthermore, to confirm that the PI(3,4)P_2 surge observed is the consequence of its enhanced synthesis rather than altered degradation, we pre-treated HEK293A cells with 300 nM wortmannin (Wm), a non-selective PI3K inhibitor, for 30 min

before stimulating with EGF. The presence of wortmannin completely eliminated any increase in the levels of PIP_3 and $PI(3,4)P_2$, thus confirming that the observed $PI(3,4)P_2$ surge originates from its increased synthesis (Fig. 4*I*). Taken together, our findings demonstrate that the alterations in $PI(3,4)P_2$ following EGF stimulation are primarily due to enhanced synthesis of $PI(3,4)P_2$ *via* the class I PI3K-SHIP2 pathway. This is further supported by the transient decrease in $PI(3,4)P_2/PIP_3$ ratio immediately following EGF stimulation before its elevation, highlighted by the enhanced temporal resolution data shown in Figure 3*F*.

The effect of EGFR stimulation on SHIP2 phosphorylation

Having established the pivotal role of SHIP2 in the elevation of $PI(3,4)P_2$ following EGF stimulation, we aimed to investigate its regulation in response to EGF and insulin stimulation. To this end we measured its phosphorylation levels, known to correlate with enzymatic activity (29). In this series of experiments, we overexpressed EGFR in HEK293A cells using two distinct approaches: a substantial overexpression and a more physiologically representative, moderate overexpression achieved through different promoters: cytomegalovirus (CMV) and thymidine kinase (TK) promoters for high and low expression, respectively. 28 h following transfection, serum-starved cells were stimulated with EGF and the two previously selected insulin concentrations for 5 min. Cell lysates were analyzed through Western blotting.

Stimulation with EGF resulted in the phosphorylation of SHIP2 at tyrosine positions 986/987 and 1135. Contrarily, stimulation with insulin did not induce SHIP2 phosphorylation, even after a tenfold increase in the concentration (Fig. 5*A*). As expected, EGF-induced SHIP2 phosphorylation was more pronounced in cells with higher EGFR overexpression (Fig. 5*A*, left images) but was still detectable in cells with moderate overexpression (Fig. 5*A*, right images). To confirm that the used stimuli concentrations are effective we further compared the signaling of EGF and insulin in two additional pathways, a PI3K-dependent pathway, Akt, and a PI3K independent one, ERK (22, 30). As PI3K activation is shared between EGF and insulin, both stimulations resulted in Akt phosphorylation. However, ERK was phosphorylated with the EGF pathway only. We also examined EGFR phosphorylation which occurred only with EGF, as expected. These observations were consistent across both levels of receptor overexpression (Fig. 5*A*). Immunoblotting images of SHIP2 phosphorylation at tyrosine position 1135 were quantified and statistically tested (Fig. 5*B*).

As our BRET measurements indicated that changes in PIP levels following EGF stimulation were rapid (Fig. 3*F*), we examined the dynamics of SHIP2 phosphorylation at tyrosine position 1135 with a higher temporal resolution, using eight different durations of EGF exposure rather than only 5 min. Results demonstrated that SHIP2 phosphorylation was discernible as early as 5 s post-EGF stimulation and increased steadily with longer durations of stimulation, reaching its peak intensity at 10 min (Fig. 5, *C* and *D*).

To address potential concerns that EGFR overexpression could affect PIP dynamics, we conducted BRET-based lipid measurements in cells exhibiting either endogenous EGFR levels or overexpression driven by the TK or CMV promoters. All conditions displayed a consistent pattern of phosphoinositide response upon EGF stimulation, with higher EGFR expression correlating with more sustained lipid alterations (Fig. 5*E*, upper graphs). Insulin-induced PIP patterns were also not affected by EGFR overexpression (Fig. 5*E*, lower graphs).

In conclusion, our findings demonstrate that the observed surge in $PI(3,4)P_2$ following EGF stimulation can be attributed to the enhanced activity of SHIP2, likely facilitated by its phosphorylation. Notably, this phosphorylation of SHIP2 is absent with insulin stimuli, highlighting the different signaling patterns for these two tyrosine kinase receptors.

PIP signaling dynamics upon EGF and insulin stimulation in HeLa cells with endogenous EGFR expression

Given that EGF receptor expression can be variable in HEK cell lines thus necessitating receptor overexpression, we sought a cell line with stable, endogenous EGF receptor expression. We therefore selected HeLa cells, which respond robustly to both EGF and insulin (31–33). These cells were transfected with our $PI(3,4)P_2$ and PIP_3 biosensors. 28 h later, serum-starved cells were stimulated with 100 ng/ml EGF or 70 nM insulin, and BRET ratio changes were measured. The resulting $PI(3,4)P_2$ and PIP_3 dynamics closely resembled those observed in HEK cells. Although insulin produced a comparatively larger increase in PIP_3, EGF elicited a more pronounced elevation of $PI(3,4)P_2$ (Fig. 6*A*, red and blue curves respectively). Analysis of the $PI(3,4)P_2/PIP_3$ ratio confirmed that, similar to both examined HEK cell lines, EGF consistently yielded a higher ratio than insulin, regardless of which PIP_3 sensor was used (Fig. 6, *B* and *C*). We also performed the same immunoblotting analysis as in HEK293A cells, revealing comparable outcomes, including phosphorylation of SHIP2 at two tyrosine sites upon EGF stimulation (Fig. 6*D*). In conclusion, the observed PIP patterns and SHIP2 dynamics are not exclusive to HEK-derived cell lines and do not require receptor overexpression. Instead, they are also evident in a cell line with endogenous EGF receptor expression, reinforcing the broader applicability of our findings.

Bioinformatics analysis of SHIP2 involvement in intracellular signaling pathways

Taken together, our findings suggest a more significant involvement of SHIP2 in the EGFR signaling pathway as compared to the insulin receptor (IR) pathway. To further substantiate this observation, we utilized a bioinformatics approach with the L-1000 database (refer to Methods for details). This analysis involved comparing gene expression signatures from SHIP2 manipulation (both inhibition and activation) against those resulting from the manipulation of other proteins. The results, presented in Figure 7, show the distribution of normalized correlation scores, which quantify the similarity between SHIP2-associated gene expression

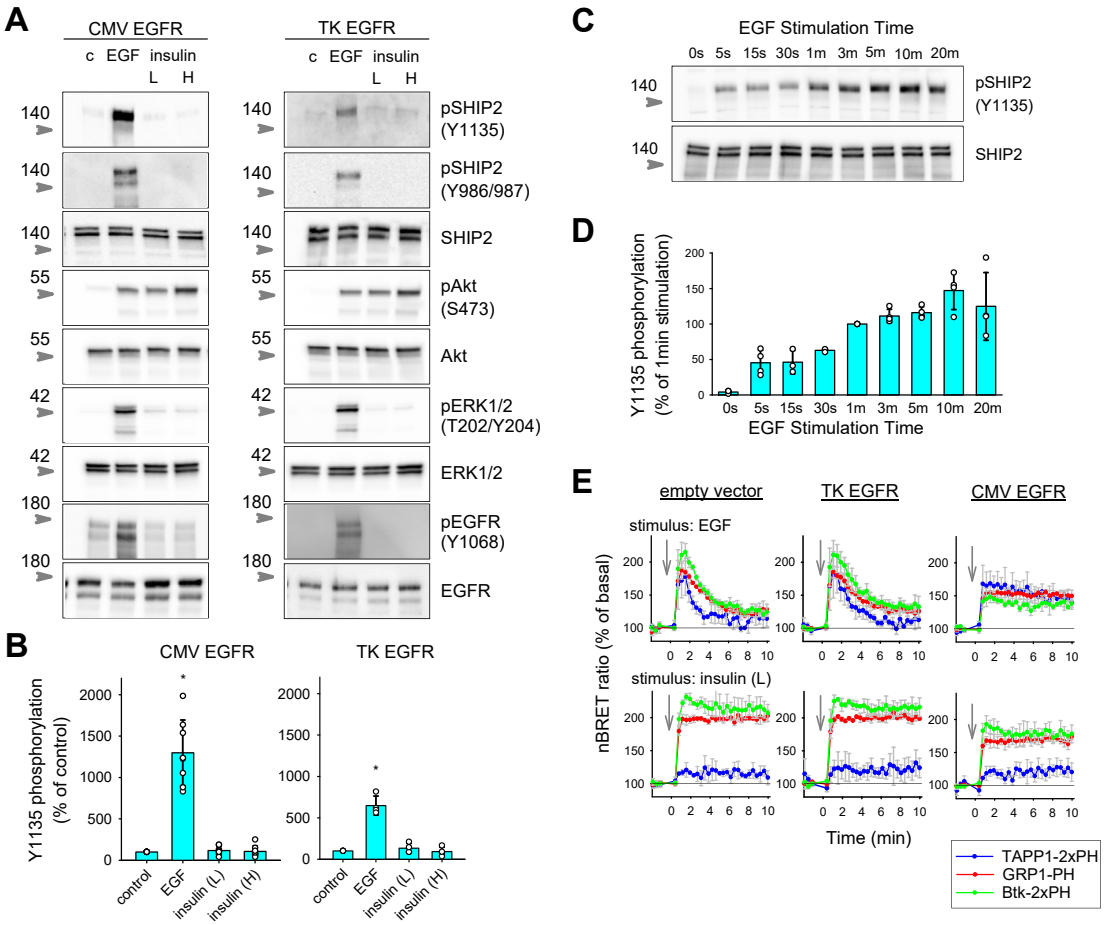

Figure 5. The effect of EGFR stimulation on SHIP2 phosphorylation. *A*, EGFR was expressed at two different levels in HEK293A cells, using either CMV or TK promoters to achieve substantial and moderate overexpression, respectively. Serum starved (5 h) samples were stimulated with 100 ng/ml EGF, 70 nM insulin (L) or 0.7 μM insulin (H), as indicated, for 5 min. Cell lysates were then analyzed with Western blot using antibodies for the indicated proteins. Phospho-specific antibodies are marked with an initial p, and the sites of phosphorylation are indicated in brackets. The total protein amounts are shown as loading controls. Molecular weights (in kDa) are indicated with arrows. *B*, immunoblot quantification of phospho-SHIP2 at Tyr1135 as shown on *panel A*, separately for substantial overexpression (*left graph*) and moderate overexpression (*right graph*) of EGFR. Quantification values were normalized for the control (100%) for each experiment. Data are the means ± SD from 4 to 8 independent experiments. For statistical analysis ANOVA on ranks was used with Student-Neuman-Keuls *post hoc* test, and EGF-treated samples were significantly different from all other samples (*$p < 0.05$), while insulin treatment caused no significant change. *C*, Western blot analysis of SHIP2 phosphorylation at tyrosine 1135 following EGF stimulation over various time points (5 s to 20 min, as labeled above each lane) in HEK293A cells overexpressing EGFR (CMV). The upper panel displays phosphorylated SHIP2 (pSHIP2 Y1135), while the lower *panel* shows total SHIP2, which served as a loading control. *Arrows* on the *left* indicate the molecular weight marker at 140 kDa. *D*, immunoblot quantification of phospho-SHIP2 on *panel C*. Quantification values were normalized for the 1 min EGF stimulation (100%) for each experiment. Data are the means ± SD from 3 to 4 independent experiments. *E*, the levels of PIP_3 and $PI(3,4)P_2$ were measured with BRET in HEK293A cells transiently transfected with the different EGFR constructs (as indicated) and PIP sensors (as detailed in Fig. 3). Serum starved cells (5 h) were treated with EGF (100 ng/ml) or insulin (70 nM) at time points indicated with *arrows*, and BRET ratios were processed as detailed in the methods. Data are the mean ± SD of 3 independent experiments, each performed in duplicate.

changes and those induced by other proteins. Specifically, positive scores denote concordant expression patterns, while negative scores indicate opposing effects. The results display a distinct bimodal distribution with sharp peaks at −1 and +1, underscoring strong reciprocal or parallel transcriptional responses linked to SHIP2 activity.

In the graph, significant hits are concentrated in the two tails, with their importance increasing the farther they are from the zero point. Triangles mark the correlation scores: blue for EGFR and red for IR manipulations relative to SHIP2 manipulations. The results clearly show a disparity in the correlation values. While the IR profiles exhibit only moderate similarity to SHIP2 perturbations, appearing in the less significant portions of the distribution, the EGFR profiles predominantly cluster in the positive tail of the distribution (in the higher, more significant values). This indicates strong similarities between EGFR and SHIP2 perturbations, affirming the critical role of SHIP2 within the EGFR signaling network, far more than within the IR pathway.

Mechanism of SHIP2 phosphorylation upon EGF stimulation and its effect on PIP dynamics

After noting enhanced SHIP2 phosphorylation following EGFR stimulation, which produces a unique PIP pattern distinct from IR stimulation, we sought to explore the specific molecular mechanism driving SHIP2 phosphorylation during EGFR activation. Both EGFR and IR are receptor tyrosine

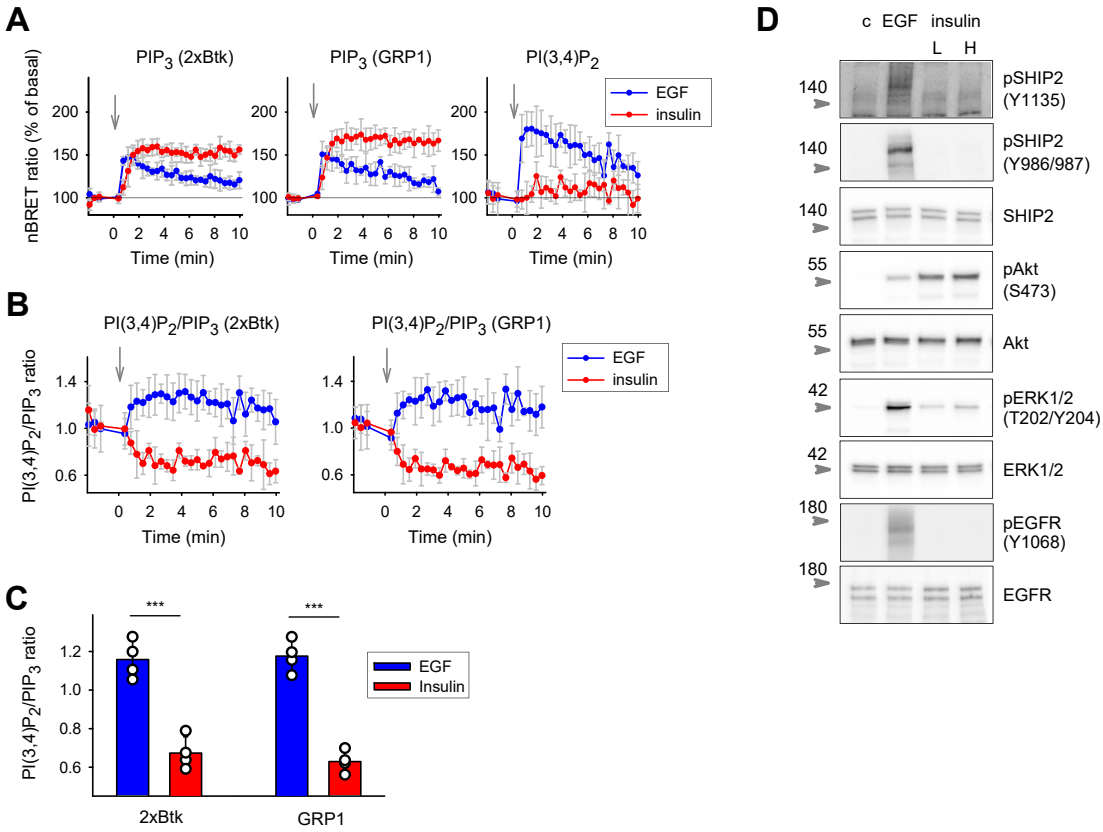

Figure 6. Comparing the effect of EGF and insulin stimulation in HeLa cells. *A*, the levels of PIP_3 and $PI(3,4)P_2$ were measured with BRET in HeLa cells. Cells were transiently transfected with the Btk-2xPH or GRP1-PH sensors to measure PIP_3, or with the TAPP1-2xPH sensor to measure $PI(3,4)P_2$. 28 h after the transfection, serum starved cells (5 h) were treated with EGF (100 ng/ml, *blue curves*) and insulin (70 nM, *red curves*), at time point indicated by the *arrows*. BRET ratios were calculated as described in Methods and were normalized for the baselines (100%) for each curve. Data are the mean ± SD of 4 independent experiments, each performed in duplicate. *B*, $PI(3,4)P_2/PIP_3$ ratios were calculated similarly to Figures 2*B* and 3*D* using both PIP_3 sensors in the calculation, as indicated. *C*, the bar graph shows the $PI(3,4)P_2/PIP_3$ ratios with each stimulus. Data are means ± SD of the last 5 measurement points of the curves from *panel B*. For statistical analysis, EGF- and insulin-induced changes were compared with an unpaired, two-tailed *t* test for each sensor separately. ***$p < 0.001$. *D*, serum starved (5 h) HeLa cells were stimulated with 100 ng/ml EGF, 70 nM insulin (L) or 0.7 μM insulin (H), as indicated, for 5 min. Cell lysates were then analyzed with Western blot using antibodies for the indicated proteins. Phospho-specific antibodies are marked with an initial p, and the sites of phosphorylation are indicated in brackets. The total protein amounts are shown as loading controls. Molecular weights (in kDa) are indicated with *arrows*.

kinases and share many signaling pathways such as PI3K activation, but a unique feature of EGFR signaling not associated with the IR pathway is PLCγ-induced calcium increase (22, 24). Consequently, we started with exploring the potential role of both PI3K and PLCγ pathways in SHIP2 phosphorylation. To investigate the role of calcium signaling, we employed immunoblotting utilizing the calcium chelator BAPTA-AM in HEK293A cells. Initially, cells were transfected with EGFR and, after 28 h, serum-starved cells were pre-treated for 30 min with either BAPTA-AM or DMSO before stimulation with EGF and the two previously selected insulin concentrations for 5 min. Calcium chelation resulted in a partial but significant attenuation of EGF-induced phosphorylation at both Y1135 and Y986/987 of SHIP2 (Fig. 8*A*). To confirm effective calcium chelation with BAPTA-AM pre-treatment we conducted cytoplasmic calcium measurements in HEK293A using our previously developed BRET calcium sensors (34), and were able to confirm effective calcium buffering by BAPTA-AM compared to DMSO pre-treatment following EGF stimulation (Fig. 8*B*).

To determine the role of PI3K in SHIP2 phosphorylation we conducted similar immunoblotting experiments using wortmannin pre-treatment in HEK293A. Similarly to BAPTA-AM, 30 min of wortmannin pre-treatment resulted in a partial but substantial attenuation of EGF-induced SHIP2 phosphorylation at both tyrosine sites. To confirm effective inhibition of PI3Ks by wortmannin, Akt phosphorylation was also measured with immunoblotting, which showed complete suppression (Fig. 8*C*). Finally, 30-min pre-treatment using both BAPTA-AM and wortmannin resulted in a strong attenuation of SHIP2 phosphorylation (Fig. 8*D*). This combined pre-treatment proved to cause significantly greater inhibition compared to individual treatments, when immunoblotting images were quantified and statistically tested (Fig. 8*E*).

Recognizing the PLCγ-induced calcium signaling as a key determinant in SHIP2 phosphorylation, we aimed to investigate this pathway in a more specific manner. Cells transfected with EGFR were serum-starved and then pre-treated for 30 min with U73122, a PLC inhibitor, or with DMSO and U73343 (specific negative control), prior to a 5-min

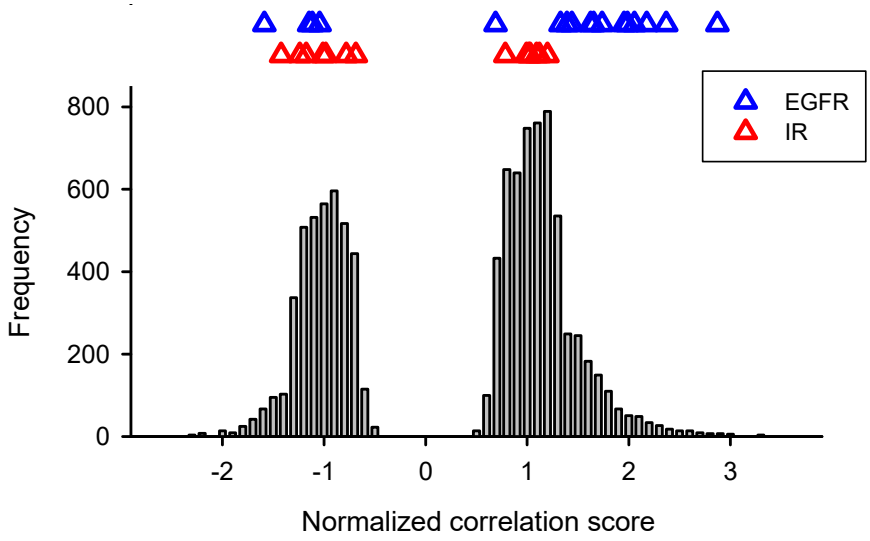

Figure 7. Bioinformatics analysis of SHIP2 involvement in intracellular signaling pathways. This bar chart illustrates the distribution of Pearson correlation scores that quantify the degree of similarity between SHIP2 perturbation profiles and various other perturbation profiles within the L-1000 database (detailed in the Methods section). Each bar corresponds to the frequency of scores across specified intervals. Above these bars, colored triangles mark specific correlation values: *blue triangles* for scores derived from SHIP2/EGFR perturbation profile correlations, and *red triangles* for those from SHIP2/IR perturbation profile correlations. These color-coded markers help illustrate the comparative analysis of how SHIP2 interacts with the EGFR and IR signaling pathways.

stimulation with EGF. Inhibition of PLC markedly reduced EGF-induced phosphorylation of SHIP2 at both tyrosine residues Y1135 and Y986/987 (Fig. 8*F*), which proved significant after quantification (Fig. 8*G*). Given ongoing debates about the impact of SHIP2 phosphorylation on its phosphatase activity, we further explored the effects of PLC inhibition on the PI(3,4)P_2/PIP_3 ratio using BRET. Our results indicated a significant decrease in this ratio following PLC inhibition with EGF stimulation, while, as expected, insulin-induced changes remained unaffected (Fig. 8*H*).

Discussion

In this study, we employed our BRET-based biosensors to monitor PIP levels at the PM in real-time. This approach allowed us to recognize distinct signaling behaviors in response to EGF and insulin stimulation. Notably, although both EGF and insulin elevated PIP_3 and PI(3,4)P_2 levels, EGF consistently generated a higher PI(3,4)P_2/PIP_3 ratio compared to insulin in both HEK cell lines and in HeLa cells. This observation suggests a preferential production of PI(3,4)P_2 during EGF signaling. Using siRNA-mediated knockdown of both PI(3,4)P_2 synthetic pathways, we demonstrated that SHIP2 is primarily responsible for regulating PI(3,4)P_2 levels at the membrane during EGF stimulation. This was corroborated by siRNA rescue experiments and enhanced temporal resolution BRET measurements of the PI(3,4)P_2/PIP_3 ratio. On the other hand, SHIP2 knockdown had no influence on insulin-induced PIP dynamics. Additionally, phosphorylation of SHIP2 was observed following EGF but not insulin stimulation, indicating a distinct role of SHIP2 in modulating the PI3K signaling pathway in response to EGF. Moreover, we found that while SHIP2 phosphorylation in the EGF pathway depends partially on PI3K activity, it is primarily driven by the PLC-induced calcium signal. Beyond reduction in SHIP2 phosphorylation, inhibition of PLC also significantly reduced the PI(3,4)P_2/PIP_3 ratio, strongly suggesting a role for SHIP2 phosphorylation in regulating its phosphatase activity. These findings provide new insights into receptor-specific phosphoinositide dynamics and emphasize how differential growth factor signaling can shape unique lipid signaling profiles at the PM, potentially influencing downstream cellular responses.

In our experiments, we used several different sensors for PIP_3. Although these sensors contain only the lipid-binding PH domains of their respective original proteins (GRP1 or Btk), they might still differ in their affinity and binding kinetics and thus behave differently under the same conditions, as can be seen on the confocal images of Figure 1*B*. This discrepancy between GRP1- and Btk-based sensors is reflected in the basal BRET ratios as well (Fig. 1*C*), although this signal might be additionally influenced by the relative orientation of the BRET donor and acceptor molecules in each sensor (35). To enhance the relatively small signals, we introduced a tandem dimer version of our Btk-based sensor which we expected to have increased avidity. Indeed, our artificially duplicated sensor showed a slightly higher signal already at resting PIP_3 levels (Fig. 3*B*), and a substantially larger increase after receptor stimulation compared to the single Btk PH domain version (Fig. 3*C*). This finding is in line with a recent study reporting on the complex dynamics of Btk lipid binding and activation which features a sharp sensitivity for PIP_3 density in the PM (36).

We started our studies with HEK293-AT1 cells, a cell line stably expressing type 1A angiotensin receptor, which has been

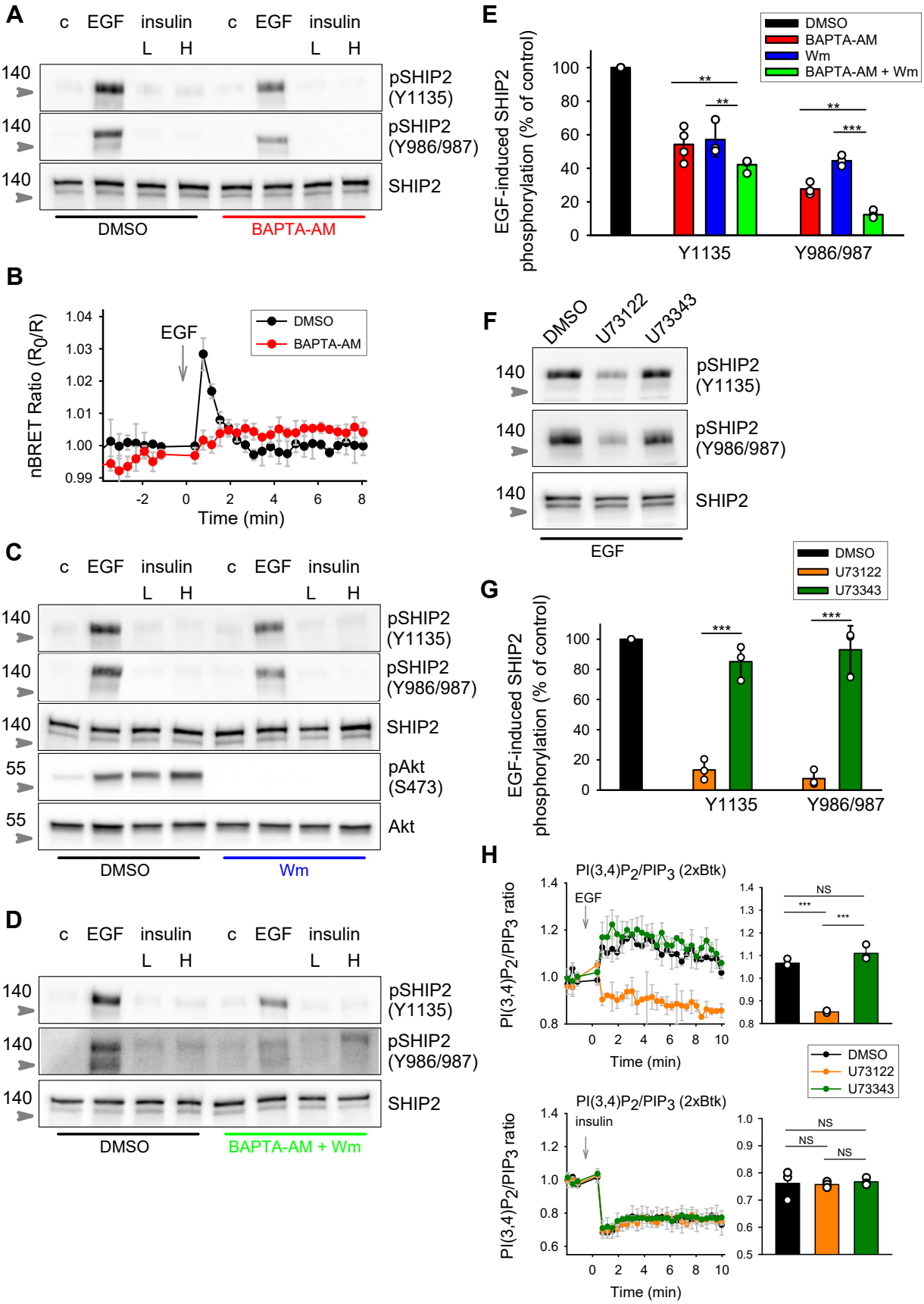

Figure 8. Mechanism of SHIP2 phosphorylation upon EGF stimulation. *A*, Western blot analysis of phospho-SHIP2 levels at tyrosine positions 1135 and 986/987 in HEK293A cells expressing the CMV EGFR construct. Serum-starved (5 h) cells, pre-treated for 30 min with either DMSO or BAPTA-AM (20 μM), were stimulated with 100 ng/ml EGF, 70 nM insulin (L) or 0.7 μM insulin (H), as indicated, for 5 min. Anti-SHIP2 measurement was used as loading control.

used by our group in several previous studies (27, 37, 38). However, we wanted to check our findings in a more generally used cell line as well, which led us to use HEK293A cells in subsequent experiments. Although these two cell lines have common origins, we found striking differences in their PIP response to the same stimuli, especially in PIP_3 changes as measured by the GRP1-based sensor (Figs. 2*A* and 3*C*). We speculate that this discrepancy might be due to higher resting PI3K activity in HEK293-AT1 cells, supported by elevated GRP1-PH basal BRET ratios in these cells (compare Figs. 1*C* and 3*B*). However, we did not investigate this further as our main focus was the divergent responses evoked by EGF and insulin, which were more consistent in both cell lines as determined by the $PI(3,4)P_2/PIP_3$ ratio (see Figs. 2*C* and 3*E*).

Our results indicate that SHIP2, using PIP_3 generated by class I PI3Ks, serves as the primary source of $PI(3,4)P_2$ in the EGF signaling pathway, rather than class II PI3Ks (Fig. 4*B*). This is in line with the notion that class II PI3K does not contribute significantly to signaling-related $PI(3,4)P_2$ dynamics (28) but rather generates localized, small pools of $PI(3,4)P_2$ at endocytic vesicles (39). Interestingly, however, siRNA-mediated knockdown of class II PI3K resulted in an increase in $PI(3,4)P_2$ levels following EGF stimulation. Since class II PI3K is one of the main enzymes involved in $PI(3,4)P_2$ synthesis (14) and is known to be recruited and activated by EGFR (40, 41), this finding was surprising. A plausible explanation for this result could lie in the critical role of Class II PI3K in receptor endocytosis (14). The knockdown of class II PI3K may disrupt EGFR internalization upon EGF stimulation, thereby prolonging EGFR activation at the PM and enhancing $PI(3,4)P_2$ production.

To assess SHIP2 regulation in response to EGF and insulin, we examined its phosphorylation status, specifically at tyrosine residues 986/987 and 1135. Our observations confirm phosphorylation at these sites following EGF stimulation (Fig. 5*A*), aligning with previous studies (42). We further explored the temporal dynamics of SHIP2 phosphorylation across different EGF exposure times, noting discernible phosphorylation as early as 5 s post-stimulation, which steadily increased, peaking at 10 min (Fig. 5, *C* and *D*). The impact of SHIP2 tyrosine phosphorylation on its phosphatase activity remains a topic of debate. While some studies suggest that it enhances the phosphatase activity of SHIP2 (42), others propose that its activity is regulated more by changes in subcellular localization than by its phosphorylation state (43). Our results demonstrate that SHIP2 tyrosine phosphorylation coincides with significant PIP_3-to-$PI(3,4)P_2$ conversion in the EGF signaling pathway, as shown by BRET lipid measurements, suggesting that phosphorylation may enhance SHIP2 function, either by modulating its localization or by directly increasing its phosphatase activity.

To confirm our results on a broader spectrum of conditions and cellular contexts, we used a bioinformatics approach where gene expression changes after perturbations (genetic or chemical activation or inactivation) of specific proteins were compared across many cell types and different conditions, based on an existing database named LINCS-L1000. We set out to determine the correlation between SHIP2 perturbation induced gene expression profiles and that of other proteins, and after quantification, we observed much higher correlation scores for EGFR perturbations compared to insulin receptor (IR) manipulations (blue and red triangles on Fig. 7, respectively). This confirmed a stronger connection between the signaling networks of SHIP2 and EGFR overall. However, we also detected negative scores (representing anti-correlation) which highlight that the interaction between SHIP2, and these receptors can be highly dependent on the cellular context. Furthermore, the cell lines in the LINCS-L1000 database are mostly of tumor origin and their gene regulatory machinery is likely to be damaged. In addition, the time course of the response of the gene expression level to a perturbation is different for the different genes in the profile. The actual time point presented in the database may not optimally capture the similarity between two patterns. Despite these limitations, we believe that this statistically robust method supports the involvement of SHIP2 in the EGF response.

We demonstrated that EGF-induced SHIP2 phosphorylation at the investigated tyrosine residues is partially reduced by both calcium chelation and PI3K inhibition, with varying effects at each site (Fig. 8*E*). This variation may be due to differences in antibody sensitivity or distinct regulatory mechanisms affecting each phosphorylation site. Given the varied impacts of phosphorylation on SHIP2 function, where

Molecular weights are indicated with *arrows* (140 kDa). *B*, cytoplasmic calcium measurements with a BRET-based sensor in serum-starved HEK293A cells pre-treated for 30 min with either DMSO or BAPTA-AM. Cells were stimulated with EGF as indicated, and BRET ratios were normalized to the control period of DMSO-pretreated samples. Data are the mean ± SD of 3 independent experiments, each performed in duplicate. *C*, Western blot analysis of phospho-SHIP2 and phospho-Akt levels in HEK293A cells. All conditions were the same as on *panel A*, except for the 30-min pre-treatment with 100 nM Wortmannin (Wm). Anti-SHIP2 and anti-Akt measurements were used as loading control. *D*, Western blot analysis of phospho-SHIP2 levels. All conditions were the same as on *panel A*, except for the 30-min combined pre-treatment with BAPTA-AM and Wm. *E*, immunoblot quantification of EGF-induced phospho-SHIP2 levels at tyrosine sites Y1135 and Y986/987 with the indicated pre-treatments. Values were normalized for the DMSO pre-treated samples (100%) for each experiment. Data are the means ± SD from 3 to 4 independent experiments. For statistical analysis two-way ANOVA was used with Holm-Sidak *post hoc* test. All pre-treated samples were significantly different from their respective control. Significance is indicated only for comparisons of particular interest. $^{**}p < 0.01$, $^{***}p < 0.001$. *F*, Western blot analysis of EGF-induced SHIP2 phosphorylation levels following 30 min pre-treatment with DMSO, U73122 (10 μM) or U73343 (10 μM, negative control). *G*, immunoblot quantification of EGF-induced phospho-SHIP2 levels at tyrosine sites Y1135 and Y986/987 with the indicated pre-treatments. Values were normalized for the DMSO treated samples (100%) for each experiment. Data are the means ± SD from 3 independent experiments. For statistical analysis, one-way ANOVA with Holm-Sidak *post hoc* test was used, separately for each phosphorylation site. There was no significant difference between DMSO and U73343 pre-treatment. $^{***}p < 0.001$. *H*, the $PI(3,4)P_2/PIP_3$ ratio was analyzed using the tandem Btk-PH-based PIP_3 sensor and the TAPP1-2xPH sensor to measure $PI(3,4)P_2$. HEK293A cells expressing CMV EGFR construct were serum-starved (5 h) before being pre-treated with DMSO, U73122 (10 μM), or U73343 (10 μM) for 30 min. Cells were then stimulated with EGF (100 ng/ml, *upper graph*) or insulin (70 nM, *lower graph*), as indicated by the *arrows*. Data are the mean ± SD of 3 independent experiments, each performed in duplicate. The bar graphs illustrate the $PI(3,4)P_2/PIP_3$ ratios associated with each pre-treatment, presented as mean ± SD of the last 5 measurement points from the ratio graphs. Statistical significance was determined using one-way ANOVA and Holm-Sidak *post hoc* test was used for EGF-stimulated groups. $^{***}p < 0.001$, NS $p > 0.05$.

some sites correlate with increased degradation (44) and others with enhanced enzymatic activity (29, 42), further research is essential to delineate the specific roles and regulatory mechanisms of each site. As the calcium signal appears to be the dominant driver of SHIP2 phosphorylation, we used a PLC inhibitor prior to EGF stimulation, which revealed a nearly complete inhibition of SHIP2 phosphorylation as well as a significantly reduced $PI(3,4)P_2/PIP_3$ ratio (Fig. 8, *F–H*). This highlights the potential impact of SHIP2 phosphorylation on its phosphatase activity. Moreover, while some studies have suggested that the kinase responsible for SHIP2 phosphorylation is likely a Src family member (43, 44), additional studies are required to identify the specific kinase involved. Since SHIP2 is being targeted pharmacologically, a thorough understanding of its regulatory mechanisms is crucial for therapeutic development (21).

In this study, we utilized U73122 to inhibit PLC to investigate its influence on SHIP2 phosphorylation within the EGF signaling pathway (Fig. 8, *F–H*). However, despite its widespread use, U73122 is notorious for its off-target effects (45, 46) and inconsistent efficacy, with some reports even suggesting paradoxical activation rather than inhibition of certain PLC isoforms *in vitro* (47). These effects are likely contingent on the specific conditions under which U73122 interacts with PLC. It has been proposed that while U73122 may activate cytosolic PLC enzymes, it could inhibit membrane-associated PLCs (47), the latter being the focus of our *in vivo* studies. Furthermore, there is no valid pharmacological alternative for targeting PLC, with the other options also known for their problematic nonspecific inhibition (48, 49). Therefore, U73122 was used as a complementary approach to calcium chelation, both of which had similar effects on EGF-induced SHIP2 phosphorylation. Nevertheless, due to the known limitations of U73122, these findings must be interpreted with caution. This highlights the critical need for further research to clearly define the role of PLC in inducing SHIP2 phosphorylation within the EGF pathway.

Our study did not detect SHIP2 phosphorylation at the examined sites following insulin stimulation, even with a tenfold increase in concentration (Fig. 5). In contrast, a previous study has observed SHIP2 phosphorylation in response to insulin, in a model with stable overexpression of the insulin receptor (50). Another study found that this insulin-induced phosphorylation varied even between different developmental stages of the same cell line (51). Taken together, these findings suggest that SHIP2 phosphorylation may depend on specific experimental conditions and cellular context. Despite these discrepancies, the role of SHIP2 as a key negative regulator in insulin signaling is well established. This important role is well demonstrated by SHIP2 overexpression being associated with insulin resistance, while targeting it has been shown to improve insulin sensitivity and glucose homeostasis, making it a potential therapeutic target for managing insulin resistance and metabolic disorders (21, 52).

EGFR overexpression in our experiments in HEK293-derived cell lines was necessary due to variability in endogenous receptor levels. As this may alter downstream signaling, we performed BRET-based lipid measurements with cells expressing either endogenous EGFR or the two overexpression levels, driven by either the TK or CMV promoter. All expression levels showed a consistent phosphoinositide pattern upon EGF stimulation, with higher EGFR expression leading to more sustained lipid changes. Notably, PIP dynamics were nearly identical in case of endogenous and TK-driven overexpression, suggesting that the TK promoter closely mirrors physiological conditions (Fig. 5*E*). To validate these findings beyond HEK cells, we utilized HeLa cells, chosen for their stable, robust response to both EGF and insulin through endogenous receptors. BRET lipid measurements and immunoblotting results in HeLa cells (Fig. 6) were consistent with those observed in the EGFR-overexpressing HEK cells. This confirms that the PIP patterns and SHIP2 dynamics identified are not unique to modified HEK cell lines but are also present in cells with native EGFR expression, thus underscoring the broader applicability of our findings.

Our BRET measurements, together with the $PI(3,4)P_2/PIP_3$ ratio analysis, reveal a preferential production of $PI(3,4)P_2$ in the EGF signaling pathway compared to insulin signaling. Given that $PI(3,4)P_2$ is a well-established signaling molecule involved in various cellular processes, these distinct dynamics in $PI(3,4)P_2$ production may contribute to downstream functional differences between the two pathways. However, experimentally evaluating these differences poses a significant challenge, as the role of $PI(3,4)P_2$ is highly context-dependent. $PI(3,4)P_2$ has been shown to play a crucial role in diverse cellular contexts, such as platelet function (53) and cataract prevention (54), which limits the applicability of testing its effects in our current system. Nevertheless, one pathway we were able to evaluate was the impact of differential $PI(3,4)P_2$ and PIP_3 production in the EGF and insulin signaling pathways on the activation of Akt isoforms. Since Akt1 is predominantly activated by PIP_3 and Akt2 by $PI(3,4)P_2$ (55), we hypothesized that EGF signaling would preferentially activate Akt2 compared to insulin. To test this, we analyzed Akt isoform activation using immunoblotting for Akt phosphorylation. However, our results revealed no significant difference in the phosphorylation patterns of Akt isoforms between EGF and insulin (data not shown). The precise role of preferential $PI(3,4)P_2$ production in modulating signaling pathways remains unclear and warrants further investigation.

Experimental procedures

Materials

Molecular biology reagents, Lipofectamine 2000 (Cat. No. 11668019) and Lipofectamine RNAiMAX (Cat. No. 13778150), were purchased from Thermo Fisher Scientific. Coelenterazine-H was purchased from Regis Technologies (1–361304–200). BAPTA-AM (Cat. No. 2787), U73122 (Cat. No. 1268), and U73343 (Cat. No. 4133) were from Tocris, and insulin was from Eli Lilly. Unless otherwise stated, all other chemicals and reagents were purchased from Sigma-Aldrich.

DNA constructs

To prepare the CMV EGFR and TK EGFR constructs, the coding sequence of the previously used EGFR was cloned to the Clontech pEGFP-N1 vector containing either the cytomegalovirus (CMV) or the thymidine kinase (TK) promoters (56). Using the NheI and Bsp1407I restriction enzymes, the EGFP sequence was replaced with the receptor sequence. In addition to the previously created and characterized PM PIP_3 and PI(3,4)P_2 BRET-based biosensors (L10-mVenus-T2A-Btk-PH-Luciferase, L10-mVenus-T2A-NES-Luciferase-GRP1-PH and L10-mVenus-T2A-Luciferase-TAPP1-2xPH) (27, 57) we created the tandem version of Btk-PH-containing biosensor (L10-mVenus-T2A-Btk-2xPH-Luciferase) by inserting the sequence of a second PH domain between the PH and luciferase sequences using the AgeI restriction site. In the construct, the two PH domains are connected by the DPPVAAGAGGAG linker. Using the same strategy, mVenus-tagged Btk-2xPH constructs was also created. Mammalian expression vectors coding wild-type (WT) and phosphatase domain deleted (PD) human SHIP2 were purchased from Addgene (No. 214907 and 214,901) (58). All constructs were checked by sequencing.

Cell culture

HEK293-AT1 cells (a line that stably expresses the type-1A rat angiotensin II receptor (AT1AR) (37)), HEK293A (Thermo Fisher Scientific, Cat. No. R70507) and HeLa cells (ATCC, CCL-2) were maintained in Dulbecco's modified Eagle's medium (DMEM, Gibco 11,995,065) supplemented with 10% fetal bovine serum (Biosera, FB-1200), 50 U/ml penicillin and 50 μg/ml streptomycin (Gibco, 15,140–122). HEK293-AT1 cells were also treated with 5 μg/ml Plasmocin (InvivoGen, ant-mpp) as a *mycoplasma* prophylactic and were regularly tested for *mycoplasma* contamination. All cell lines were cultured in a 5% humidified CO_2 incubator at 37 °C in 10 cm tissue culture plastic dishes.

Confocal microscopy

HEK293-AT1 or HEK293A cells were seeded at a density of 3×10^4 cells/well on poly-L-lysine-pretreated (0.001%, 1 h) IBIDI 8-well μ-Slides (Cat. No. 80826) and cultured at 37 °C in DMEM for 1 day. For transfection, the culture medium was changed to 200 μl transfection mixture containing the indicated DNA constructs (0.2 μg total DNA/well) and 0.33 μl/well Lipofectamine 2000. After 6 h, the medium was changed to 300 μl supplemented DMEM medium. Cells were inspected 24 to 26 h after transfection using a Zeiss LSM 710 laser confocal microscope with a 63 × /1.4 oil-immersion objective. Cells were serum-depleted for 5 h where indicated and medium was changed to modified Krebs–Ringer buffer (120 mM NaCl, 4.7 mM KCl, 1.2 mM $CaCl_2$, 0.7 mM $MgSO_4$, 10 mM glucose and 10 mM Na-HEPES, pH 7.4) at room temperature before experiments. Post-acquisition picture analysis was performed using Fiji and Photoshop (Adobe) software. Only linear changes were made during picture analysis and processing.

Bioluminescence resonance energy transfer (BRET) measurements

For BRET measurements, HEK293-AT1, HEK293A or HeLa cells were trypsinized (0.25% Trypsin, Lonza BE17–160E) and plated on poly-L-lysine-pretreated (0.001%, 1 h) white 96-well plates (Greiner bio-one, 655,083) at a density of 6×10^4 cells/well together with the indicated DNA constructs (0.03–0.04 μg of total DNA/well) and the cell transfection reagent (0.25 μl/well Lipofectamine 2000) in Opti-MEM reduced serum medium (Gibco, 31,985,047). Cells were serum-starved (5 h) before starting the BRET measurements, which were performed 28 h after transfection. Before the measurements, the medium over the cells was changed to a modified Krebs–Ringer buffer (50 μl) (described above) for 1 h at 37 °C. Measurements were performed at 37 °C using a ThermoFisher Scientific Varioskan LUX Multimode Microplate Reader, and started with the addition of the cell-permeable luciferase substrate coelenterazine-H (40 μl; final concentration of 5 μM), and counts were recorded using 480 nm and 530 nm emission filters. Detection time was 250 ms for each wavelength. The indicated reagents were also dissolved in modified Krebs-Ringer buffer and added (20 μl). All measurements were done in two biological replicates. To calculate changes in the PM lipid levels, BRET ratios were calculated by dividing the 530 nm and 480 nm intensities and normalized to the baseline. Because the absolute ratio values depended on the expression of the sensors in the case of the intermolecular inositol lipid sensors, the resting levels were considered as 100%, whereas 0% was determined from the values of those experiments where cytoplasmic luciferase construct was expressed alone.

Knockdown experiments

HEK293-AT1 or HEK293A cells were plated on 6-well plates at a density of 1.5×10^5 cells/well. One day later, the medium was changed to fresh culture medium and cells were transfected with 200 μl transfection mixture containing 6 μl/well Lipofectamine RNAiMAX and the indicated siRNAs (120 pmol/well). All siRNAs were ON-TARGETplus SMARTpool (Horizon Discovery) mixes of 4 different sequences against the target gene (L-004152–00–0005 for SHIP2, L-006771–00–0005 for PI3KC2A, L-006772–00–0005 for PI3KC2B) and we used ON-TARTGETplus Non-targeting Pool as scrambled control (D-001810–10–05). 48 h later, DNA transfection and BRET measurements or immunoblotting were carried out as detailed in the relevant sections.

Immunoblotting

Cells were cultured on 6-well plates (4×10^5 cells/well) in cDMEM at 37 °C. One day later, HEK293A cells were transfected by adding 200 μl transfection mixture containing the indicated DNA constructs (0.5 μg DNA total/well) and 2 μl/well Lipofectamine 2000. 23 h after plating (HeLa) or transfection (HEK293A), cells were made quiescent by incubation in serum-free DMEM for 5 h. After agonist stimulation, reactions were stopped by placing the 6-well plates on ice and washing each well with ice-cold modified Krebs–Ringer buffer

(described above). Cells were then scraped with 2 × concentrated Laemmli buffer supplemented with 2-mercapto-ethanol (5%) and protease and phosphatase inhibitors (cOmplete protease inhibitor cocktail, Roche 11,836,145,001). This cell lysate was briefly sonicated, then boiled at 95 °C for 10 min, and equal amounts of samples were loaded into 4 to 15% SDS-polyacrylamide gels (BioRad, 4,561,083). Proteins were transferred to PVDF membranes (BioRad, 1,704,156). Membranes were blocked with a 5% blocking solution (fat-free milk powder diluted in TBST) for 1 h at room temperature and incubated with the primary antibody (diluted 1:1000 in TBST containing 5% fat-free milk powder) overnight at 4 °C. Membranes were washed 3 times with TBST for 10 min, then incubated with HRP-linked secondary antibody (anti-rabbit, Cell Signaling #7074, or anti-mouse, Cell Signaling #7076, diluted 1:5000 in TBST containing 5% fat-free milk powder) for 1 h at room temperature and washed 3 times. The signals were visualized with enhanced chemiluminescence, using Immobilon Western HRP substrate reagent, and were then detected with an Azure c600 device. All immunoblot images shown are representative of at least 3 independent experiments. Bands were quantified by measuring the total pixel intensity with background subtraction using ImageJ. The primary antibodies used were rabbit anti-phospho-SHIP2 (Tyr-986/987, Cell Signaling, #2008), rabbit anti-phospho-SHIP2 (Tyr-1135, Thermo Fisher Scientific, PA5104651), rabbit anti-SHIP2 (Cell Signaling, #2839), rabbit anti-Akt (Cell Signaling, #4691), rabbit anti-phospho-Akt (Ser-473, Cell Signaling, #4060), rabbit anti-ERK (Cell Signaling, #9102), mouse anti-phospho-ERK (Thr-202/Tyr-204, Cell Signaling, #9106), mouse anti-EGFR (Santa Cruz, sc-373746), and mouse anti-phospho-EGFR (Tyr-1068, Cell Signaling, #2236).

Bioinformatics analysis

The LINCS-L1000 database (https://lincsproject.org/LINCS/) is a collaborative effort for the systematic screening of gene expression pattern changes of selected human cell lines responding to various treatments (perturbations). These treatments include drug induced selective activation or inhibition of various proteins as well as knock-out or knock-down of selected genes *via* CRISPR or siRNA techniques. The cell lines, the drugs, the experimental protocols, all the related parameters and data processing steps are standardized across the project. The results are collected in the L-1000 database as normalized sets of gene expression change profiles of the given perturbation.

From the database, the INPPL1 (the gene symbol of SHIP2) perturbation profiles were selected. The selection was further narrowed down to cell lines containing data for more than one perturbation experiment for SHIP2. This restriction resulted in 16 cell lines, mostly of tumor origin. Their perturbation profiles were screened for similarity with the ones of SHIP2 using Spearman correlation as the metrics of similarity. Gene set enrichment analysis was applied on the gene similarity sets using the python "decoupler" module with Z-score normalization. In the case of ligand induced perturbation experiments activation and inhibition data were treated separately (59). The procedure resulted in a ranked list of protein perturbation profiles, correlating or anti-correlating with the perturbation profiles of SHIP2 (positive and negative values, respectively).

Mathematical and statistical analysis

SigmaPlot 10.0 was used for statistical analysis, the tests applied (including *post hoc* tests after ANOVA) for each comparison are indicated in the figure legends. The program automatically tested for normal distribution and equal variance of the samples, and *t* test or ANOVA were used only when both tests passed, otherwise non-parametric tests (*e.g.* ANOVA on Ranks) were used.

Data availability

The datasets generated during and/or analyzed during the current study are available from the corresponding author upon reasonable request.

Acknowledgments—We are thankful for the technical assistance of Kata Szabolcsi.

Author contributions—M. C., A. D., and D. J. T. writing–original draft; M. C. methodology; A. K., S. B., D. K. N., A. D., and P. V. investigation; L. H. and P. V. conceptualization; A. D., D. J. T., and P. V. visualization; D. J. T. formal analysis; P. V. writing–review & editing.

Funding and additional information—This work was supported by the Hungarian National Research, Development and Innovation Fund (NKFI K134357, TKP2021-EGA-24).

Conflict of interest—The authors declare that they have no conflicts of interest with the contents of this article.

Abbreviations—The abbreviations used are: BRET, bioluminescence resonance energy transfer; Btk, Bruton's tyrosine kinase; PH, pleckstrin homology; PIP, phosphoinositide; PIP3, phosphatidylinositol 3,4,5- trisphosphate; PM, plasma membrane; RTK, receptor tyrosine kinase; SHIP2, SH2-domain containing inositol polyphosphate 5-phosphatase 2.

References

1. Posor, Y., Jang, W., and Haucke, V. (2022) Phosphoinositides as membrane organizers. *Nat. Rev. Mol. Cell Biol.* **23**, 797–816
2. Hammond, G. R. V., and Burke, J. E. (2020) Novel roles of phosphoinositides in signaling, lipid transport, and disease. *Curr. Opin. Cell Biol.* **63**, 57–67
3. Dickson, E. J., and Hille, B. (2019) Understanding phosphoinositides: rare, dynamic, and essential membrane phospholipids. *Biochem. J.* **476**, 1–23
4. Lolicato, F., Nickel, W., Haucke, V., and Ebner, M. (2024) Phosphoinositide switches in cell physiology - from molecular mechanisms to disease. *J. Biol. Chem.* **300**, 105757
5. Burke, J. E. (2018) Structural basis for regulation of phosphoinositide kinases and their involvement in human disease. *Mol. Cell* **71**, 653–673
6. Buckles, T. C., Ziemba, B. P., Masson, G. R., Williams, R. L., and Falke, J. J. (2017) Single-molecule study reveals how receptor and Ras synergistically activate PI3Kalpha and PIP(3) signaling. *Biophys. J.* **113**, 2396–2405
7. Truebestein, L., Hornegger, H., Anrather, D., Hartl, M., Fleming, K. D., Stariha, J. T. B., *et al.* (2021) Structure of autoinhibited Akt1 reveals

mechanism of PIP(3)-mediated activation. *Proc. Natl. Acad. Sci. U. S. A.* **118**, e2101496118
8. Sugiyama, M. G., Fairn, G. D., and Antonescu, C. N. (2019) Akt-ing up just about everywhere: compartment-specific Akt activation and function in receptor tyrosine kinase signaling. *Front. Cell Dev. Biol.* **7**, 70
9. Manna, P., and Jain, S. K. (2015) Phosphatidylinositol-3,4,5-triphosphate and cellular signaling: implications for obesity and diabetes. *Cell Physiol. Biochem.* **35**, 1253–1275
10. Hawkins, P. T., and Stephens, L. R. (2016) Emerging evidence of signalling roles for PI(3,4)P2 in Class I and II PI3K-regulated pathways. *Biochem. Soc. Trans.* **44**, 307–314
11. Hasegawa, J. (2024) New insights into the regulation and roles of phosphatidylinositol 3,4-bisphosphate. *J. Biochem.* **176**, 339–345
12. Ray, J., Sapp, D. G., and Fairn, G. D. (2024) Phosphatidylinositol 3,4-bisphosphate: out of the shadows and into the spotlight. *Curr. Opin. Cell Biol.* **88**, 102372
13. Gozzelino, L., De Santis, M. C., Gulluni, F., Hirsch, E., and Martini, M. (2020) PI(3,4)P2 signaling in cancer and metabolism. *Front. Oncol.* **10**, 360
14. Posor, Y., Eichhorn-Gruenig, M., Puchkov, D., Schoneberg, J., Ullrich, A., Lampe, A., *et al.* (2013) Spatiotemporal control of endocytosis by phosphatidylinositol-3,4-bisphosphate. *Nature* **499**, 233–237
15. Wang, H., Loerke, D., Bruns, C., Muller, R., Koch, P. A., Puchkov, D., *et al.* (2020) Phosphatidylinositol 3,4-bisphosphate synthesis and turnover are spatially segregated in the endocytic pathway. *J. Biol. Chem.* **295**, 1091–1104
16. Muraille, E., Pesesse, X., Kuntz, C., and Erneux, C. (1999) Distribution of the src-homology-2-domain-containing inositol 5-phosphatase SHIP-2 in both non-haemopoietic and haemopoietic cells and possible involvement of SHIP-2 in negative signalling of B-cells. *Biochem. J.* **342**(Pt 3), 697–705
17. Muller, S. M., and Jucker, M. (2024) The functional roles of the src homology 2 domain-containing inositol 5-phosphatases SHIP1 and SHIP2 in the pathogenesis of human diseases. *Int. J. Mol. Sci.* **25**, 5254
18. Ando, K., Kucukali, F., Doeraene, E., Nagaraj, S., Antonelli, E. M., Thazin Htut, M., *et al.* (2024) Alteration of gene expression and protein solubility of the PI 5-phosphatase SHIP2 are correlated with Alzheimer's disease pathology progression. *Acta Neuropathol.* **147**, 94
19. Thomas, M. P., Erneux, C., and Potter, B. V. (2017) SHIP2: structure, function and inhibition. *Chembiochem* **18**, 233–247
20. Ramos, A. R., Ghosh, S., and Erneux, C. (2019) The impact of phosphoinositide 5-phosphatases on phosphoinositides in cell function and human disease. *J. Lipid Res.* **60**, 276–286
21. Kerr, W. G., Pedicone, C., Dormann, S., Pacherille, A., and Chisholm, J. D. (2020) Small molecule targeting of SHIP1 and SHIP2. *Biochem. Soc. Trans.* **48**, 291–300
22. Wee, P., and Wang, Z. (2017) Epidermal growth factor receptor cell proliferation signaling pathways. *Cancers (Basel)* **9**, 52
23. Petersen, M. C., and Shulman, G. I. (2018) Mechanisms of insulin action and insulin resistance. *Physiol. Rev.* **98**, 2133–2223
24. Delos Santos, R. C., Bautista, S., Lucarelli, S., Bone, L. N., Dayam, R. M., Abousawan, J., *et al.* (2017) Selective regulation of clathrin-mediated epidermal growth factor receptor signaling and endocytosis by phospholipase C and calcium. *Mol. Biol. Cell* **28**, 2802–2818
25. Klip, A., Sun, Y., Chiu, T. T., and Foley, K. P. (2014) Signal transduction meets vesicle traffic: the software and hardware of GLUT4 translocation. *Am. J. Physiol. Cell Physiol.* **306**, C879–C886
26. Varnai, P., Gulyas, G., Toth, D. J., Sohn, M., Sengupta, N., and Balla, T. (2017) Quantifying lipid changes in various membrane compartments using lipid binding protein domains. *Cell Calcium* **64**, 72–82
27. Toth, J. T., Gulyas, G., Hunyady, L., and Varnai, P. (2019) Development of nonspecific BRET-based biosensors to monitor plasma membrane inositol lipids in living cells. *Methods Mol. Biol.* **1949**, 23–34
28. Goulden, B. D., Pacheco, J., Dull, A., Zewe, J. P., Deiters, A., and Hammond, G. R. V. (2019) A high-avidity biosensor reveals plasma membrane PI(3,4)P(2) is predominantly a class I PI3K signaling product. *J. Cell Biol.* **218**, 1066–1079
29. Elong Edimo, W., Derua, R., Janssens, V., Nakamura, T., Vanderwinden, J. M., Waelkens, E., *et al.* (2011) Evidence of SHIP2 Ser132 phosphorylation, its nuclear localization and stability. *Biochem. J.* **439**, 391–401
30. Sampaio, C., Dance, M., Montagner, A., Edouard, T., Malet, N., Perret, B., *et al.* (2008) Signal strength dictates phosphoinositide 3-kinase contribution to Ras/extracellular signal-regulated kinase 1 and 2 activation via differential Gab1/Shp2 recruitment: consequences for resistance to epidermal growth factor receptor inhibition. *Mol. Cell Biol.* **28**, 587–600
31. Uchida, T. (1996) Stimulation of phospholipid synthesis in HeLa cells by epidermal growth factor and insulin: activation of choline kinase and glycerophosphate acyltransferase. *Biochim. Biophys. Acta* **1304**, 89–104
32. Kamentseva, R. S., Kharchenko, M. V., Gabdrahmanova, G. V., Kotov, M. A., Kosheverova, V. V., and Kornilova, E. S. (2023) EGF, TGF-alpha and amphiregulin differently regulate endometrium-derived mesenchymal stromal/stem cells. *Int. J. Mol. Sci.* **24**, 13408
33. Martinez Baez, A., Castro Romero, I., Chihu Amparan, L., Castaneda, J. R., and Ayala, G. (2023) The insulin receptor substrate 2 mediates the action of insulin on HeLa cell migration via the PI3K/Akt signaling pathway. *Curr. Issues Mol. Biol.* **45**, 2296–2308
34. Gulyas, G., Toth, J. T., Toth, D. J., Kurucz, I., Hunyady, L., Balla, T., *et al.* (2015) Measurement of inositol 1,4,5-trisphosphate in living cells using an improved set of resonance energy transfer-based biosensors. *PLoS One* **10**, e0125601
35. Molinari, P., Casella, I., and Costa, T. (2008) Functional complementation of high-efficiency resonance energy transfer: a new tool for the study of protein binding interactions in living cells. *Biochem. J.* **409**, 251–261
36. Chung, J. K., Nocka, L. M., Decker, A., Wang, Q., Kadlecek, T. A., Weiss, A., *et al.* (2019) Switch-like activation of Bruton's tyrosine kinase by membrane-mediated dimerization. *Proc. Natl. Acad. Sci. U. S. A.* **116**, 10798–10803
37. Hunyady, L., Baukal, A. J., Gaborik, Z., Olivares-Reyes, J. A., Bor, M., Szaszak, M., *et al.* (2002) Differential PI 3-kinase dependence of early and late phases of recycling of the internalized AT1 angiotensin receptor. *J. Cell Biol.* **157**, 1211–1222
38. Gulyas, G., Sohn, M., Kim, Y. J., Varnai, P., and Balla, T. (2020) ORP3 phosphorylation regulates phosphatidylinositol 4-phosphate and Ca(2+) dynamics at plasma membrane-ER contact sites. *J. Cell Sci.* **133**, jcs237388
39. Bilanges, B., Posor, Y., and Vanhaesebroeck, B. (2019) PI3K isoforms in cell signalling and vesicle trafficking. *Nat. Rev. Mol. Cell Biol.* **20**, 515–534
40. Wheeler, M., and Domin, J. (2001) Recruitment of the class II phosphoinositide 3-kinase C2beta to the epidermal growth factor receptor: role of Grb2. *Mol. Cell Biol.* **21**, 6660–6667
41. Arcaro, A., Zvelebil, M. J., Wallasch, C., Ullrich, A., Waterfield, M. D., and Domin, J. (2000) Class II phosphoinositide 3-kinases are downstream targets of activated polypeptide growth factor receptors. *Mol. Cell Biol.* **20**, 3817–3830
42. Prasad, N. K., Werner, M. E., and Decker, S. J. (2009) Specific tyrosine phosphorylations mediate signal-dependent stimulation of SHIP2 inositol phosphatase activity, while the SH2 domain confers an inhibitory effect to maintain the basal activity. *Biochemistry* **48**, 6285–6287
43. Phee, H., Jacob, A., and Coggeshall, K. M. (2000) Enzymatic activity of the Src homology 2 domain-containing inositol phosphatase is regulated by a plasma membrane location. *J. Biol. Chem.* **275**, 19090–19097
44. Ruschmann, J., Ho, V., Antignano, F., Kuroda, E., Lam, V., Ibaraki, M., *et al.* (2010) Tyrosine phosphorylation of SHIP promotes its proteasomal degradation. *Exp. Hematol.* **38**, 392–402
45. Huang, W., Barrett, M., Hajicek, N., Hicks, S., Harden, T. K., Sondek, J., *et al.* (2013) Small molecule inhibitors of phospholipase C from a novel high-throughput screen. *J. Biol. Chem.* **288**, 5840–5848
46. Scott, S. A., Mathews, T. P., Ivanova, P. T., Lindsley, C. W., and Brown, H. A. (2014) Chemical modulation of glycerolipid signaling and metabolic pathways. *Biochim. Biophys. Acta* **1841**, 1060–1084
47. Klein, R. R., Bourdon, D. M., Costales, C. L., Wagner, C. D., White, W. L., Williams, J. D., *et al.* (2011) Direct activation of human phospholipase C by its well known inhibitor u73122. *J. Biol. Chem.* **286**, 12407–12416
48. Compeer, M. G., Janssen, G. M., and De Mey, J. G. (2013) Endothelin-1 and endothelin-2 initiate and maintain contractile responses by different mechanisms in rat mesenteric and cerebral arteries. *Br. J. Pharmacol.* **170**, 1199–1209

49. Bill, C. A., and Vines, C. M. (2020) Phospholipase C. *Adv. Exp. Med. Biol.* **1131**, 215–242
50. Blero, D., De Smedt, F., Pesesse, X., Paternotte, N., Moreau, C., Payrastre, B., *et al.* (2001) The SH2 domain containing inositol 5-phosphatase SHIP2 controls phosphatidylinositol 3,4,5-trisphosphate levels in CHO-IR cells stimulated by insulin. *Biochem. Biophys. Res. Commun.* **282**, 839–843
51. Gagnon, A., Artemenko, Y., Crapper, T., and Sorisky, A. (2003) Regulation of endogenous SH2 domain-containing inositol 5-phosphatase (SHIP2) in 3T3-L1 and human preadipocytes. *J. Cell Physiol.* **197**, 243–250
52. Baumgartener, J. W. (2003) SHIP2: an emerging target for the treatment of type 2 diabetes mellitus. *Curr. Drug Targets Immune Endocr. Metabol. Disord.* **3**, 291–298
53. Durrant, T. N., Moore, S. F., Bayliss, A. L., Jiang, Y., Aitken, E. W., Wilson, M. C., *et al.* (2020) Identification of PtdIns(3,4)P(2) effectors in human platelets using quantitative proteomics. *Biochim. Biophys. Acta Mol. Cell Biol. Lipids* **1865**, 158575
54. Gulluni, F., Prever, L., Li, H., Krafcikova, P., Corrado, I., Lo, W. T., *et al.* (2021) PI(3,4)P2-mediated cytokinetic abscission prevents early senescence and cataract formation. *Science* **374**, eabk0410
55. Liu, S. L., Wang, Z. G., Hu, Y., Xin, Y., Singaram, I., Gorai, S., *et al.* (2018) Quantitative lipid imaging reveals a new signaling function of phosphatidylinositol-3,4-bisphophate: isoform- and site-specific activation of Akt. *Mol. Cell* **71**, 1092–1104.e1095
56. Varnai, P., Toth, B., Toth, D. J., Hunyady, L., and Balla, T. (2007) Visualization and manipulation of plasma membrane-endoplasmic reticulum contact sites indicates the presence of additional molecular components within the STIM1-Orai1 complex. *J. Biol. Chem.* **282**, 29678–29690
57. Toth, J. T., Gulyas, G., Toth, D. J., Balla, A., Hammond, G. R., Hunyady, L., *et al.* (2016) BRET-monitoring of the dynamic changes of inositol lipid pools in living cells reveals a PKC-dependent PtdIns4P increase upon EGF and M3 receptor activation. *Biochim. Biophys. Acta* **1861**, 177–187
58. Fafilek, B., Balek, L., Bosakova, M. K., Varecha, M., Nita, A., Gregor, T., *et al.* (2018) The inositol phosphatase SHIP2 enables sustained ERK activation downstream of FGF receptors by recruiting Src kinases. *Sci. Signal* **11**, eaap8608
59. Badia-i-Mompel, P., Vélez Santiago, J., Braunger, J., Geiss, C., Dimitrov, D., Müller-Dott, S., *et al.* (2022) decoupleR: ensemble of computational methods to infer biological activities from omics data. *Bioinformatics Adv.* **2**, vbac016

cells

MDPI

Article

Optimizing PH Domain-Based Biosensors for Improved Plasma Membrane PIP_3 Measurements in Mammalian Cells

Amir Damouni [1], Dániel J. Tóth [1,2], Aletta Schönek [1], Alexander Kasbary [1], Adél P. Boros [1] and Péter Várnai [1,2,*]

[1] Department of Physiology, Faculty of Medicine, Semmelweis University, 1094 Budapest, Hungary; amir.damouni@stud.semmelweis.hu (A.D.); toth.daniel@semmelweis.hu (D.J.T.)
[2] HUN-REN-SU Molecular Physiology Research Group, Hungarian Research Network and Semmelweis University, 1094 Budapest, Hungary
* Correspondence: varnai.peter@semmelweis.hu

Abstract

Phosphoinositide-binding pleckstrin homology (PH) domains interact with both phospholipids and proteins, often complicating their use as specific lipid biosensors. In this study, we introduced specific mutations into the phosphatidylinositol 3,4,5-trisphosphate (PIP_3)-specific PH domains of protein kinase B (Akt) and general receptor for phosphoinositides 1 (GRP1) that disrupt protein-mediated interactions while preserving lipid binding, in order to enhance biosensor specificity for PIP_3, and evaluated their impact on plasma membrane (PM) localization and lipid-tracking ability. Using bioluminescence resonance energy transfer (BRET) and confocal microscopy, we assessed the localization of PH domains in HEK293A cells under different conditions. While Akt-PH mutants showed minimal deviations from the wild type, GRP1-PH mutants exhibited significantly reduced PM localization both at baseline and after stimulation with epidermal growth factor (EGF), insulin, or vanadate. We further developed tandem mutant GRP1-PH domain constructs to enhance PM PIP_3 avidity. Additionally, our investigation into the influence of ADP ribosylation factor 6 (Arf6) activity on GRP1-PH-based biosensors revealed that while the wild-type sensors were Arf6- dependent, the mutants operated independently of Arf6 activity level. These optimized GRP1-PH constructs provide a refined biosensor system for accurate and selective detection of dynamic PIP_3 signaling, expanding the toolkit for dissecting phosphoinositide-mediated pathways.

Keywords: phosphoinositide (PI); phosphatidylinositol 3,4,5-trisphosphate (PIP_3); pleckstrin homology (PH) domain; biosensor; general receptor for phosphoinositides 1 (GRP1); ADP ribosylation factor 6 (Arf6); protein kinase B (Akt); bioluminescence resonance energy transfer (BRET); confocal microscopy

Academic Editor: Juan Carlos Lacal

Received: 5 June 2025
Revised: 14 July 2025
Accepted: 17 July 2025
Published: 21 July 2025

Citation: Damouni, A.; Tóth, D.J.; Schönek, A.; Kasbary, A.; Boros, A.P.; Várnai, P. Optimizing PH Domain-Based Biosensors for Improved Plasma Membrane PIP_3 Measurements in Mammalian Cells. *Cells* **2025**, *14*, 1125. https://doi.org/10.3390/cells14141125

1. Introduction

Phosphoinositides (PIs) are essential structural and functional components of biological membranes. These amphipathic molecules are composed of a glycerol backbone attached to two non-polar fatty acid tails, which vary in length, and a polar inositol head group linked via a phosphate group. Enzymatic modifications of the inositol ring result in seven phosphatidylinositol phosphates (PIPs), each characterized by distinct phosphorylation patterns. These PIPs are dynamically interconverted by the actions of specific kinases and phosphatases [1,2]. Present ubiquitously in all human cell biomembranes,

phosphoinositides are integral not only to membrane architecture but also to functions such as membrane identification and signaling, orchestrating a vast array of cellular activities [3]. Many of their roles are facilitated through interactions with proteins via specific lipid-binding domains, such as pleckstrin homology (PH) domains [4,5].

PH domains are approximately 120-amino-acid long regions commonly found in a wide range of intracellular signaling proteins [6]. These domains differ significantly in their PIP binding affinity and specificity, with certain PH domains binding to only one and others capable of binding to multiple PIP species. Notably, only a small fraction (approximately 10%) of the 234 PH domains in the human proteome bind strongly to phosphoinositides [7]. Their selective binding capacity enables PH domains to direct proteins to defined membrane compartments, thereby contributing to the spatial and temporal regulation of signaling pathways. PH domains are found in a diverse array of signaling molecules, including kinases, guanine nucleotide exchange factors (GEFs), GTPase-activating proteins (GAPs), phospholipases, and other proteins, underscoring their broad functional spectrum in cellular dynamics [8]. Interestingly, although many PH domain-containing proteins possess multiple PH domains, typically only one is actively involved in PIP binding [9]. PH domains with high specificity and affinity for particular PIPs form the basis of lipid biosensors, which are widely employed to monitor dynamic changes in phosphoinositide levels and to investigate lipid-mediated signaling processes [10].

PH domains are well known to mediate plasma membrane (PM) localization primarily through their interactions with phosphoinositides such as phosphatidylinositol 3,4,5-trisphosphate (PIP_3). However, it is also well established that, for several PH domains, lipid binding alone is not sufficient to account for their membrane targeting. In these cases, additional lipid-independent interactions with membrane-associated proteins or structural elements contribute significantly to their localization, a concept referred to as coincidence detection [11,12]. For example, in the case of dynamin, the affinity of its PH domain for PIs is insufficient to direct proper membrane localization by itself, yet its distribution remains regulated by inositol lipid signaling, suggesting the involvement of additional interactions [13–15]. Furthermore, overexpression of isolated PH domains can competitively displace endogenous membrane-associated proteins, thereby inhibiting their function. Interestingly, mutations in PH domains that preserve lipid binding but disrupt lipid-independent interactions, reduce this dominant negative effect. These findings support a model in which both lipid binding and lipid-independent interactions are essential for accurate PH domain localization and functional regulation at the membrane, as was demonstrated in the cases of protein kinase B (PKB or Akt) and general receptor for phosphoinositides-1 (GRP1) [16].

GRP1 is a GEF of the cytohesin family that activates ADP-ribosylation factor (Arf) monomeric GTPases and plays a critical role in vesicular trafficking and cytoskeletal remodeling in mammalian cells [17]. GRP1 contains a PH domain that specifically binds PIP_3, a prerequisite for its localization to the plasma membrane and proper cellular function [18]. While negatively charged phospholipids such as phosphatidylserine may contribute to its membrane localization by generating a weak, transient association, they are insufficient for stable binding on their own [19–21]. The isolated GRP1-PH domain has been widely employed as a biosensor for detecting plasma membrane-associated PIP_3 [10,22,23]. However, its membrane association has been shown to depend not only on PIP_3 binding but also on protein–protein interactions. This was demonstrated by two point mutations at a putative interaction site outside of the lipid-binding pocket, I307E and K340L, which preserve lipid binding yet abolish the ability of the PH domain to exert dominant negative effects [16]. The required non-lipid interaction partner was later identified as the active, GTP-bound form of Arf6 [24].

Akt is a serine/threonine kinase central to the phosphoinositide 3-kinase (PI3K) signaling pathway, regulating key cellular processes such as proliferation, apoptosis, transcription, and glucose metabolism [25,26]. Its activation is triggered by receptor tyrosine kinases (RTKs), which activate PI3K and lead to the production of PIP_3 at the PM [27]. Akt translocates to the PM via its PH domain by binding PIP_3, where it becomes activated and subsequently phosphorylates numerous target proteins in the cytosol, nucleus, and at the membrane [28]. In addition to PIP_3, the PH domain of Akt, specifically that of Akt2, can also bind $PI(3,4)P_2$ [29], and Akt has also been shown to interact with phosphatidylserine at a distinct site that enhances PIP_3 binding [30]. Moreover, Akt is also thought to be involved in protein–protein interactions independent of lipid binding, although the interacting partners remain unidentified. Mutations at threonine 34 in the PH domain, such as T34L and T34F, disrupt this non-lipid interaction without affecting lipid binding, as indicated by a lack of dominant negative effects [16].

In this study, we leveraged specific mutations in the PIP_3-specific PH domains of Akt and GRP1 that selectively disrupt protein-mediated interactions while preserving lipid binding, with the aim of improving biosensor specificity for PIP_3. Using bioluminescence resonance energy transfer (BRET), we evaluated the plasma membrane localization of these biosensors in HEK293A cells under various stimulation conditions. While Akt-PH mutants displayed minimal deviation from wild-type behavior, GRP1-PH mutants exhibited markedly reduced membrane association both at baseline and following stimulation with epidermal growth factor (EGF), insulin, or vanadate. To enhance PIP_3 avidity and biosensor performance, we further developed tandem mutant GRP1-PH constructs, enabling robust detection of PIP_3 dynamics. In addition to BRET-based assays, we demonstrated the utility of these optimized biosensors in confocal microscopy. Finally, we examined the influence of Arf6 activity and found that, unlike their wild-type counterparts, the mutant GRP1-PH sensors localized to the membrane independently of Arf6, further improving their specificity for PIP_3 detection.

2. Materials and Methods

2.1. Materials

All molecular biology materials, including Lipofectamine 2000, were purchased from Thermo Fisher Scientific. Coelenterazine-H was supplied by Regis Technologies (Morton Grove, IL, USA), and insulin was obtained from Eli Lilly (Indianapolis, IN, USA). Unless noted otherwise, additional chemicals and reagents were sourced from Sigma–Aldrich (St. Louis, MO, USA).

2.2. DNA Constucts

The PH domain constructs utilized in this work included the following amino acid regions: human GRP1 (residues 267–399; AJ005197), human Akt1 (residues 1–164; NM_005163), and human Btk (residues 1–177; BC109079) [31,32]. To generate GRP1-PH biosensors harboring the I307E and K340L point mutations, the original PH domain sequences described in our earlier study [16] were substituted with a wild-type version using BglII and EcoRI restriction enzymes [33]. For constructing the tandem GRP1-PH biosensor (L10-mVenus-T2A-NES-Luciferase-GRP1-2xPH), a second PH domain sequence was inserted between the first PH and the luciferase coding region at the BglII site, with the two domains linked via an SSREGS peptide. Similarly, a tandem Btk-PH biosensor (L10-mVenus-T2A-Btk-2xPH-Luciferase) was created by introducing a second PH domain sequence between the initial PH and luciferase regions at the AgeI site, joined by a DPPVAAGAGGAG linker [34]. For fluorescent labeling, both single and tandem GRP1-PH constructs were inserted between the BglII and EcoRI sites of the pEGFP-C1 vector, in

which GFP was replaced by an N-terminal NES (ALQKKLEELELDEA)-tagged Venus fluorescent protein.

The human EGF receptor, non-internalizing rat type-1 angiotensin receptor (AT1R Δ319) and sensors for phosphatidylinositol 4-phosphate (PI4P) (L10-Venus-T2A-Luc-SidM-2xP4M) and phosphatidylinositol 4,5-bisphosphate [PI(4,5)P2] (L10-Venus-T2A-PLCd1-PH-Luc) were described [16,35,36]. Arf6 constructs were a kind gift from Julie Donaldson, NHLBI, NIH (Bethesda, MD, USA) [24].

2.3. Cell Culture

All experiments were conducted using HEK293A cells, obtained from Thermo Fisher Scientific (Waltham, MA, USA) (Cat. No. R70507). The cells were cultured in DMEM (Gibco (Waltham, MA, USA) 11995065) containing 10% fetal bovine serum (Biosera (Cholet, France)), FB-1200), along with 50 units/mL penicillin and 50 µg/mL streptomycin (Gibco (Waltham, MA, USA), 15140-122). Cultivation was carried out in 10 cm plastic culture dishes at 37 °C in a humidified incubator with 5% CO_2.

2.4. BRET Measurements

HEK293A cells were detached using 0.25% trypsin (Lonza (Basel, Switzerland), Cat. No. BE17-160E) and seeded into white 96-well plates (Greiner Bio-One (Kremsmünster, Austria), Cat. No. 655083) pre-coated with 0.001% poly-L-lysine for 1 h. Cells were plated at a density of 6×10^4 per well. Co-transfection was performed using Lipofectamine 2000 (0.25 µL per well) and 0.03–0.04 µg of total plasmid DNA per well, diluted in Opti-MEM reduced serum medium (Gibco (Waltham, MA, USA), Cat. No. 31985047). To overcome the variability associated with endogenous EGF receptor (EGFR) expression in HEK293-derived cell lines, in addition to the BRET sensors, cells were also transfected with EGFR. After 28 h, BRET measurements were performed following a 5 h serum starvation period. Before measurements, the medium was replaced with 50 µL of modified Krebs–Ringer buffer (120 mM NaCl, 4.7 mM KCl, 1.2 mM $CaCl_2$, 0.7 mM $MgSO_4$, 10 mM glucose, and 10 mM Na-HEPES, pH 7.4) and incubated at 37 °C for 1 h. Measurements were conducted at 37 °C using a Thermo Fisher Scientific (Waltham, MA, USA) Varioskan LUX Multimode Microplate Reader. To begin the measurements, 40 µL of coelenterazine-H (a membrane-permeable luciferase substrate) was added to each well in a final concentration of 5 µM. Luminescence signals were then captured using 480 nm and 530 nm emission filters, with an acquisition time of 250 ms per wavelength. Additional compounds were introduced in 20 µL volume dissolved in modified Krebs–Ringer buffer. For experiments involving vanadate, a fresh solution was prepared before each run by combining 30 µM hydrogen peroxide with 100 µM sodium orthovanadate in a 1:1 ratio. All measurements were conducted in duplicate biological replicates. BRET ratios, used to monitor changes in plasma membrane lipid content, were determined by dividing the emission intensity at 530 nm by that at 480 nm. Since absolute ratio values depended on sensor expression levels, in some experiments these ratios were normalized with resting levels set to 100%, while 0% was determined from experiments using a cytoplasmic luciferase construct alone.

2.5. Confocal Microscopy

HEK293A cells were seeded at a density of 3×10^4 cells per well onto IBIDI 8-well µ-Slides (Cat. No. 80826) pretreated with 0.001% poly-L-lysine for 1 h. Cells were cultured in DMEM at 37 °C for 24 h before transfection. For transfection, the medium was replaced with 200 µL Opti-MEM containing the indicated DNA constructs (0.2 µg total DNA/well) and 0.33 µL/well Lipofectamine 2000. After 6 h, the transfection medium was replaced with 300 µL supplemented DMEM. Serum-starved cells (5 h) were imaged 24–26 h post-transfection using a Zeiss LSM 710 laser confocal microscope equipped with a

63×/1.4 oil-immersion objective, heated to 30 °C. Prior to imaging, medium was changed to 200 µL/well modified Krebs-Ringer buffer (described above) at room temperature. For stimulation, EGF was added in an additional volume of 100 µL. Image analysis was conducted using Fiji 1.54p and Photoshop C3 (Adobe), with only linear adjustments applied during processing. After background subtraction, fluorescent pixel intensity changes in various compartments of the cells were measured by Fiji.

2.6. Mathematical and Statistical Analysis

Data analysis was carried out using SigmaPlot version 10.0. The particular statistical methods employed are described in the corresponding figure legends. Quantitative results are expressed as mean ± standard deviation, based on a minimum of three separate experiments.

3. Results

3.1. The PM PIP_3 Sensing Ability of the GRP1-PH- and Akt-PH-Based Biosensor Mutants Compared to the Wild Type

To measure PIP_3 levels, we utilized BRET-based biosensors by fusing the lipid-binding domains of Akt, GRP1, or their respective mutants to the BRET donor molecule luciferase. To specifically monitor PIP_3 levels at the plasma membrane, the BRET acceptor, Venus, was anchored to the membrane using the Lck targeting sequence. Additionally, a nuclear export signal (NES) was incorporated into the GRP1-based sensors to counteract their previously observed nuclear accumulation. Both the donor and acceptor components were expressed from a single construct, separated by a T2A sequence to ensure equimolar expression following transfection. A more detailed description of this method has been published previously [22,33]. This setup enabled a comprehensive comparative analysis of biosensor behavior under various stimulations, providing insights into the role of lipid-independent interactions in biosensor dynamics. The GRP1-PH biosensor was examined alongside two mutants: K340L (lysine-to-leucine substitution at position 340) and I307E (isoleucine-to-glutamic acid substitution at position 307). Similarly, the Akt-PH sensor was analyzed with two mutants in which threonine at position 34 was replaced by leucine (T34L) or phenylalanine (T34F) (Figure 1A). These mutations in both proteins were selected in a previous study based on structural data suggesting they are located away from the lipid-binding pocket and on a putative site for protein–protein interactions (16, see also graphical abstract). All selected mutants exhibit impaired protein interactions while retaining their lipid-binding affinity [16,24].

We conducted our experiments in HEK293A cells and evaluated biosensor responses to various stimuli known to modulate PIP_3 levels. Given the established role of receptor tyrosine kinases (RTKs) in activating PI3K and promoting PIP_3 production, we focused on stimulation with epidermal growth factor (EGF) and insulin. To further probe PIP_3 dynamics, we also included sodium vanadate, a phosphatase inhibitor known to elevate PIP_3 levels. Cells were transfected with the wild type or mutant biosensors, and EGFR. After 28 h, serum-starved cells were stimulated with EGF (100 ng/mL), insulin (70 nM), or vanadate (100 nM), and BRET ratio variations were calculated.

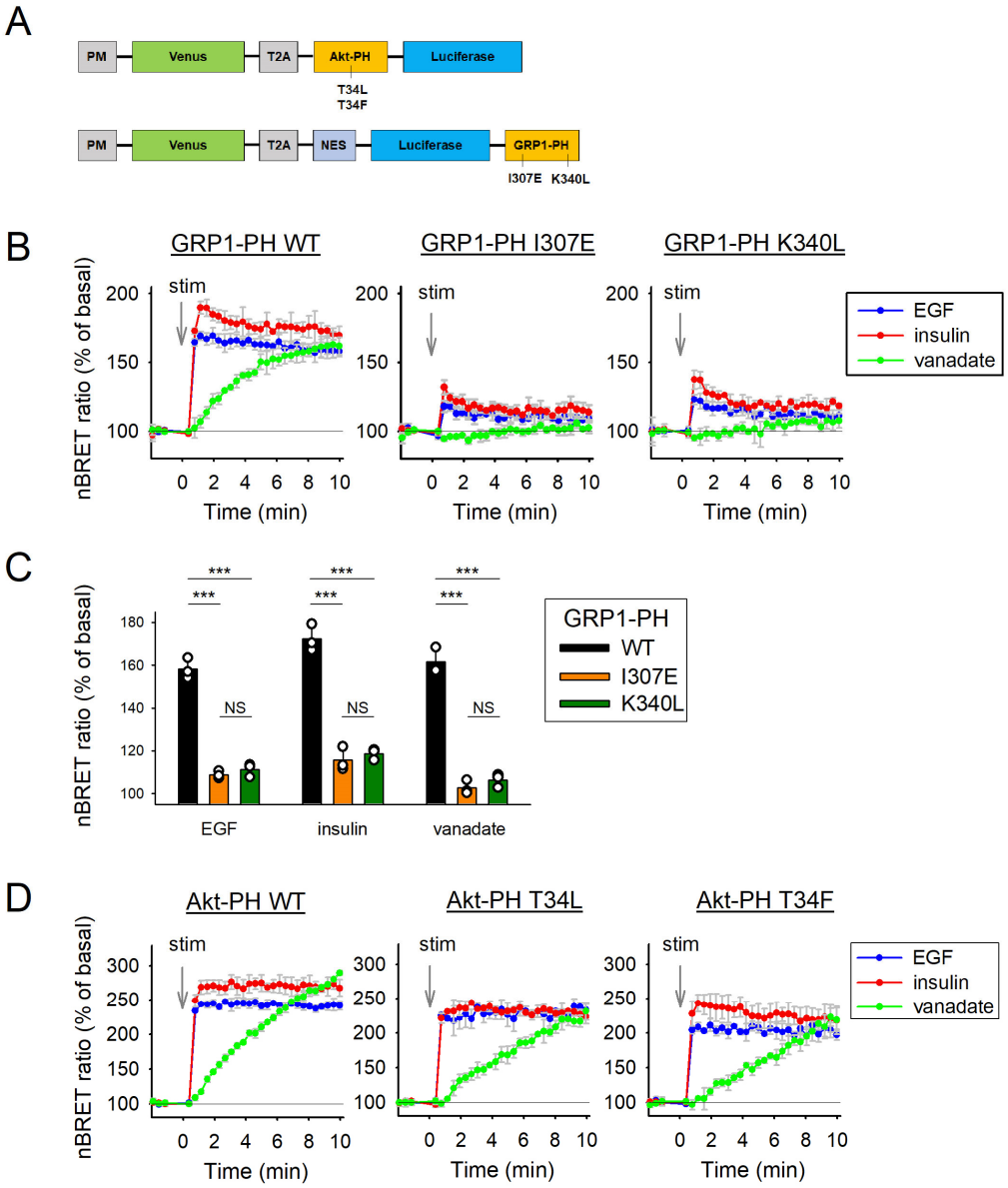

Figure 1. The PM PIP_3 sensing ability of GRP1-PH- and Akt-PH-based biosensor mutants compared to the wild type (WT). (**A**) Schematic representation of the domain structures of the phosphoinositide BRET-based biosensors used in this study. 'PM' denotes the plasma membrane-targeting sequence of Lck, while 'T2A' refers to a viral peptide sequence which enables the production of two separate polypeptide chains. Mutations that disrupt protein interactions are indicated for each PH domain. (**B**) PIP_3 level changes were measured with GRP1-PH-based BRET sensors in HEK293A cells. Cells were transiently transfected with EGFR, as well as the wild-type (WT) or mutant (I307E and K340L) sensors, as indicated. At 28 h later and after a 5 h period of serum starvation, cells were treated with 100 ng/mL EGF, 70 nM insulin or 100 nM vanadate at the zero time point (stimulation). The calculated BRET ratio values were normalized for the baselines (100%) for each curve. Data are the means ± SD, $n = 3$. (**C**) To statistically test the signals of the WT and mutant sensors with each stimulus, we calculated the means (± SD) of the last 5 measurement points of the curves from panel B. We used one-way ANOVAs with Holm–Sidak post-hoc tests separately for each treatment. *** $p < 0.001$, NS $p > 0.05$. (**D**) PIP_3 level changes were measured with Akt-PH-based BRET sensors in HEK293A cells. Cells were transiently transfected with EGFR and either WT or mutant (T34L and T34F) sensors. Experimental conditions, treatments (EGF, insulin, and vanadate), and BRET ratio normalization were as described in panel B. Data are the means ± SD, $n = 3$.

As expected, the wild-type GRP1-PH domain displayed a significant increase in BRET ratios across all treatments, indicative of increased PM localization (Figure 1B, left graph). Conversely, the I307E and K340L mutants showed only marginal increases in BRET ratios (Figure 1B, middle and right graphs). A direct comparison of wild-type and mutant sensors following 10 min stimulation with each agent revealed a significantly reduced response in the mutants across all three treatments (Figure 1C), underscoring the importance of lipid-independent interactions in mediating the PM recruitment of the wild-type GRP1-PH domain.

Following the same experimental protocol, we then evaluated the wild-type Akt-PH domain and its two mutants, T34L and T34F. The wild-type Akt-PH domain showed a significant increase in BRET ratios across all treatments (Figure 1D, left graph), while both mutants, T34L and T34F, exhibited a comparable but slightly diminished response (Figure 1D, middle and right graphs). Taken together, these findings suggest that although the GRP1-PH domain mutants enhance lipid-binding specificity by minimizing protein-mediated interactions, their limited signal amplitude compromises their utility for dynamic lipid monitoring. In contrast, the preserved responsiveness of the Akt-PH mutants suggests that lipid-independent interactions play a lesser role in the membrane association and functional performance of Akt-based biosensors.

3.2. Enhancing the PIP_3 Affinity of Lipid Selective Mutant GRP1-PH Based Biosensors

To overcome the lower affinity of the mutated GRP1-based sensors compared to the wild type, evident from their significantly diminished response to the same treatments (Figure 1C), we developed tandem versions of the previously employed mutated PH domains, an approach generally correlated with enhanced lipid binding strength. In line with the previously applied protocol, we initially transfected cells with EGFR and our novel mutated biosensors. After 28 h, serum-starved cells were treated with 100 ng/mL EGF, 70 nM insulin, or 100 nM vanadate, and BRET ratio variations were calculated. As expected, the tandem configurations of the sensors exhibited a substantially greater increase in response to each treatment (Figure 2A) compared to their single-domain counterparts (Figure 1B). To demonstrate the functionality of the tandem mutants, we averaged the BRET ratio changes observed at the end of each measurement across all stimuli (Figure 2B), which were comparable to those elicited by the wild-type sensor (Figure 1C).

To gain deeper insight into the properties of our BRET-based biosensors, we assessed their basal BRET ratios, measured before any stimulation. These initial values reflect the extent to which the lipid-binding domains are localized to the plasma membrane under resting conditions across all GRP1-PH-based sensor variants. As expected, disruption of lipid-independent interactions in the mutant sensors resulted in significantly lower basal BRET ratios compared to the wild-type GRP1-PH, indicating reduced membrane association despite intact lipid-binding capability. Notably, the tandem mutant constructs exhibited higher basal BRET ratios than their single-domain counterparts, consistent with the enhanced membrane avidity conferred by the tandem configuration (Figure 2C). Together, these results suggest that tandem GRP1-PH mutants combine enhanced membrane recruitment with independence from protein-mediated interactions, making them well-suited for reliable and specific monitoring of dynamic PIP_3 signaling.

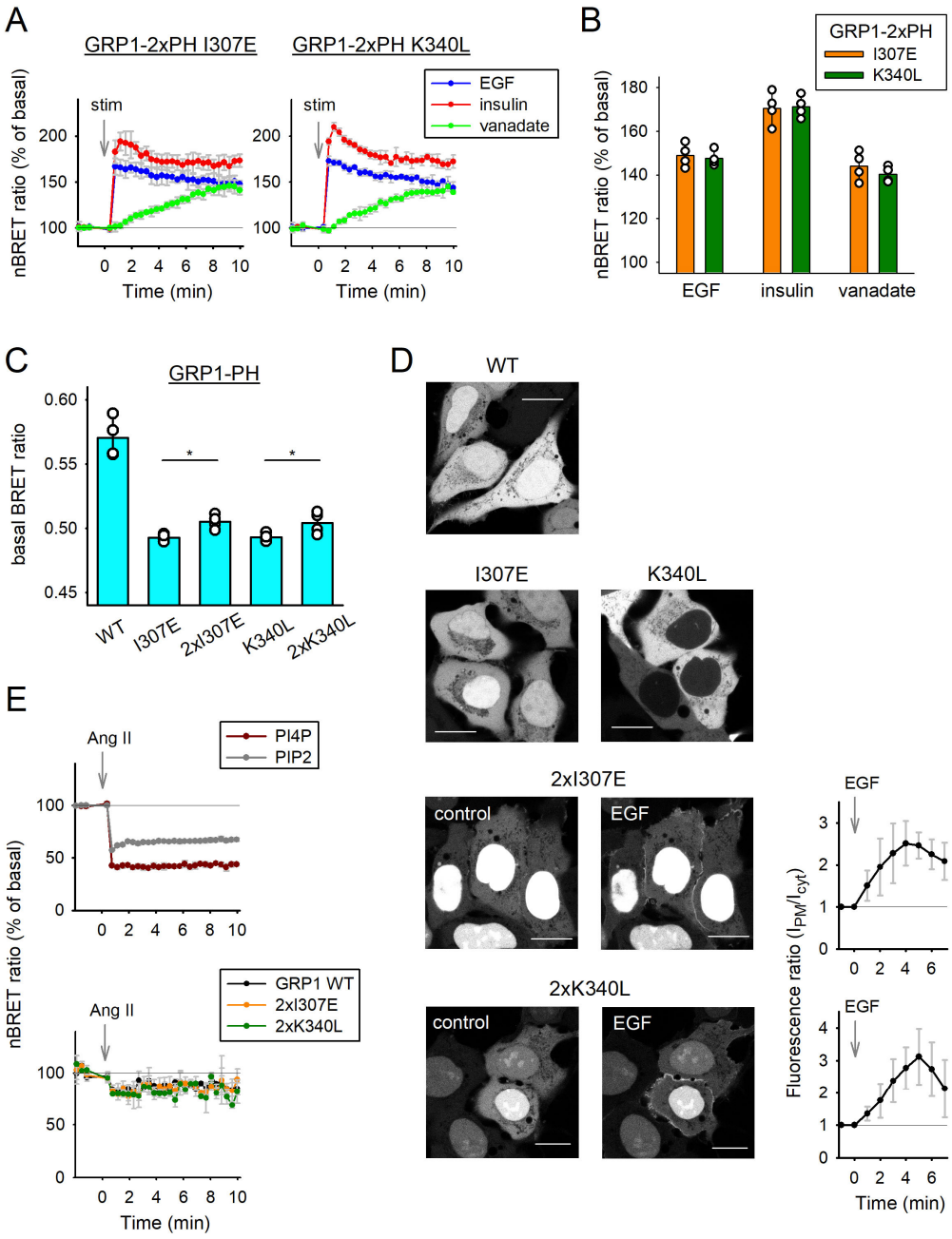

Figure 2. The PM PIP_3 sensing ability of the duplicated mutant GRP1-PH based biosensors. (**A**) PIP_3 level changes were measured using the duplicated BRET sensors in HEK293A cells. Cells were transiently transfected with EGFR and tandem mutant GRP1-PH based sensors (2xPH I307E and 2xPH K340L, as indicated). Experimental conditions, treatments (EGF, insulin, vanadate), and BRET ratio normalization were as described in Figure 1B. Data are the means ± SD, $n = 4$. (**B**) The bar graph displays the average of the last 5 measurement points of the curves from panel A, shown as means ± SD. (**C**) The bar graph shows the corresponding basal BRET ratios (before stimulation) of the indicated sensors from Figures 1B and 2A. Data are the means ± SD, $n = 4$. For statistical analysis, ANOVA on Ranks with the Student–Newman–Keuls post-hoc test was used separately for each mutation site. All mutants were significantly different from the wild type. * $p < 0.05$. (**D**) Representative confocal images of serum-starved (5 h) HEK293A cells expressing the indicated lipid-binding domains tagged with Venus. Cells expressing the tandem I307E or K340L mutants were also imaged 5 min after stimulation with 100 ng/mL EGF, as indicated. Scale bar: 10 µm. After background subtraction, fluorescent intensity changes were measured. Calculation of PM and cytoplasm ratio (IPM/Icyt) was used to quantitate the extent of membrane localization (right graphs).

(**E**) Changes in PI4P, PI(4,5)P_2, and PIP_3 levels were monitored using BRET-based biosensors in HEK293A cells. Cells were transiently transfected with a non-internalizing variant of the type 1 angiotensin receptor (AT1R Δ319) together with the GRP1-based sensors (for PIP_3 detection) SidM-2xP4M (for PI4P) and PLCδ1-PH (for PI(4,5)P_2), as indicated. At 28 h post-transfection and after 5 h of serum starvation, cells were stimulated with angiotensin II (100 nM). The calculated BRET ratio values were normalized to the baseline (100%) for each curve. Data represent the means ± SD, $n = 3$.

To further assess the utility of our newly optimized biosensors beyond BRET-based assays, we performed confocal microscopy to examine their intracellular localization and suitability for imaging-based applications. HEK293A cells were transfected with wild-type GRP1-PH, as well as the single and tandem mutant variants, each tagged with the yellow fluorescent protein Venus. The following day, serum-starved cells were imaged. All biosensors exhibited prominent cytosolic localization and, except for the single K340L mutant, the sensors were also present in the nucleus. To evaluate their responsiveness and applicability for live-cell imaging, cells expressing the tandem I307E or K340L mutants were stimulated with 100 ng/mL EGF. This induced a robust translocation of the sensors to the plasma membrane, confirming their functionality and demonstrating their suitability for confocal microscopy-based detection of PIP_3 dynamics (Figure 2D).

Next, to assess whether the introduced mutations affected the lipid-binding specificity of our optimized GRP1-PH biosensors, particularly with regard to PI4P and PI(4,5)P_2, we performed additional experiments targeting other plasma membrane phosphoinositides. HEK293A cells were co-transfected with wild-type or tandem GRP1-PH-based biosensors, the PI4P-specific SidM-2xP4M sensor, the PI(4,5)P_2-specific PLCδ1-PH sensor, and a non-internalizing variant of the type 1 angiotensin receptor (AT1R Δ319) to promote pronounced changes in PM phosphoinositide levels. After 28 h, serum-starved cells were stimulated with 100 nM of angiotensin II (Ang II) and BRET ratio changes were calculated. As expected, angiotensin II treatment caused a marked reduction in PI4P and PI(4,5)P_2 levels, as detected by the corresponding sensors (Figure 2E, upper graph). In contrast, the GRP1-based biosensors exhibited only a minor decrease in BRET signal (Figure 2E, lower graph), likely reflecting a secondary effect due to depletion of PI(4,5)P_2, the precursor of PIP_3. Importantly, wild-type and tandem mutant GRP1 sensors responded similarly, confirming that the introduced mutations did not alter the lipid-binding specificity of the PH domain.

3.3. Comparison Between Wild-Type and Mutant Sensors Under Varying Arf6 Activity Levels

Given that the mutations in our GRP1-PH sensors have been reported to disrupt interactions with activated Arf6 [16,24], we sought to assess how these sensors respond under varying levels of Arf6 activity. To this end, we repeated our BRET experiments in HEK293A cells using the wild-type (single) GRP1-PH sensor and the tandem I307E mutant, this time co-expressing either wild-type Arf6, a constitutively active GTPase-deficient mutant (Q67L), or a constitutively inactive GTP-binding–deficient mutant (T27N) [37]. To emphasize baseline differences, the resulting BRET ratios are presented without normalization.

As shown in the left graph of Figure 3A, the wild-type GRP1-PH sensor exhibited a markedly higher basal BRET ratio when co-expressed with either wild-type Arf6 or the constitutively active Q67L mutant (black and red curves, respectively), compared to the inactive T27N variant (blue curve). In all three conditions, EGF stimulation led to a further increase in the BRET signal. In contrast, the tandem I307E mutant (right graph) displayed no appreciable differences in basal BRET ratios across the different Arf6 variants and showed a similar EGF-induced increase under all conditions.

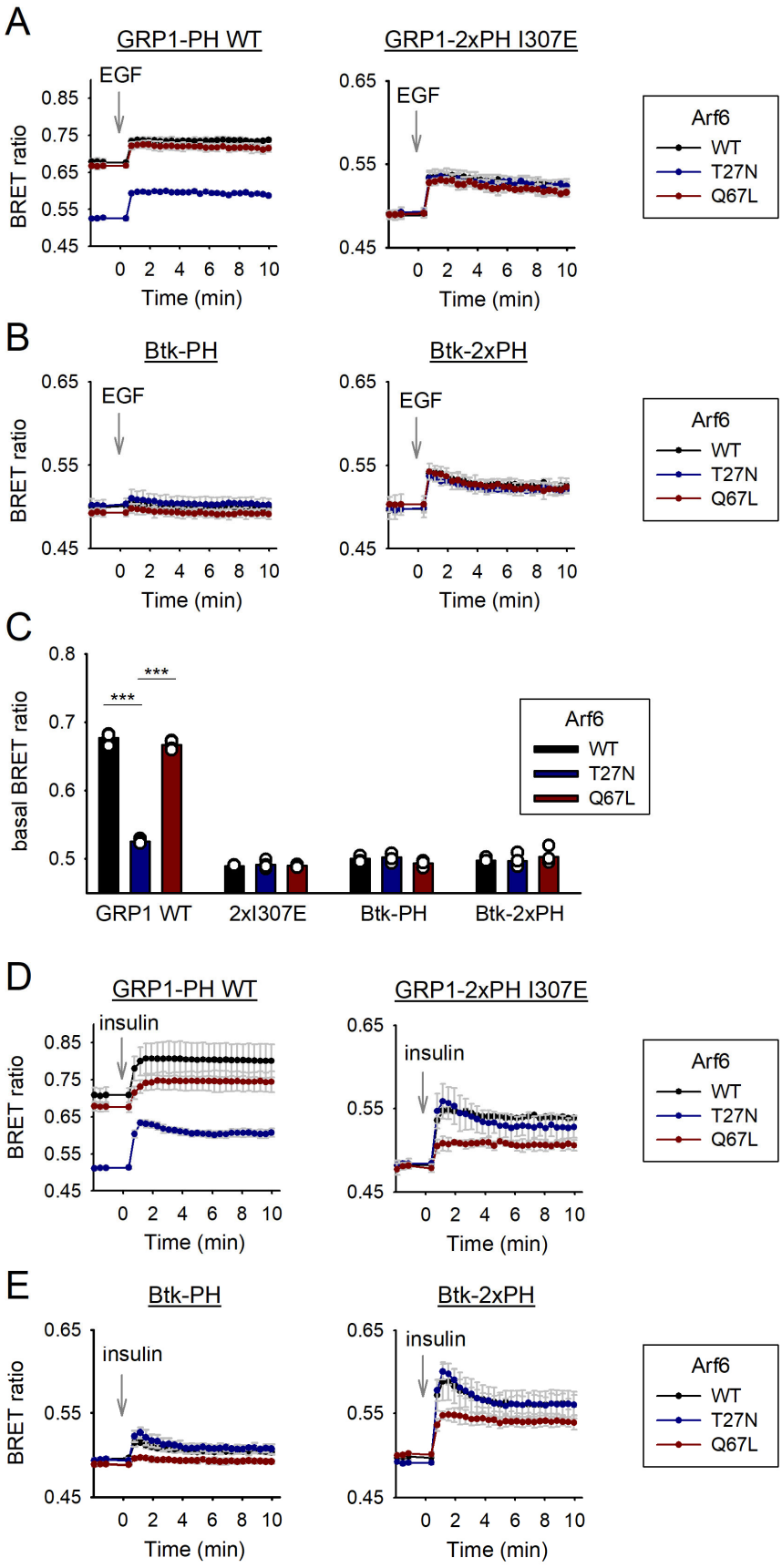

Figure 3. Comparison between wild-type and mutant sensors under varying Arf6 activity levels. (**A**) PIP_3 dynamics were monitored in HEK293A cells using GRP1-PH-based BRET sensors. Cells were

transiently transfected with EGFR and either wild-type or tandem I307E mutant GRP1-PH sensors, as indicated. To assess the effect of Arf6 activity, cells were also transfected with wild-type Arf6, a constitutively active GTPase-deficient mutant (Q67L), or a constitutively inactive GTP-binding-deficient mutant (T27N). At 28 h after transfection, serum starved cells (5 h) were treated with EGF (100 ng/mL), at the time point indicated by the arrows, and the BRET ratio was calculated as described in Methods. Data are the means ± SD, n = 4. (**B**) PIP_3 dynamics were monitored in HEK293A cells using single and tandem Btk-PH-based BRET sensors (left and right graphs, respectively). Experimental conditions, including Arf6 constructs and stimulation, were as described in panel A. Data are the means ± SD, n = 4. (**C**) The bar graph shows the corresponding basal BRET ratios (before stimulation) of the indicated sensors from panels A and B. Data are the mean ± SD of 4 independent experiments. For statistical analysis, one-way ANOVA was used separately for each sensor with Tukey post-hoc test where applicable. Only significant differences are shown for each sensor. *** $p < 0.001$. (**D**) PIP_3 dynamics were monitored in HEK293A cells using GRP1-PH-based BRET sensors. Transfection and experimental conditions were as described in panel A, except cells were stimulated with insulin (70 nM, arrow). Data are the mean ± SD, n = 4. (**E**) PIP_3 dynamics were monitored in HEK293A cells using single and tandem Btk-PH-based BRET sensors (left and right graphs, respectively). Transfection and experimental conditions were as described in panel B, except cells were stimulated with insulin (70 nM, arrow). Data are the means ± SD, n = 4.

To further contextualize our findings with the GRP1-PH-based PIP_3 sensors, we conducted a comparative analysis using sensors based on the PH domain of Bruton's tyrosine kinase (Btk), which is not known to be regulated by Arf6. We performed the same experimental setup as in Figure 3A, using both single and tandem versions of the Btk-PH-based sensor (Figure 3B, left and right panels, respectively). In contrast to the wild-type GRP1-PH sensor, neither sensor variant showed significant differences in basal BRET ratios across varying Arf6 activity levels, including low (T27N, blue curve), high (Q67L, red curve), or wild-type Arf6 (black curve). Consistent with our earlier observations [34], the tandem Btk-PH sensor demonstrated increased sensitivity to PIP_3 elevation following EGF stimulation compared to the single-domain construct.

To statistically evaluate baseline BRET ratios, we averaged the pre-stimulation values for each condition and compared them separately for each sensor (Figure 3C). The wild-type GRP1 sensor showed a significantly higher basal signal when co-expressed with wild-type or constitutively active Arf6 (black and red bars, respectively) compared to the inactive T27N mutant (blue bar). In contrast, no significant differences were observed for the I307E tandem mutant or for either version of the Btk-PH-based sensor. These findings support the conclusion that plasma membrane association of the wild-type GRP1-PH domain is dependent on Arf6 activity level, and that this dependency is abolished by the I307E mutation, enhancing its specificity as a PIP_3 sensor.

We next examined the response of the same set of PIP_3 sensors to insulin stimulation under conditions of varying Arf6 activity (Figure 3D,E). For the wild-type GRP1-PH sensor (Figure 3D, left panel), baseline differences mirrored those observed with EGF stimulation (Figure 3A, left panel). In accordance with previously shown results, insulin elicited a stronger signal increase than EGF, although interpretation was complicated by the markedly different baseline levels across Arf6 conditions. In contrast, the tandem I307E GRP1-PH sensor (Figure 3D, right panel) showed no baseline variation across Arf6 variants, but its insulin-induced response was attenuated in the presence of constitutively active Arf6 Q67L (red curve) compared to both wild-type (black curve) and inactive T27N (blue curve) Arf6. Similar patterns were observed with the Btk-PH-based sensors (Figure 3E), where the tandem version again displayed a more pronounced response to insulin, consistent with the results seen upon EGF stimulation.

Our findings indicate that, unlike the wild-type sensor, the tandem I307E GRP1-PH-based sensor detects PIP_3 changes independently of Arf6 activity while maintaining high

sensitivity. This optimized GRP1-PH construct offers a refined biosensor system for accurate and selective monitoring of dynamic PIP_3 signaling. Using this new sensor, alongside the Arf6-independent Btk-PH-based sensors, we also uncovered a differential insulin-induced PIP_3 response that varies with Arf6 activity, warranting further investigation.

4. Discussion

In this study, we sought to refine the specificity of PIP_3 biosensors by introducing targeted mutations into the PH domains of Akt and GRP1 that preserve lipid binding while disrupting protein-mediated interactions. Our results demonstrate that, while mutations in the Akt-PH domain had minimal impact on plasma membrane association, analogous modifications in the GRP1-PH domain significantly reduced membrane localization both before (basal) and after stimulation with EGF, insulin, and vanadate. Despite offering greater lipid specificity and diminished interference from protein–protein interactions, these single-domain GRP1 mutants exhibited limited signal amplitude, reducing their utility in tracking dynamic lipid changes. To overcome this, we developed tandem GRP1-PH mutants, which restored membrane responsiveness and achieved signal amplitudes comparable to the wild-type sensor. These optimized constructs were effective in both BRET-based assays and confocal microscopy, where EGF stimulation triggered robust translocation of the tandem K340L sensor to the plasma membrane. Moreover, unlike the wild-type sensor, the tandem GRP1-PH mutants displayed membrane recruitment independent of Arf6 activity levels, further supporting their refined specificity. Collectively, our findings establish these optimized GRP1-PH biosensors as refined tools capable of selectively and accurately reporting dynamic PIP_3 fluctuations.

In all experiments, vanadate stimulation elicited a distinct BRET signal profile across the sensors, characterized by a continuous, progressive increase over the entire measurement period. This was in stark contrast to the rapid rise and subsequent plateau observed following EGF or insulin treatment (Figure 1B,D and Figure 2A). The unique kinetics of the vanadate response likely reflect its mode of action: rather than engaging receptor-mediated signaling cascades, vanadate exerts its effect by inhibiting phosphatases, leading to a gradual accumulation of PIP_3 over time [38]. This distinction highlights the differential regulatory mechanisms underlying PIP_3 dynamics depending on the nature of the upstream stimulus.

In our previous microscopy studies, we examined cells expressing fluorescent protein-tagged GRP1-PH biosensors, all of which exhibited prominent nuclear and cytosolic localization [16]. Later, we introduced the NES into the biosensors to reduce nuclear localization [34]. Surprisingly, upon introducing the NES, only the single K340L mutant showed complete exclusion from the nucleus, whereas the other sensors displayed only partial reduction in nuclear signal. Notably, the tandem sensors exhibited strong nuclear localization despite the presence of the NES (Figure 2D). This unexpected behavior suggests that the tandem configuration may impair effective nuclear export. Strong nuclear localization might be a disadvantage for these tandem mutant sensors by reducing the cytosolic fraction of the PH domain, but their enhanced responsiveness to elevations of PM PIP_3 levels (as seen on Figure 2A after EGF and insulin stimulation) show that this can be counterbalanced by improved lipid affinity. Still, further reductions in baseline nuclear localization for these tandem mutant sensors would be desirable, e.g., by introducing tandem or multiple NES sequences.

Another possible drawback for the sensors used in this study is that they require overexpression for reliable detection, which may interfere with cellular functions by sequestering PIP_3 or other binding partners [39]. Near endogenous levels of expression would be ideal as elegantly demonstrated in a recent study using a single-molecule detection

method [40]. However, when minimizing overexpression levels and taking into account this limitation, our new sensors can still be valuable tools to monitor PIP changes and can even be adapted for single-molecule detection techniques.

Consistent with previous findings [18,24], our results indicate that, in addition to PIP_3, active (GTP-bound) Arf6 contributes to the membrane recruitment of wild-type GRP1-PH domains, as evidenced by elevated basal signals upon overexpression of constitutively active Arf6 (Q67L) (Figure 3A,C). Notably, overexpression of wild-type Arf6 produced similarly high baseline signals, suggesting that a substantial proportion of Arf6 is in its active state under these conditions. In contrast, the tandem I307E mutant sensor showed no sensitivity to changes in Arf6 activity levels and displayed reduced membrane association compared to the wild-type sensor even in the presence of inactive Arf6 (T27N), raising the possibility that high levels of inactive Arf6 may still contribute to GRP1-PH membrane localization. However, the physiological relevance of this observation remains unclear and warrants further investigation.

Another notable observation from these experiments was the differential effect of Arf6 activity on insulin-induced PIP_3 signal elevation, which was consistent across all PIP_3 biosensors tested. Interestingly, overexpression of wild-type or inactive Arf6 resulted in comparable increases in PIP_3 levels following insulin stimulation, whereas constitutively active Arf6 attenuated this response. This finding is particularly valuable, as it suggests that these PIP_3 biosensors can also be used to indirectly assess Arf6 activity states in the context of insulin signaling. While both GRP1 and Arf6 have been previously implicated in insulin signaling downstream of PI3K and Akt [41], the mechanisms by which Arf6 modulates insulin-induced PIP_3 production remain unclear and warrant further investigation beyond the scope of this study.

5. Conclusions

In this study, we developed refined GRP1-PH-based biosensors to improve the specificity and performance of PIP_3 detection at the plasma membrane. By introducing targeted mutations that disrupt protein–protein interactions while preserving lipid binding, we generated single-domain variants with enhanced selectivity but reduced signal amplitude. To overcome this limitation, we engineered tandem versions of these mutants, which restored membrane responsiveness to levels comparable with the wild-type sensor. Despite their increased nuclear localization, these tandem constructs demonstrated robust performance in both live-cell imaging and BRET-based assays, offering a reliable tool for dynamic and selective monitoring of PIP_3 signaling with minimal interference from non-lipid interactions.

Our experiments also evaluated the contributions of Arf6 activity to GRP1-PH membrane localization and PIP_3 signaling. The wild-type GRP1-PH sensor displayed elevated basal membrane association when co-expressed with wild-type or constitutively active Arf6, supporting the role of the active Arf6 in facilitating membrane recruitment. In contrast, the tandem I307E mutant showed no sensitivity to Arf6 activity, confirming its specificity for PIP_3 and independence from protein-mediated interactions. Taken together, our results demonstrate that the optimized GRP1-PH constructs serve as reliable and specific tools for monitoring dynamic changes in PIP_3 levels, with reduced susceptibility to interference from protein-mediated interactions.

Author Contributions: Conceptualization, P.V.; methodology, P.V. and D.J.T.; formal analysis, A.D. and D.J.T.; investigation, A.D., A.S., A.K. and A.P.B.; writing—original draft preparation, A.D., A.S. and A.K.; writing—review and editing, D.J.T. and P.V.; visualization, A.D., A.P.B. and P.V.; supervision, P.V.; funding acquisition, P.V. All authors have read and agreed to the published version of the manuscript.

Funding: This work was supported by the Hungarian National Research, Development and Innovation Fund (NKFI K134357, TKP2021-EGA-24).

Institutional Review Board Statement: Not applicable.

Informed Consent Statement: Not applicable.

Data Availability Statement: The datasets generated and/or analyzed during the current study are available from the corresponding author upon reasonable request.

Acknowledgments: We are thankful for the technical assistance of Kata Szabolcsi.

Conflicts of Interest: The authors declare no conflicts of interest.

Abbreviations

The following abbreviations are used in this manuscript:

Akt	Protein kinase B
Ang II	Angiotensin II
Arf6	ADP ribosylation factor 6
AT1R	Type I angiotensin receptor
BRET	Bioluminescence resonance energy transfer
Btk	Bruton's tyrosine kinase
DMEM	Dulbecco's modified Eagle medium
EGF	Epidermal growth factor
EGFR	Epidermal growth factor receptor
GAP	GTPase-activating protein
GEF	Guanine nucleotide exchange factor
GRP1	General receptor for phosphoinositides 1
NES	Nuclear export signal
PH-domain	Pleckstrin homology-domain
PI	Phosphoinositides
PI3K	Phosphoinositide 3-kinase
PIP	Phosphatidylinositol phosphate
PI4P	Phosphatidylinositol 4-phosphate
$PI(4,5)P_2$	Phosphatidylinositol 4,5-bisphosphate
PIP_3	Phosphatidylinositol 3,4,5-trisphosphate
PM	Plasma membrane
RTK	Receptor tyrosine kinase
WT	Wild type

References

1. Dickson, E.J.; Hille, B. Understanding phosphoinositides: Rare, dynamic, and essential membrane phospholipids. *Biochem. J.* **2019**, *476*, 1–23. [CrossRef] [PubMed]
2. Shewan, A.; Eastburn, D.J.; Mostov, K. Phosphoinositides in cell architecture. *Cold Spring Harb. Perspect. Biol.* **2011**, *3*, a004796. [CrossRef] [PubMed]
3. Posor, Y.; Jang, W.; Haucke, V. Phosphoinositides as membrane organizers. *Nat. Rev. Mol. Cell Biol.* **2022**, *23*, 797–816. [CrossRef] [PubMed]
4. Kutateladze, T.G. Translation of the phosphoinositide code by PI effectors. *Nat. Chem. Biol.* **2010**, *6*, 507–513. [CrossRef] [PubMed]
5. Hammond, G.R.V.; Burke, J.E. Novel roles of phosphoinositides in signaling, lipid transport, and disease. *Curr. Opin. Cell Biol.* **2020**, *63*, 57–67. [CrossRef] [PubMed]
6. Lemmon, M.A. Pleckstrin homology (PH) domains and phosphoinositides. *Biochem. Soc. Symp.* **2007**, *74*, 81–93. [CrossRef] [PubMed]
7. Lemmon, M.A. Membrane recognition by phospholipid-binding domains. *Nat. Rev. Mol. Cell Biol.* **2008**, *9*, 99–111. [CrossRef] [PubMed]
8. Ingley, E.; Hemmings, B.A. Pleckstrin homology (PH) domains in signal transduction. *J. Cell Biochem.* **1994**, *56*, 436–443. [CrossRef] [PubMed]

9. Powis, G.; Meuillet, E.J.; Indarte, M.; Booher, G.; Kirkpatrick, L. Pleckstrin Homology [PH] domain, structure, mechanism, and contribution to human disease. *Biomed. Pharmacother.* **2023**, *165*, 115024. [CrossRef] [PubMed]
10. Idevall-Hagren, O.; De Camilli, P. Detection and manipulation of phosphoinositides. *Biochim. Biophys. Acta* **2015**, *1851*, 736–745. [CrossRef] [PubMed]
11. Godi, A.; Di Campli, A.; Konstantakopoulos, A.; Di Tullio, G.; Alessi, D.R.; Kular, G.S.; Daniele, T.; Marra, P.; Lucocq, J.M.; De Matteis, M.A. FAPPs control Golgi-to-cell-surface membrane traffic by binding to ARF and PtdIns(4)P. *Nat. Cell Biol.* **2004**, *6*, 393–404. [CrossRef] [PubMed]
12. Liu, Y.; Kahn, R.A.; Prestegard, J.H. Interaction of Fapp1 with Arf1 and PI4P at a membrane surface: An example of coincidence detection. *Structure* **2014**, *22*, 421–430. [CrossRef] [PubMed]
13. Bethoney, K.A.; King, M.C.; Hinshaw, J.E.; Ostap, E.M.; Lemmon, M.A. A possible effector role for the pleckstrin homology (PH) domain of dynamin. *Proc. Natl. Acad. Sci. USA* **2009**, *106*, 13359–13364. [CrossRef] [PubMed]
14. Szaszak, M.; Gaborik, Z.; Turu, G.; McPherson, P.S.; Clark, A.J.; Catt, K.J.; Hunyady, L. Role of the proline-rich domain of dynamin-2 and its interactions with Src homology 3 domains during endocytosis of the AT1 angiotensin receptor. *J. Biol. Chem.* **2002**, *277*, 21650–21656. [CrossRef] [PubMed]
15. Yu, J.W.; Mendrola, J.M.; Audhya, A.; Singh, S.; Keleti, D.; DeWald, D.B.; Murray, D.; Emr, S.D.; Lemmon, M.A. Genome-wide analysis of membrane targeting by S. cerevisiae pleckstrin homology domains. *Mol. Cell* **2004**, *13*, 677–688. [CrossRef] [PubMed]
16. Varnai, P.; Bondeva, T.; Tamas, P.; Toth, B.; Buday, L.; Hunyady, L.; Balla, T. Selective cellular effects of overexpressed pleckstrin-homology domains that recognize PtdIns(3,4,5)P3 suggest their interaction with protein binding partners. *J. Cell Sci.* **2005**, *118*, 4879–4888. [CrossRef] [PubMed]
17. Jackson, T.R.; Kearns, B.G.; Theibert, A.B. Cytohesins and centaurins: Mediators of PI 3-kinase-regulated Arf signaling. *Trends Biochem. Sci.* **2000**, *25*, 489–495. [CrossRef] [PubMed]
18. Malaby, A.W.; van den Berg, B.; Lambright, D.G. Structural basis for membrane recruitment and allosteric activation of cytohesin family Arf GTPase exchange factors. *Proc. Natl. Acad. Sci. USA* **2013**, *110*, 14213–14218. [CrossRef] [PubMed]
19. Corbin, J.A.; Dirkx, R.A.; Falke, J.J. GRP1 pleckstrin homology domain: Activation parameters and novel search mechanism for rare target lipid. *Biochemistry* **2004**, *43*, 16161–16173. [CrossRef] [PubMed]
20. He, J.; Haney, R.M.; Vora, M.; Verkhusha, V.V.; Stahelin, R.V.; Kutateladze, T.G. Molecular mechanism of membrane targeting by the GRP1 PH domain. *J. Lipid Res.* **2008**, *49*, 1807–1815. [CrossRef] [PubMed]
21. Lai, C.L.; Srivastava, A.; Pilling, C.; Chase, A.R.; Falke, J.J.; Voth, G.A. Molecular mechanism of membrane binding of the GRP1 PH domain. *J. Mol. Biol.* **2013**, *425*, 3073–3090. [CrossRef] [PubMed]
22. Varnai, P.; Gulyas, G.; Toth, D.J.; Sohn, M.; Sengupta, N.; Balla, T. Quantifying lipid changes in various membrane compartments using lipid binding protein domains. *Cell Calcium* **2017**, *64*, 72–82. [CrossRef] [PubMed]
23. Varnai, P.; Balla, T. Live cell imaging of phosphoinositide dynamics with fluorescent protein domains. *Biochim. Biophys. Acta* **2006**, *1761*, 957–967. [CrossRef] [PubMed]
24. Cohen, L.A.; Honda, A.; Varnai, P.; Brown, F.D.; Balla, T.; Donaldson, J.G. Active Arf6 recruits ARNO/cytohesin GEFs to the PM by binding their PH domains. *Mol. Biol. Cell* **2007**, *18*, 2244–2253. [CrossRef] [PubMed]
25. Truebestein, L.; Hornegger, H.; Anrather, D.; Hartl, M.; Fleming, K.D.; Stariha, J.T.B.; Pardon, E.; Steyaert, J.; Burke, J.E.; Leonard, T.A. Structure of autoinhibited Akt1 reveals mechanism of PIP(3)-mediated activation. *Proc. Natl. Acad. Sci. USA* **2021**, *118*, e2101496118. [CrossRef] [PubMed]
26. Sugiyama, M.G.; Fairn, G.D.; Antonescu, C.N. Akt-ing Up Just About Everywhere: Compartment-Specific Akt Activation and Function in Receptor Tyrosine Kinase Signaling. *Front. Cell Dev. Biol.* **2019**, *7*, 70. [CrossRef] [PubMed]
27. Buckles, T.C.; Ziemba, B.P.; Masson, G.R.; Williams, R.L.; Falke, J.J. Single-Molecule Study Reveals How Receptor and Ras Synergistically Activate PI3Kalpha and PIP(3) Signaling. *Biophys. J.* **2017**, *113*, 2396–2405. [CrossRef] [PubMed]
28. Yudushkin, I. Control of Akt activity and substrate phosphorylation in cells. *IUBMB Life* **2020**, *72*, 1115–1125. [CrossRef] [PubMed]
29. Liu, S.L.; Wang, Z.G.; Hu, Y.; Xin, Y.; Singaram, I.; Gorai, S.; Zhou, X.; Shim, Y.; Min, J.H.; Gong, L.W.; et al. Quantitative Lipid Imaging Reveals a New Signaling Function of Phosphatidylinositol-3,4-Bisphophate: Isoform- and Site-Specific Activation of Akt. *Mol. Cell* **2018**, *71*, 1092–1104 e1095. [CrossRef] [PubMed]
30. Huang, B.X.; Akbar, M.; Kevala, K.; Kim, H.Y. Phosphatidylserine is a critical modulator for Akt activation. *J. Cell Biol.* **2011**, *192*, 979–992. [CrossRef] [PubMed]
31. Varnai, P.; Balla, T. Visualization of phosphoinositides that bind pleckstrin homology domains: Calcium- and agonist-induced dynamic changes and relationship to myo-[3H] inositol-labeled phosphoinositide pools. *J. Cell Biol.* **1998**, *143*, 501–510. [CrossRef] [PubMed]
32. Varnai, P.; Rother, K.I.; Balla, T. Phosphatidylinositol 3-kinase-dependent membrane association of the Bruton's tyrosine kinase pleckstrin homology domain visualized in single living cells. *J. Biol. Chem.* **1999**, *274*, 10983–10989. [CrossRef] [PubMed]
33. Toth, J.T.; Gulyas, G.; Hunyady, L.; Varnai, P. Development of Nonspecific BRET-Based Biosensors to Monitor Plasma Membrane Inositol Lipids in Living Cells. *Methods Mol. Biol.* **2019**, *1949*, 23–34. [CrossRef] [PubMed]

34. Damouni, A.; Toth, D.J.; Barsi, S.; Nagy, D.K.; Kasbary, A.; Hunyady, L.; Cserzo, M.; Varnai, P. Differential activation of the inositol 5-phosphatase SHIP2 by EGF and insulin signaling pathways. *J. Biol. Chem.* **2025**, *301*, 110275. [CrossRef] [PubMed]
35. Gulyas, G.; Toth, J.T.; Toth, D.J.; Kurucz, I.; Hunyady, L.; Balla, T.; Varnai, P. Measurement of inositol 1,4,5-trisphosphate in living cells using an improved set of resonance energy transfer-based biosensors. *PLoS ONE* **2015**, *10*, e0125601. [CrossRef] [PubMed]
36. Toth, J.T.; Gulyas, G.; Toth, D.J.; Balla, A.; Hammond, G.R.; Hunyady, L.; Balla, T.; Varnai, P. BRET-monitoring of the dynamic changes of inositol lipid pools in living cells reveals a PKC-dependent PtdIns4P increase upon EGF and M3 receptor activation. *Biochim. Biophys. Acta* **2016**, *1861*, 177–187. [CrossRef] [PubMed]
37. Peters, P.J.; Hsu, V.W.; Ooi, C.E.; Finazzi, D.; Teal, S.B.; Oorschot, V.; Donaldson, J.G.; Klausner, R.D. Overexpression of wild-type and mutant ARF1 and ARF6: Distinct perturbations of nonoverlapping membrane compartments. *J. Cell Biol.* **1995**, *128*, 1003–1017. [CrossRef] [PubMed]
38. Batty, I.H.; van der Kaay, J.; Gray, A.; Telfer, J.F.; Dixon, M.J.; Downes, C.P. The control of phosphatidylinositol 3,4-bisphosphate concentrations by activation of the Src homology 2 domain containing inositol polyphosphate 5-phosphatase 2, SHIP2. *Biochem. J.* **2007**, *407*, 255–266. [CrossRef] [PubMed]
39. Wills, R.C.; Goulden, B.D.; Hammond, G.R.V. Genetically encoded lipid biosensors. *Mol. Biol. Cell* **2018**, *29*, 1526–1532. [CrossRef] [PubMed]
40. Holmes, V.L.; Ricci, M.M.C.; Weckerly, C.C.; Worcester, M.; Hammond, G.R.V. Single-molecule lipid biosensors mitigate inhibition of endogenous effector proteins. *J. Cell Biol.* **2025**, *224*, e202412026. [CrossRef] [PubMed]
41. Li, J.; Malaby, A.W.; Famulok, M.; Sabe, H.; Lambright, D.G.; Hsu, V.W. Grp1 plays a key role in linking insulin signaling to glut4 recycling. *Dev. Cell* **2012**, *22*, 1286–1298. [CrossRef] [PubMed]